The Effects of Nonuniformity on Rare Gas Plasma Magnetohydrodynamic Power Generation(Dissertation_全文)

AUTHOR(S):

Yoshikawa, Kiyoshi

THE EFFECTS OF NONUNIFORMITY ON RARE GAS PLASMA MAGNETOHYDRODYNAMIC POWER GENERATION

KIYOSHI YOSHIKAWA

DECEMBER 1973

INSTITUTE OF ATOMIC ENERGY
KYOTO UNIVERSITY

THE EFFECTS OF NONUNIFORMITY ON RARE GAS PLASMA MAGNETOHYDRODYNAMIC POWER GENERATION

KIYOSHI YOSHIKAWA

DECEMBER 1973

INSTITUTE OF ATOMIC ENERGY
KYOTO UNIVERSITY

ACKNOWLEDGMENTS

The author wishes to express his gratitude for the guidance and encouragement of his adviser, Professor I. Michiyoshi, Department of Nuclear Engineering, Kyoto University. Appreciation is also expressed for the support of Professor Y. Hattori, Institute of Atomic Energy, Kyoto University.

Special thanks are due to Dr. M. Numano, Department of Nuclear Engineering, Kyoto University, for his helpful discussions and to the staff of Kyoto University Computer Center.

The author acknowledges the assistance given by Mr. R. Jayakumar, Scientific officer, Bhabha Atomic Research Center, India and Mr. R. Koga, Corpuscular Engineering Laboratory, Institute of Atomic Energy, Kyoto University, in writing this thesis.

ABSTRACT

In this paper problems concerning spatially nonuniform properties of the MHD plasma were investigated. They were, however, limited to those due to the current concentration at the electrode edge and due to the ionization instability in MHD generation, and also to those due to the spatial temperature distribution in the line-reversal method.

In chapter I, the electrical characteristics of MHD generators with nonuniform gas plasma were investigated. When the surface of discontinuity is not parallel or perpendicular to the direction of the MHD channel length, the electrical conductivity and the Hall parameter become tensor quantities in Ohm's law. With increasing degree of spatial fluctuation of the electrical conductivity, the effective electrical conductivity and the effective Hall parameter greatly decrease both for isotropic and anisotropic nonuniformity. For a Faraday-type MHD generation, the power density is much influenced by the degree of fluctuation, but for a Hall-type MHD generation, on the other hand, it is not so sensitive to the degree of fluctuation and reaches as large as half of the maximum attainable power density for large fluctuations as long as the angle is negative, where the angle is that of the flow direction measured from the axis perpendicular to the surface of discontinuity. The elevation of the electron temperature in a nonuniform gas plasma is also strongly dependent on the degree of fluctuation and the effective nonequilibrium ionization will be hardly expected for large fluctuations.

In chapter II, the feasibility of easing the current concentration at the electrode edge was studied through the adoption of resistive segmented electrodes and leading out the current from the electrodes at the edges opposite the points where the current usually concentrates. Numerical analyses were performed both by difference method and by iteration method, assuming constant gas-dynamical param-

eters and uniform channel cross section. The results reveal that when the resistivity of the electrode is moderate, the current distribution becomes fairly symmetric with reference to the electrode center, and the current concentration on the electrode edge is thus greatly reduced.. When the Hall parameter is large, the internal resistance in case of resistive electrodes becomes nearly equal to that of non-resistive electrodes. For small Hall parameters, however, the internal resistance is appreciably greater in resistive than in non-resistive electrodes.

Another feasibility for the reduction of the current concentration through the adoption of the spatially nonuniform Hall parameters was examined in chapter III and the current refraction was analyzed. The idea to control the current pattern by the spatially nonuniform Hall parameters seemed to be very promising according to the analysis performed, but the application of this idea to the practical MHD generation by using spatially modulated magnetic field will be very difficult to be analyzed, since the analysis must be made in the three dimension, resulting in complications in numerical calculations. Only the feasibility was hence proved in this chapter.

The other representative phenomenon causing a serious nonuniformity in the MHD plasma is the ionization instability. In chapter IV, the condition of occurrence of the ionization instability and the electrical characteristics of MHD generation including the effects of the ionization instability were calculated for an alkali metal seeded noble gas plasma with varying seed fractions, magnetic field strengths and current densities, using the linear perturbation theory with allowance for the ionization of noble gas atoms. The results indicate that the stable region is narrowly restricted, and once the MHD operation condition falls into an unstable region subject to the ionization instability, the power density in a Faraday-type MHD generator with finely segmented electrodes in case of a small seed fraction is no more proportional to the square of the magnetic field strength and furthermore there exists an optimal magnetic field strength for the maximum

power output. But in case of a larger seed fraction of 10^{-3}, on the other hand, where the ionization instability is thought to be dominant, current densities are approximately proportional to the magnetic field strength and power densities to the square of the magnetic field strength. Regardless of fluctuations due to the ionization instability, a Faraday-type MHD generator with finely segmented electrodes operated in a seed fraction of 10^{-3} gives higher power densities, in general, than in case of a smaller seed fraction of 10^{-5}. With increasing operation pressures in case of a seed fraction of 10^{-3}, the plasma remains still stable until large magnetic field strength and consequently the power densities are almost independent of the operation pressure. This will be very favorable to a practical MHD generation.

In the last chapter, from the diagonostic point of view, the influence of the spatial temperature distribution and the measuring configuration on the line-reversal temperature was investigated under MHD generation conditions at a seed fraction of 10^{-3} and atmospheric pressure, under which conditions, dispersion broadening occurs. In order to obtain information about the inner part of the plasma at large optical thicknesses, the width of the spectroscope inlet slit and of the spectral region covered by the photomultiplier must be made sufficiently wide.

TABLE OF CONTENTS

LIST OF FIGURES

LIST OF TABLES

NOMENCLATURE

Latin symbols

A	energy loss of electrons by elastic collisions
A_M	matrix
A_T	logarithmic derivative of A with respect to T_e at steady conditions
a	electrode spacing
a	ratio of collision broadened half-width to Doppler broadened half-width
a_i	ionization coefficient
$\overline{B}$	magnetic field
$\overline{B}_a$	external magnetic field
B_λ	Planck function at wave length λ
$B_{t\lambda}$	specific intensity averaged over $(\lambda-\delta/2,\lambda+\delta/2)$ for $\Delta\neq 0$
b	electrode thickness
C_c	a constant for collision broadening
C_D	a constant for Doppler broadening
C_N	a constant for natural broadening
C_{St}	a constant for Stark broadening
c	electrode length in the flow direction
c	speed of light
c_1, c_2	constants
D/Dt	mobil operator
d	channel height
$\overline{E}$	electric field
$\overline{E}^*$	sum of all electric fields and motional emf's
$\langle E_y^* \rangle_y$	y component of $\overline{E}^*$ averaged over y-axis
$E_{/\!/}^*$	component of $\overline{E}^*$ parallel to the surface of discontinuity
e	elementary electric charge

$\overline{e}_z$	unit vector in z direction
F	function of space
f	degree of fluctuation
$f_j(x)$	spatial distribution function of temperature
f_m	maximum degree of fluctuation
f_{mn}	emission oscillator strength of $m \rightarrow n$ transition
G	degree of nonuniformity
G_{ij}	tensor component of degree of nonuniformity
h	Planck's constant
I_λ	specific intensity at wave length λ
I_t	specific intensity averaged over $(\lambda-\delta/2,\lambda+\delta/2)$ for $\Delta=0$
i	imaginary unit
J	total current
J_λ	specific intensity emitted by plasma alone
$\overline{j}$	current density
$\langle j_x \rangle_x$	x component of $\overline{j}$ averaged over x-axis
$j_\perp$	component of $\overline{j}$ perpendicular to the surface of discontinuity
K_F	load factor of a Faraday-type MHD generator
K_H	load factor of a Hall-type MHD generator
K_0	load factor of a Hall-type MHD generator in a uniform plasma
k	Boltzmann's constant
k_0	$(e^2 n_R f_{mn} \lambda_0 / 4\varepsilon_0 m_e c)\sqrt{M_R/2\pi RT}$
k_r	recombination coefficient
k_λ	absorption coefficient at wave length λ
k_ν	absorption coefficient at wave frequency ν
$k_{\nu c}$	absorption coefficient due to collision broadening
k_{ν_D}	absorption coefficient due to Doppler broadening
k_{ν_N}	absorption coefficient due to natural broadening
$k_{\nu_{St}}$	absorption coefficient due to Stark broadening
$k_{\lvert\xi\rvert}$	absorption coefficient expressed by ξ
L	arbitrary length
ℓ	physical thickness of plasma
M	Mach number

M	tensor Hall parameter
M_p	mole weight of parent atoms
M_R	mole weight of radiating atoms
m_a	mass of an atom
m_e	mass of an electron
m_j	mass of the j-th component
n_e	electron number density
n_P	number density of parent atoms
n_R	number density of radiating atoms
n_{so}	initial number density of seed atoms
n_T	logarithmic derivative of n_e with respect to T_e at steady state conditions
n_A^+	ion number density of argon atoms
n_j^+	ion number density of the j-th component
n_K^+	ion number density of potassium atoms
P_a	normalized absorption coefficient
P_e	power density of an MHD generator
$<P_e>_F$	averaged power density of a Faraday-type MHD generator
$<P_e>_F$	averaged power density of a Faraday-type MHD generator normalized by $<P_e>_{Fmax}$
$<P_e>_H$	averaged power density of a Hall-type MHD generator
$<P_e>_H$	averaged power density of a Hall-type MHD generator normalized by $<P_e>_{Fmax}$
$<P_e>_{Fmax}$	maximum attainable power density of an ideal Faraday-type MHD generator
P_o	pressure of the system
p_e	pressure of electrons
p,q,r	space coordinates
Q_{ej}	elastic collision cross section of electrons with the j-th component
Q_r	energy loss by radiation
$\bar{q}_e$	heat flux vector of electrons
R	gas constant

R_i	internal resistance of an MHD generator
$<R_i>$	internal resistance of an MHD generator normalized by R_{ideal}
R_{ideal}	ideal internal resistance of an MHD generator
R_L	load resistance
R_T	ratio of actual electron temperature to ideal one measured from gas temperature
S	area of electrode surface and neighboring insulator
$S(T_e)$	equilibrium constant of Saha's equation at T_e
s	arbitrary direction
T	plasma temperature
T_c	temperature at plasma center
T_e	electron temperature
T_{e0}	ideal electron temperature in a uniform plasma
T_g	gas temperature
T_s	line-reversal temperature
T_w	temperature at plasma surface
T_Δ	line-reversal temperature averaged over $(\lambda_0-\Delta/2,\lambda_0+\Delta/2)$
$T_{\Delta\infty}$	asymptotic averaged line-reversal temperature T_Δ
$\overline{u}$	gas velocity
V	potential difference
V_H	Hall potential difference
V_H'	Hall potential difference normalized by ψ_0/σ
V_i	ionization potential of seed atoms
$<V_i>$	averaged ionization potential
V_{ij}	ionization potential of the j-th component
v_P	mean relative speed of parent atoms-seed atoms
v_R	mean relative speed of seed atoms-seed atoms
w	channel width
X,Y,Z	space coordinates
x,y,z	space coordinates
x'	coordinate x normalized by d
Y'	perturbed term
y'	coordinate y normalized by d

Greek symbols

α	ratio of electrode resistance to plasma resistance
α_c	a constant
α_i	ionization degree of seed atoms
α_j	ionization degree of the j-th component
α_s	α giving most symmetric current distribution
β_{cr}	critical Hall parameter
β_e	Hall parameter of electrons
β_{eff}	effective Hall parameter of electrons
β_i	Hall parameter of ions
β_j	Hall parameter based on th j-th component of magnetic field
$\Delta\beta_e$	difference of Hall parameters across the surface of discontinuity
γ	ratio of specific capacities
γ_D	ratio of Debye radius of electron alone to the mean distance of ions
γ_e	$\beta_e n_T/\sigma_T$
Δ	wave length region covered by photomultiplier
δ	collision loss parameter of electrons
δ	superposed width (Chapter V)
δ_j	collision loss parameter of electrons with the j-th component
$\overline{\mathcal{E}}^*$	augmented electric field
ε	seed fraction
ε_0	dielectric constant of vacuum
ζ	reduced coefficient of load factor of a Hall-type MHD generator
η	averaged electrical efficiency
η_i	ion broadening parameter
Θ	incident angle of $\overline{j}$ with respect to the surface of discontinuity
Θ^*	Θ giving minimum $\Delta\Theta$
$\Delta\Theta$	angle of deviation of current density

θ	angle between $\overline{u}$ and p-axis (Chapter I)
θ	angle between propagation direction of ionization instability wave and averaged current density
θ_j	angle of direction of $\overline{j}$
θ_j'	angle of direction of $\overline{j}'$
θ^*	$arctan\ \gamma_e$
Λ	$(12\pi/e^3)(\varepsilon_0 kT_e)^{3/2}/n_e^{1/2}$
λ	wave length
λ_e	thermal conductivity of electrons
λ_0	wave length of resonance line
$\Delta\lambda_N$	half-width of wave length for natural broadening
$\Delta\lambda_{Se}$	half-width due to collision of radiating atoms and electrons
μ_e	electron mobility
ν	wave frequency
ν_e	total collision frequency of electrons
ν_{ej}	collision frequency of electrons with the j-th component
ν_0	frequency of resonance line
$\Delta\nu_c$	half-width of frequency for collision broadening
$\Delta\nu_D$	half-width of frequency for Doppler broadening
$\Delta\nu_N$	half-width of frequency for natural broadening
$\Delta\nu_P$	half-width of frequency due to collision with parent atoms
$\Delta\nu_R$	half-width of frequency due to collision with radiating atoms
$\Delta\nu_{St}$	half-width of frequency for Stark broadening
$\Delta\nu_t$	total half-width
ξ	nondimensional frequency
ρ	resistivity of electrode
ρ_P^2	optical cross section of parent atoms
ρ_R^2	optical cross section of radiating atoms
Σ	electrical conductivity corrected for ion-slip
σ	electrical conductivity
σ_{eff}	effective electrical conductivity
σ_L	equivalent electrical conductivity of load resistance
σ_T	logarithmic derivative of σ with respect to T_e at steady

	state conditions
τ^*	characteristic time of ionization instability
τ_λ	optical thickness of plasma at wave length λ
φ	angle between the surface of discontinuity and x-axis
ϕ	potential
ϕ_{ue}	potential on upper electrode
ϕ_{ui}	potential on upper insulator
ϕ'_{ue}	potential on upper electrode normalized by ψ_0/σ
ϕ'_{ui}	potential on upper insulator normalized by ψ_0/σ
Ψ, ψ	current flux function
ψ_0	total current of j_y per unit length of z direction
ψ'	current flux function normalized by ψ_0
Ω	Hall parameter corrected for ion-slip
ω	complex angular velocity $(=\omega_r - i\omega_i)$
ω_i	growth rate

INTRODUCTION

With the progress of human life, the quantity of energy consumption surprisingly increases year by year, causing serious anxiety about fossil fuel exhaustion. The most promising means of solving this problem will be the utilization of nuclear energy through nuclear fission at present and nuclear fusion in the future. A huge number of heat sources will, however, be necessary to meet the huge consumption of energy required, but when energy is practically used, electrical energy is preferentially consumed because of the highest performance. Hence heat energy must be converted into electrical energy with high conversion efficiency. However, the conversion efficiency at present can not exceed much more than 40%, as it experiences mechanical energy on the way of conversion, and thus waste heat more than 50% is thrown away into the atmosphere or the sea. This means immediately not only ineffective usage of energy sources, but also occurrence of serious and large scale thermal pollution. There is no doubt that the thermal pollution will increase in much wider scale on the earth so as to affect the existence of the human beings in the future unless new radical and wise means of energy conversion with much higher efficiency are developed.

In order to solve these problems fundamentally, it is obvious that the energy conversion system with much higher efficiency should be applied and considering large capacity of electrical power, the direct energy conversion by MHD generation fits best to this purpose and here exists the significance of investigations of MHD generation.

In this paper problems concerning mainly the closed cycle plasma (CCP) MHD generation are investigated, and some are surely very peculiar to the CCP MHD generation, but some may well be applicable to the open cycle MHD generation. The merits of the CCP MHD generation are high power density at considerably lower temperatures and lesser mate-

rial restrictions due to high temperature atmosphere than those to the open cycle MHD generation, if the effective nonequilibrium ionization is achieved. In practice, however, it is not so easy to realize the effective nonequilibrium ionization due mainly to the effects of the nonuniformity in the MHD plasma which is the greatest bottleneck to the early realization of the CCP MHD generation at present.

When the external magnetic field is applied, Hall effect appears and this effect becomes strong with increasing magnetic field strength, resulting in nonuniform properties in the MHD plasma. It is needless to say that perfect uniform properties of the MHD plasma are the most desirable[1] from the point of view of the nonequilibrium MHD generation, and the MHD output power depends much on the degree of the nonuniformity and decreases with increasing the degree of the nonuniformity. Hence the phenomena causing nonuniform properties of the MHD plasma should be studied and the method to suppress such phenomena must be investigated.

One of the representative phenomena causing the nonuniformity is the current concentration on the electrode edges due to Hall effects [2], and this phenomenon is solved completely[3] by infinitely segmented electrodes. From the technical point of view, however, infinite segmenting is almost impossible in an actual generator and thus finite segmenting effects remain. In case of finite segmenting and constant plasma parameters, the elongation of current path results in the increase of internal resistance of MHD generators[4], but it can be reduced to some degree by staggering electrodes[5]. From the point of view of nonequilibrium ionization, short-circuiting between neighboring electrodes by large induced Hall fields and strongly nonuniform Joule heating due to the current concentration become rather serious problems. The former results in an internal current leak loop, thereby in the reduction of segmenting effects of electrodes[6] and consequently in the large power loss of MHD generation. The latter incurs the spatial nonuniformity of the electron temperature due to nonuniform Joule heating[7,8,9,10] resulting also in the deterioration of elec-

trical performances of MHD generation. In the field of study to suppress the current concentration on the electrode edges, there were a few proposals, one of which is the adoption of wedged-shape resistive segmented electrodes[3,37] and another is the adoption of staggered electrodes[5]. With respect to the proposal of the former, however, no detail analysis has not been made and recently an experiment using resistive segmented electrodes equivalent to wedged-shape resistive ones was reported[11] but not in detail with respect to their performances. As to staggered electrodes, considerably uniform current distribution is surely obtained, but the current concentration seems to remain still to some degree. In chapter II, resistive segmented electrodes which are different from wedged-shape resistive electrodes are proposed and electrical characteristics of MHD generator together with current distribution are numerically analyzed.

From the point of view of controlling current distribution, end effects have already been analyzed by using spatially modulated magnetic field[12,13,14]. In chapter III, current refraction due to spatially discontinuous Hall parameters are also analyzed and the feasibility of current distribution control by spatially modulated magnetic field through Hall parameters are discussed.

Another representative phenomenon causing the nonuniformity is the ionization instability due to incomplete relief of the excess energy by the local fluctuation of Joule dissipation. This phenomenon occurs when the Hall parameter exceeds the critical Hall parameter which is dependent on the macroscopic properties of the plasma[15,16, 17]. The expressions of the effective electrical conductivity and the effective Hall parameter were theoretically obtained for an isotropic [18] and an anisotropic[19] nonuniformity and were also numerically calculated[20]. Considerably well expressed equations for these quantities have been given by many experiments[21,22,23,40]. A few transient numerical analyses for the mechanism of the ionization instability[20,24] were made and its wave length[22,25,26], mode[27] and velocity[28] including boundary conditions were also studied, and recently

current streamer was observed by image converter technique[29] and investigated[41]. One method to suppress the ionization instability is to realize perfect ionization by very small seed fraction, say 10^{-5}, aiming at the increase of the critical Hall parameter[30] and this method was experimentally confirmed[30,31,32]. Another method, also proposed and analyzed[33], is to mix impurities, carbon monooxide for example, whose collision cross section with electrons are large. In chapter IV, the influence of the ionization instability on the power density and stable region free from the ionization instability under various seed fractions are investigated at relatively high pressures [26] at which an MHD generator will be coupled with HTGR in the future.

In the nonequilibrium MHD generation experiment, the electron temperature is a very important parameter and particularly that of the core region of the plasma is desired most to be known. There are several methods for electron temperature measurements, among which an optical method will be most superior as it affects the MHD plasma condition least. Hence line-reversal method is frequently used as the resonance lines of seeding alkali atoms are available. For the optically thick plasma as such MHD plasma, however, the temperature distribution in the boundary layer has a large influence on the measured line-reversal temperature[10], which makes it difficult to guess electron temperatures of core regions of the plasma from these measured line-reversal temperatures. In chapter V, the influence of the temperature distribution and the measuring configuration on the line-reversal temperature is theoretically investigated.

I. ELECTRICAL CHARACTERISTICS OF MHD GENERATOR IN A NONUNIFORM GAS PLASMA[38]

I.1. Introduction

In a magnetohydrodynamic (MHD) generation the applied magnetic field strength is desired to be as high as possible, since the power output is proportional to field strength squared. However, high fields result in high Hall parameters which are apt to incur undesirable phenomena such as the current concentration on the electrode edge or the ionization instability. When such phenomena occur, nonuniform characteristics of the plasma are further emphasized to a considerable degree, leading to a serious deterioration of the MHD performances. In the practical applications of the MHD generator, it is not likely that the perfect uniformity will appear, and the appearance of such nonuniformity should be rather taken for granted. Thus, in order to realize effective MHD generation, much efforts must be made for lessening the degree of the nonuniformity. In this chapter, the effects of the nonuniformity on the performance of the MHD generation are estimated in a more general manner than in reference [1].

I.2. Derivation of equations

Equations of the nonuniformity are derived and the effective electrical conductivity and the Hall parameter in case of isotropic and anisotropic nonuniformity are calculated. Then the influence of the nonuniformity on the specific power density in a Faraday-type or a Hall-type MHD generator is investigated and furthermore the relation between the nonequilibrium ionization and the nonuniformity is discussed.

First, the governing equations including the effects of the nonuniformity are briefly outlined according to Rosa[1].
Ohm's law for a gas including ion-slip may be written

$$\bar{j} = \sigma\bar{E}^* - (\beta_e/B)\bar{j}\times\bar{B} + (\beta_e\beta_i/B^2)(\bar{j}\times\bar{B})\times\bar{B}, \qquad (1.1)$$

$$\bar{E}^* = \bar{E} + \bar{u}\times\bar{B} + \bar{\nabla}p_e/en_e, \qquad (1.2)$$

where $\bar{j}$ is the current density, $\bar{E}^*$ the sum of all electric fields and motional emf's measured in the coordinate system of the observer, σ the scalar electrical conductivity of the gas, $\bar{u}$ the velocity of the gas, $\bar{B}$ the applied magnetic field, p_e the electron pressure, n_e the electron number density, e the elementary electric charge, β_e and β_i being the electron and ion Hall parameters, respectively.

In deducing equations, $\bar{u}$ and $\bar{B}$ are sssumed to be constant and σ,β_e and β_i are also assumed to be a function of p only, i.e., the nonuniformity is in the form of planes parallel to the q-r plane(see Fig.1.1). Although this is not a very general form of the nonuniformity, it gives some simplified mathematical expressions and approximation to the situation where the nonuniformity exists. It is, however, true for the case of the nonuniformity caused by the plane wave due to the ionization instability.

The components of Eq.(1.1) are found to be

$$j_x = \Sigma E_x^* - \Omega j_y, \qquad (1.3)$$

$$j_y = \Sigma E_y^* + \Omega j_x, \qquad (1.4)$$

or

$$j_p = \Sigma E_p^* - \Omega j_q, \qquad (1.5)$$

$$j_q = \Sigma E_q^* + \Omega j_p, \qquad (1.6)$$

where

$$\Sigma = \sigma/(1+\beta_e\beta_i), \qquad (1.7)$$

$$\Omega = \beta_e/(1+\beta_e\beta_i). \qquad (1.8)$$

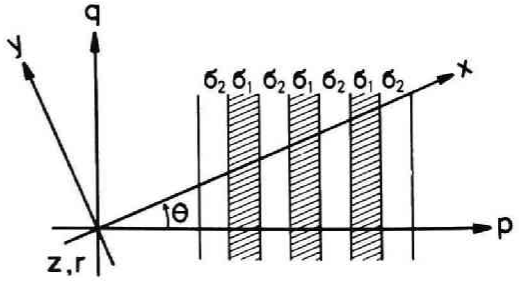

Fig.1.1. Coordinate system and nonuniformity. Plasma flows in the positive x direction and magnetic field is applied in the positive z direction.

Equations relating two coordinate systems (p,q,r) and (x,y,z) are

$$j_x = j_p cos\theta + j_q sin\theta, \tag{1.9}$$

$$j_y = -j_p sin\theta + j_q cos\theta, \qquad (-\pi/2 \leq \theta \leq \pi/2), \tag{1.10}$$

where θ is the angle made by the x and the p axes measured from the p axis. The assumption that j_q and E_p are functions of p only will be an imposed boundary condition and the relations for a steady state situation

$$div\ \overline{j} = 0, \tag{1.11}$$

$$rot\ \overline{E}^* = rot\ \overline{E} + rot(\overline{u}\times\overline{B}) = 0, \tag{1.12}$$

imply that a perpendicular component of the current density $\overline{j}$ and a tangential component of the electric field $\overline{E}^*$ are continuous across the surface of discontinuity and are independent of p and q. Hence,

$$j_p = const., \tag{1.13}$$

$$E_q^* = const. \tag{1.14}$$

Eliminating j_q from Eqs. (1.5) and (1.6), one obtains

$$\{(1+\Omega^2)/\Sigma\} j_p = E_p^* - \Omega E_q^*. \tag{1.15}$$

Since j_p and E_q^* are constant, Eqs.(1.6) and (1.15) may be integrated over the direction p immediately to yield

$$<j_q> = <\Sigma>E_q^* + <\Omega>j_p, \tag{1.16}$$

$$<(1+\Omega^2)/\Sigma> \cdot j_p = <E_p^*> - <\Omega>E_q^*, \tag{1.17}$$

where the branket < > means an average over the direction p perpendicular to the surface of discontinuity, or

$$<F> \equiv <F>_p = (1/L)\int_0^L F dp. \tag{1.18}$$

A set of averaged equations over p analogous to the original equations (1.5) and (1.6) are derived from Eqs.(1.16) and (1.17):

$$j_p = (<\Sigma>/G)<E_p^*> - (<\Omega>/G)<j_q>, \tag{1.19}$$

$$<j_q> = <\Sigma>E_q^* + <\Omega>j_p, \tag{1.20}$$

where

$$G = \langle\Sigma\rangle\langle(1+\Omega^2)/\Sigma\rangle-\langle\Omega\rangle^2. \tag{1.21}$$

This G was first defined by Rosa[1] to indicate the degree of non-uniformity.

We next consider averages of Eqs.(1.9) and (1.10) in order to obtain equations analogous to Eqs.(1.19) and (1.20) in the coordinate system (x,y,z). Average of j_x over x from Eq.(1.9) with previous assumptions yields

$$\begin{aligned}\langle j_x\rangle_x &= (1/L)\int_0^L j_x dx = (1/L)\int_0^L (j_p\cos\theta+j_q\sin\theta)dx \\ &= (1/L\cos\theta)\int_0^{L\cos\theta}(j_p\cos\theta+j_q\sin\theta)dp \\ &= \langle j_p\rangle\cos\theta+\langle j_q\rangle\sin\theta. \end{aligned}\tag{1.22}$$

Similarly,

$$\langle j_x\rangle_s = \langle j_x\rangle_p, \tag{1.23}$$

unless the arbitrary direction s is perpendicular to the direction p. Therefore, we denote these averages independent of the direction by the branket $\langle\ \rangle_s$ hereafter. If one eliminates j_p,$\langle j_q\rangle$,$\langle E_p^*\rangle$ and E_q^* from Eqs.(1.19) and (1.20), equations expressed by the terms in the coordinate system (x,y,z) are obtained as

$$(G\cos^2\theta+\sin^2\theta)\langle j_x\rangle_s+\{\langle\Omega\rangle-(G-1)\cos\theta\sin\theta\}\langle j_y\rangle_s = \langle\Sigma\rangle\langle E_x^*\rangle_s, \tag{1.24}$$

$$\{\langle\Omega\rangle+(G-1)\cos\theta\sin\theta\}\langle j_x\rangle_s-(G\sin^2\theta+\cos^2\theta)\langle j_y\rangle_s = -\langle\Sigma\rangle\langle E_y^*\rangle_s. \tag{1.25}$$

Consequently, Eqs.(1.24) and (1.25) may be written as

$$\langle j_x\rangle_s = (\langle\Sigma\rangle/G_{11})\langle E_x^*\rangle_s-(\langle\Omega\rangle/G_{12})\langle j_y\rangle_s, \tag{1.26}$$

$$\langle j_y\rangle_s = (\langle\Sigma\rangle/G_{21})\langle E_y^*\rangle_s+(\langle\Omega\rangle/G_{22})\langle j_x\rangle_s, \tag{1.27}$$

where

$$G_{11} = G\cos^2\theta+\sin^2\theta, \tag{1.28}$$

$$G_{12} = G_{11}\langle\Omega\rangle/\{\langle\Omega\rangle-(G-1)\cos\theta\sin\theta\}, \tag{1.29}$$

$$G_{21} = G\sin^2\theta + \cos^2\theta, \tag{1.30}$$

$$G_{22} = G_{21}\langle\Omega\rangle/\{\langle\Omega\rangle + (G-1)\cos\theta\sin\theta\}. \tag{1.31}$$

Comparing Eqs.(1.26),(1.27) with Eqs.(1.3),(1.4), electrical conductivities are reduced by the factor of $1/G_{11}$ and $1/G_{21}$, respectively, and Hall parameters by the factor of $1/G_{12}$ and $1/G_{22}$, respectively. It is seen from Eqs.(1.28)-(1.31) that G_{11} is not generally equal to G_{21} as well as G_{12} not to G_{22}. Since G is greater than (in case of nonuniformity) or equal to (in case of perfect uniformity) unity, G_{11} and G_{21} are always greater than or equal to unity according to G value, whereas G_{12} and G_{22} can be negative or less than unity when the angle θ is taken into account.

In order to estimate the influence of the nonuniformity on the averaged electrical conductivity and the averaged Hall parameter, assumptions will be made following Rosa[1], that the local Hall parameter is constant and the gas is made up of layers whose conductivity alternates between σ_1 and σ_2(see Fig.1.1). In this case the degree of fluctuation f is defined as

$$f = \Delta\sigma/(\sigma_1+\sigma_2) = (\sigma_1-\sigma_2)/(\sigma_1+\sigma_2). \tag{1.32}$$

Under these assumptions, Eq.(1.21) is reduced to

$$G = (1+\Omega^2 f^2)/(1-f^2). \tag{1.33}$$

When f is referred to hereafter in the calculation, the assumptions just mentioned are always implicitly made.

In case of $\theta=0$ and $\pm\pi/2$, G_{ij} is reduced to G or unity as follows:

$$\theta=0; \qquad G_{11} = G_{12} = G, \quad G_{21} = G_{22} = 1, \tag{1.34}$$

$$\theta=\pm\pi/2; \qquad G_{21} = G_{22} = G, \quad G_{11} = G_{12} = 1. \tag{1.35}$$

G_{ij} at the negative angle θ' can be easily found to be

$$G_{1j}(\theta') = G_{2j}(\theta); \quad j=1,2 \ (0<\theta<\pi/2), \tag{1.36}$$

$$G_{2j}(\theta') = G_{1j}(\theta); \quad j=1,2 \ (0<\theta<\pi/2), \tag{1.37}$$

from Eqs.(1.28)-(1.31), when the relation $\theta'=\theta-\pi/2$ holds.

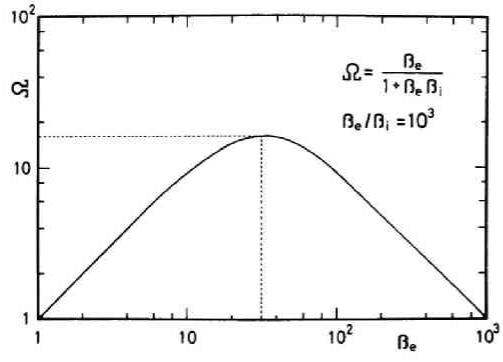

Fig.1.2. Ω vs. β_e.

In Fig.1.2 Ω vs. β_e is shown with the assumption of $\beta_e/\beta_i=10^3$. Here the ratio of β_e to β_i is arbitrarily assumed to be 10^3, but this value gives reasonable order to the ratio, since it is approximately proportional to the square root of m_i/m_e, where m_i and m_e are mass of ion and electron, respectively. In the actual MHD generation, however, the range of the Hall parameter is usually not so large as to be very sensitive to the value of β_e/β_i. It is evidently seen that Ω takes maximum at $\beta_e=\sqrt{10^3}$.

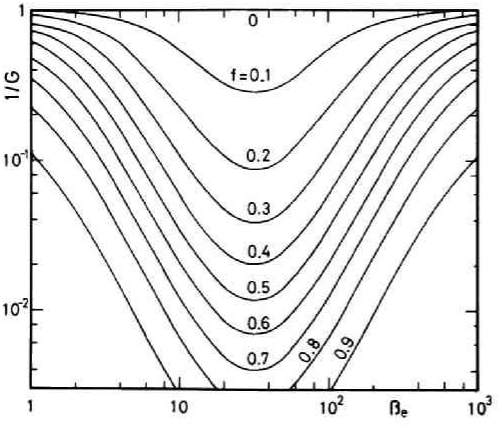

Fig.1.3. 1/G vs. β_e.

In Figs.1.3,1.4 and 1.5 inverses of G and G_{ij} at $\theta=0$, $\pi/6$ and $\pi/4$ are shown with the assumption of $\beta_e/\beta_i=10^3$. It is seen that inverses of G and G_{ij} take the minimum at $\beta_e=\sqrt{10^3}$. When the degree of fluctuation f increases, inverse G_{ij} remarkably decreases with increasing Ω and any inverse G_{ij} except G_{12}^{-1} are greater than inverse G. This is because the effect of the nonuniformity

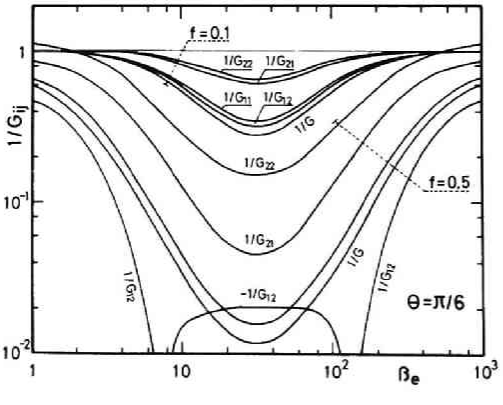

Fig.1.4. $1/G_{ij}$ vs. β_e for $\theta=\pi/6$.

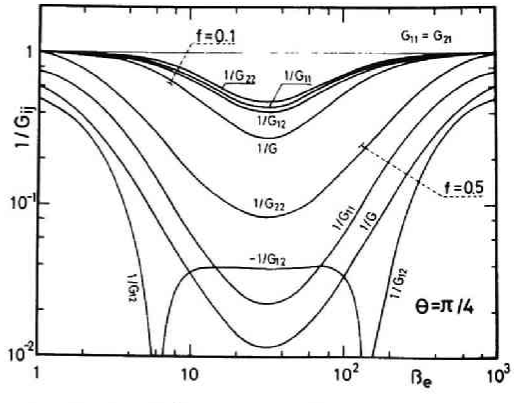

Fig.1.5. $1/G_{ij}$ vs. β_e for $\theta=\pi/4$.

is thought to be the greatest when the x axis is parallel to the p axis, i.e., in the case of $\theta=0$. As mentioned before, inverse G_{22} can be greater than unity in the region of small Ω and it becomes remarkably large when the angle θ is small.

I.3. Effective electrical conductivity and Hall parameter in a nonuniform gas plasma

The effective electrical conductivity and the effective Hall parameter are defined, respectively as

$$\sigma_{eff} = \langle\bar{j}\rangle^2/\langle\bar{j}\rangle\cdot\langle\bar{E}^*\rangle, \tag{1.38}$$

$$\beta_{eff} = |\langle\bar{j}\rangle\times\langle\bar{E}^*\rangle|/(\langle\bar{j}\rangle\cdot\langle\bar{E}^*\rangle). \tag{1.39}$$

These quantities in case of isotropic and anisotropic nonuniformity but not stochastic are discussed below.

I.3.1. Isotropic nonuniformity for constant f

In the case of isotropic nonuniformity, σ_{eff} and β_{eff} can be calculated from Eqs.(1.24) and (1.25) as averages over the angle under the assumption that the direction x rotates with a uniform angular velocity around $\bar{B}$ keeping f constant, that is

$$\sigma_{eff}/\langle\Sigma\rangle = (1/\pi\langle\Sigma\rangle)\int_{-\pi/2}^{\pi/2}(\langle j_x\rangle_s/\langle E_x^*\rangle_{\langle j_y\rangle_s=0})\,d\theta$$

$$= 1/\sqrt{G} = \{(1-f^2)/(1+\Omega^2 f^2)\}^{1/2}. \tag{1.40}$$

In deducing this relationship, it was assumed that β_e is constant and only σ varies in the direction p alternating between σ_1 and σ_2 as mentioned before. Similarly, the effective Hall parameter is given as

$$\beta_{eff} = (1/\pi)\int_{-\pi/2}^{\pi/2}|\langle E_y^*\rangle_s/\langle E_x^*\rangle_{\langle j_y\rangle_s=0}|\,d\theta$$

$$= \Omega\{(1-f^2)/(1+\Omega^2 f^2)\}^{1/2}. \tag{1.41}$$

From Eqs.(1.40) and (1.41) the following relation is deduced for a

constant Hall parameter to yield

$$\sigma_{eff}/\langle\sigma\rangle = \beta_{eff}/\beta_e. \tag{1.42}$$

In the limit of a large Ω the effective electrical conductivity and the effective Hall parameter are given for $1/\Omega<f<1$

$$lim\ \sigma_{eff} = \langle\Sigma\rangle/(\Omega\cdot f), \tag{1.43}$$

$$lim\ \beta_{eff} = 1/f. \tag{1.44}$$

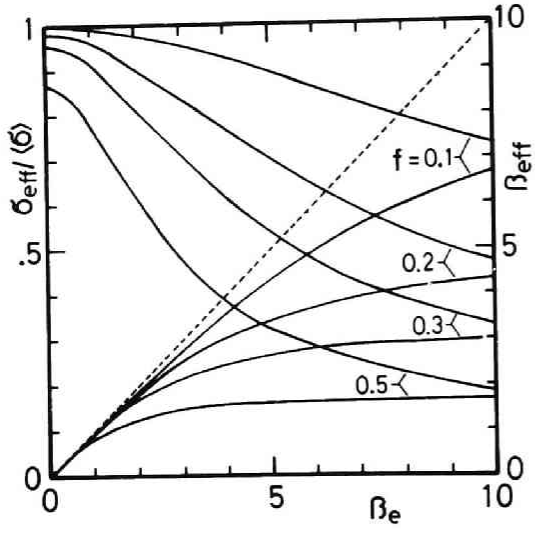

Fig.1.6. Effective electrical conductivity and Hall parameter vs. β_e for isotropic nonuniformity.

In Fig.1.6 the relations of $\sigma_{eff}/\langle\sigma\rangle$ and β_{eff} for various degrees of fluctuation f in case of $\beta_e/\beta_i=10^3$ are shown as a function of β_e at the region below $\beta_e=10$ where the ion-slip effect is negligible.

It should be noted that $\sigma_{eff}/\langle\sigma\rangle$ is not equal to unity even at $\beta_e=0$, as being pointed out by Rosa[3], due to the presence of nonuniformity and reduces to $(1-f^2)^{1/2}$ from Eq.(1.40). As for the nonuniformity caused by the ionization instability, this instability occurs suddenly when the Hall parameter β_e exceeds the critical Hall parameter β_{cr}. Hence $\sigma_{eff}/\langle\sigma\rangle$ holds unity until β_e becomes β_{cr} and then begins to decrease according to the degree of the induced nonuniformity. The experimental data obtained by other authors[35,36] show good agreement with the curves of $f=0.3$-0.5 in Fig.1.6.

I.3.2. Anisotropic nonuniformity for constant θ

Another model is to imagine anisotropic nonuniformity whose degree fluctuates with time from zero to f_m for the fixed direction. Using Eqs.(1.24) and (1.25), we obtain σ_{eff} and β_{eff} by integrating over f as

$$\sigma_{eff}/\langle\Sigma\rangle = (1/f_m\langle\Sigma\rangle)\int_0^{f_m}(\langle j_x\rangle_s/\langle E_x^*\rangle_s)\Big|_{\langle j_y\rangle_s=0} df$$

$$= c_1\{f_m+(c_1-1)I\}/f_m, \tag{1.45}$$

$$\beta_{eff}/\Omega = (1/f_m\Omega)\int_0^{f_m}\left|\langle E_y^*\rangle_s/\langle E_x^*\rangle_s\right|_{\langle j_y\rangle_s=0} df$$

$$= -c_1/c_2-\{c_1(c_1+c_2)/(f_m c_2)\}I, \tag{1.46}$$

where

$$c_1 = 1/(\sin^2\theta-\Omega^2\cos^2\theta), \tag{1.47}$$

$$c_2 = 2\Omega/\{(1+\Omega^2)\sin 2\theta-2\Omega\}, \tag{1.48}$$

$$I = \int_0^{f_m} df/(f^2-c_1). \tag{1.49}$$

The definite integral I is expressed according to a positive or a negative value of c_1 by

$$I = (1/\sqrt{-c_1})\arctan(f_m/\sqrt{-c_1}); \qquad c_1<0, \tag{1.50}$$

$$= (1/2\sqrt{c_1})\ln\{(\sqrt{c_1}-f_m)/(\sqrt{c_1}+f_m)\}; \quad c_1 \geqq 1 \geqq f_m. \tag{1.51}$$

Since c_1 can not become zero unless Ω goes to infinity, the case of $c_1=0$ can be eliminated from the practical point of view. Consequently, σ_{eff} and β_{eff} are explicitly expressed in terms of c_1, c_2 and f_m as

$$\sigma_{eff}/\langle\Sigma\rangle = c_1+\{\sqrt{-c_1}(1-c_1)/f_m\}\arctan(f_m/\sqrt{-c_1}); \quad c_1<0, \tag{1.52}$$

$$= c_1-\{\sqrt{c_1}(1-c_1)/2f_m\}\ln\{(\sqrt{c_1}-f_m)/(\sqrt{c_1}+f_m)\}; \quad c_1 \geqq 1 \geqq f_m, \tag{1.53}$$

$$\beta_{eff}/\Omega = -c_1/c_2+\{\sqrt{-c_1}(1+c_1/c_2)/f_m\}\arctan(f_m/\sqrt{-c_1}); \quad c_1<0, \tag{1.54}$$

$$= -c_1/c_2-\{\sqrt{c_1}(1+c_1/c_2)/2f_m\}\ln\{(\sqrt{c_1}-f_m)/(\sqrt{c_1}+f_m)\}; \quad c_1 \geqq 1 \geqq f_m. \tag{1.55}$$

In the limit of the degree of fluctuation, σ_{eff} and β_{eff} are expressed as

$$\lim_{f_m \to 0}(\sigma_{eff}/\langle\Sigma\rangle) = 1, \tag{1.56}$$

$$\lim_{f_m \to 0} (\beta_{eff}/\Omega) = 1, \tag{1.57}$$

and for large β_e in the case where the ion-slip effect can be neglected

$$\lim (\sigma_{eff}/\langle\sigma\rangle) = \pi/(2\beta_e f_m), \qquad \theta=0, \tag{1.58}$$

$$\lim \beta_{eff} = \pi/(2\beta_e f_m), \qquad \theta=0. \tag{1.59}$$

On the other hand, at $\beta_e=0$ for $\theta\neq 0$, $\sigma_{eff}/\langle\sigma\rangle$ is reduced to

$$\sigma_{eff}/\langle\sigma\rangle = 1/\sin^2\theta + (\cos^2\theta/2f_m\sin^3\theta)\ln\{(1-f_m\sin\theta)/(1+f_m\sin\theta)\}, \tag{1.60}$$

and this term is always less than unity unless f_m is equal to zero[38].

In Figs.1.7 and 1.8 $\sigma_{eff}/\langle\sigma\rangle$ and β_{eff} vs. β_e are shown for $\theta=0$, $\pm\pi/4$ in the anisotropic nonuniformity. It is to be noted that when $\theta=\pi/2$ both of them are reduced to unity and Ω, respectively, as is seen from Eqs.(1.53) and (1.55). With increasing θ, which is the direction of lessening influence of discontinuity, the decreasing rate of $\sigma_{eff}/\langle\sigma\rangle$ becomes smaller and the increasing rate of β_{eff} becomes larger. Compared with those in Fig.1.6, both of $\sigma_{eff}/\langle\sigma\rangle$ and β_{eff} in case of the anisotropic nonuniformity are larger even at $\theta=0$.

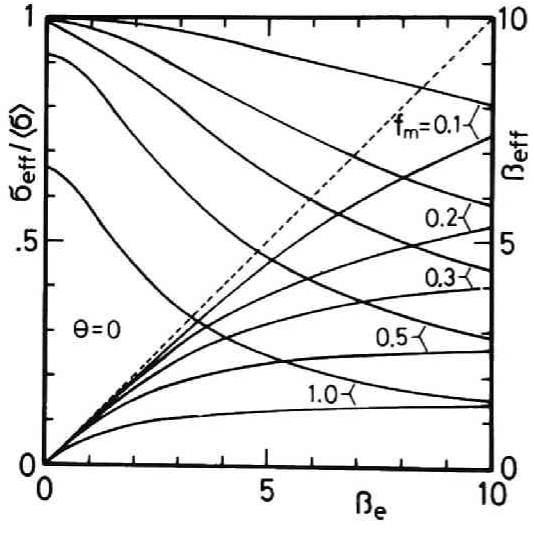

Fig.1.7. Effective electrical conductivity and Hall parameter vs. β_e for anisotropic nonuniformity at $\theta=0$.

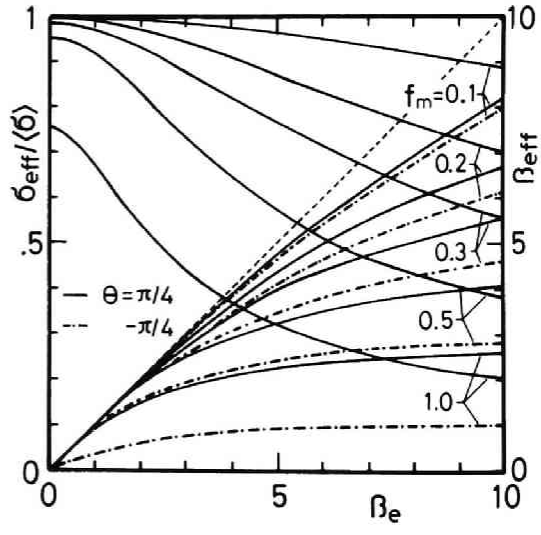

Fig.1.8. Effective electrical conductivity and Hall parameter vs. β_e for anisotropic nonuniformity at $\theta=\pm\pi/4$.

I.4. Power densities of MHD generators in a nonuniform gas plasma

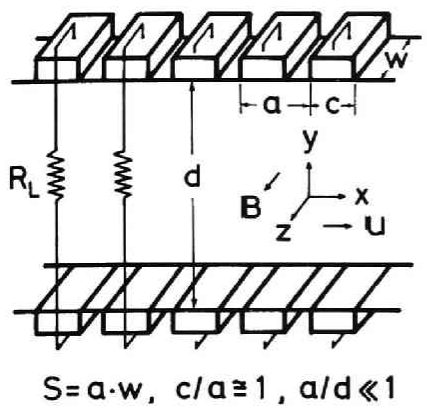

Fig.1.9. Configuration of MHD generator channel with finely segmented electrodes.

Under the existence of nonuniformity, power densities of an MHD generator are discussed. The configuration of the MHD generator channel with finely segmented electrode is shown in Fig.1.9. In deducing equations, $\overline{\nabla p_e}$ in Eq.(1.2) is neglected.

I.4.1. Faraday-type MHD generator

The power density P_e may be written by

$$P_e = -\overline{j}\cdot\overline{E}. \tag{1.61}$$

If P_e is averaged over the direction perpendicular to the surface of discontinuity,

$$\langle P_e\rangle = -(j_p\cdot\langle E_p\rangle+\langle j_q\rangle\cdot E_q) = -(\langle j_x\rangle_s\langle E_x\rangle_s+\langle j_y\rangle_s\langle E_y\rangle_s). \tag{1.62}$$

Since the Hall component of the current density $\langle j_x\rangle_s$ is equal to zero, the averaged power density may be written as

$$\begin{aligned}\langle P_e\rangle_F &= -\langle j_y\rangle_s\langle E_y\rangle_s = -(\langle\Sigma\rangle/G_{21})\langle E_y^*\rangle_y\langle E_y\rangle_y \\ &= (\langle\Sigma\rangle/G_{21})K_F(1-K_F)u^2B^2,\end{aligned} \tag{1.63}$$

where the load factor K_F is defined as

$$K_F = \langle E_y\rangle_y/(uB). \tag{1.64}$$

The maximum power density is obtained obviously at $K_F=1/2$ and $G=1$ as

$$\langle P_e\rangle_{Fmax} = \langle\Sigma\rangle u^2B^2/4. \tag{1.65}$$

I.4.2. Hall-type MHD generator

The normal component of the electric field $\langle E_y \rangle_s$ being zero, the power density of the Hall-type MHD generator may be similarly written as

$$\langle P_e \rangle_H = -\langle j_x \rangle_y \cdot \langle E_x \rangle_x, \tag{1.66}$$

$$\langle E_y^* \rangle_y = -uB. \tag{1.67}$$

Elimination of $\langle j_y \rangle_s$ from Eqs.(1.26) and (1.27) with use of Eq.(1.67) yields

$$\langle j_x \rangle_y = \frac{G_{12} \cdot G_{22} \langle \Sigma \rangle}{G_{11}(\langle \Omega \rangle^2 + G_{12} \cdot G_{22})} \left(\langle E_x \rangle_x + \frac{G_{11}}{G_{12} G_{21}} \langle \Omega \rangle uB \right) \tag{1.68}$$

If we denote a load factor of a Hall-type MHD generator as the ratio of the actual electric field to that in the open-circuit, similarly as the load factor of a Faraday-type MHD generator, it is expressed from Eq.(1.68) as

$$K_H = -\langle E_x \rangle_x \Big/ \left(\frac{G_{11}}{G_{12} G_{21}} \langle \Omega \rangle uB \right) = \zeta \cdot K_O, \tag{1.69}$$

where

$$\zeta = \frac{G_{12} G_{21}}{G_{11}} = \frac{\langle \Omega \rangle \{(G-1)\sin^2\theta + 1\}}{\langle \Omega \rangle - (G-1)\cos\theta \cdot \sin\theta}, \tag{1.70}$$

$$K_O = -\langle E_x \rangle_x / (\langle \Omega \rangle uB). \tag{1.71}$$

Since ζ reduces to unity at $G=1$ or $\theta=0$, K_H becomes the same as K_O which is a usual notation of a Hall-type MHD generation in a uniform plasma. With use of Eqs.(1.69),(1.70) and (1.71), $\langle j_x \rangle_y$ is reduced to

$$\langle j_x \rangle_y = \frac{\langle \Omega \rangle - (G-1)\cos\theta \cdot \sin\theta}{G + \langle \Omega \rangle^2} \langle \Sigma \rangle uB(1-K_H). \tag{1.72}$$

Another component $\langle j_y \rangle_x$ is written in the form as

$$\langle j_y \rangle_x = -\frac{\langle \Sigma \rangle uB}{G + \langle \Omega \rangle^2} \cdot \frac{G + K_H \langle \Omega \rangle^2 + (G-1)^2 \cos^2\theta \sin^2\theta (1-K_H)}{G\sin^2\theta + \cos^2\theta}, \tag{1.73}$$

Consequently, the power density is obtained by substituting Eqs.(1.69) and (1.72) into Eq.(1.66) as

$$\langle P_e \rangle_H = \frac{\{\langle\Omega\rangle-(G-1)\cos\theta\cdot\sin\theta\}^2}{(G+\langle\Omega\rangle^2)(G\sin^2\theta+\cos^2\theta)}\langle\Sigma\rangle u^2B^2K_H(1-K_H). \qquad (1.74)$$

Normalized power densities of a Faraday- and a Hall-type MHD generators are defined, respectively, as

$$\langle P_e \rangle_F = \langle P_e \rangle_F / \langle P_e \rangle_{Fmax} = 4K_F(1-K_F)/G_{21} = \frac{4K_F(1-K_F)}{(G-1)\sin^2\theta+1} \qquad (1.75)$$

$$\langle P_e \rangle_H = \langle P_e \rangle_H / \langle P_e \rangle_{Fmax} = \frac{4K_H(1-K_H)\{\langle\Omega\rangle-(G-1)\cos\theta\sin\theta\}^2}{(G+\langle\Omega\rangle^2)\{(G-1)\sin^2\theta+1\}} \qquad (1.76)$$

It is obviously seen from Eqs.(1.75) and (1.76) that the maximum $\langle P_e \rangle_F$ and $\langle P_e \rangle_H$ are both achieved at $K_F=K_H=0.5$. With respect to $\langle P_e \rangle_F$, inverse G_{21} in Figs.1.3, 1.4 and 1.5 should be referred to. In Figs. 1.10, 1.11 and 1.12 the maximum ($K_H=0.5$) normalized power densities of a Hall generator $\langle P_e \rangle_H$ at $\theta=0$ and $\pm\pi/4$ are shown. In case of $\theta=0$ in Fig.1.10 $\langle P_e \rangle_H$ increases monotonously with increasing Ω and stays at considerably high level until large degree of fluctuation in the region above $\Omega\simeq3$. It is notable that the decreasing rate of $\langle P_e \rangle_H$ with respect to f is very small for small f and very large for large f,

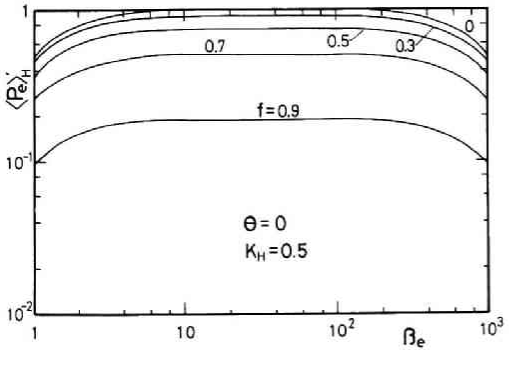

Fig.1.10. Normalized power density of a Hall-type MHD generator vs. β_e for $\theta=0$, $K_H=0.5$.

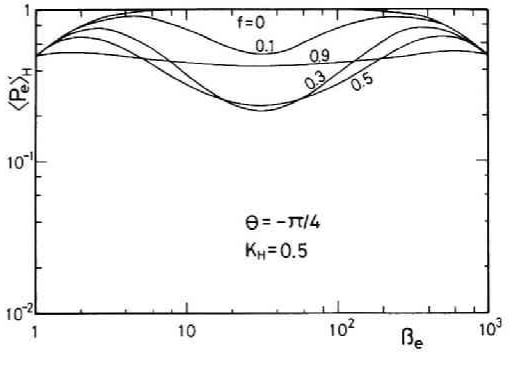

Fig.1.11. Normalized power density of a Hall-type MHD generator vs. β_e for $\theta=-\pi/4$, $K_H=0.5$.

since $\langle P_e \rangle_H$ is proportional to $(1-f^2)$ at $\theta=0$. In Fig.1.11 $\langle P_e \rangle_H$ at a negative angle of $\theta=-\pi/4$ for $K_H=0.5$ is shown. It is very interesting that $\langle P_e \rangle_H$ at $f=0.9$ exceeds those at smaller degrees of fluctuation in the region of considerably large Ω. This is because when f approaches unity, the direction of the current makes the angle $-\pi/4$ with the x axis, i.e., the current is forced to flow only in the layer of higher conductivity, resulting in $\langle P_e \rangle_H=0.5$ independent of β_e. When θ is negative, the inclination of the layer generally agrees with the current direction of the normal Hall generation and hence favorable performances of the Hall generation may be achieved as seen in Fig.1.11..

On the other hand for the positive angles, since the inclination of the layer is generally opposite to the current direction of the normal Hall generation, only the small positive Hall current is, if possible, achieved, resulting in a serious decrease of the power output of $\langle P_e \rangle_H$. When f approaches unity, the current is also forced to flow in the layer of higher conductivity, which makes an angle of $-3\pi/4$ with the x axis in case of Fig.1.12, thus resulting in the negative $\langle j_x \rangle_y$. The limiting absolute value of $\langle j_x \rangle_y$ is, however, the same as that at the negative angle of $\theta=-\pi/4$ for $f=1$ and hence $\langle P_e \rangle_H$ becomes similarly as large as 0.5. As far as the practical Hall generation is concerned, it is, however, quite unlikely that the nonuniformity corresponding to the positive angle θ will macroscopically occur. It should be noted as a conclusion that the normalized power density $\langle P_e \rangle_H$ of the Hall generation can be expected to be considerably high as long as the angle θ stays in the negative region.

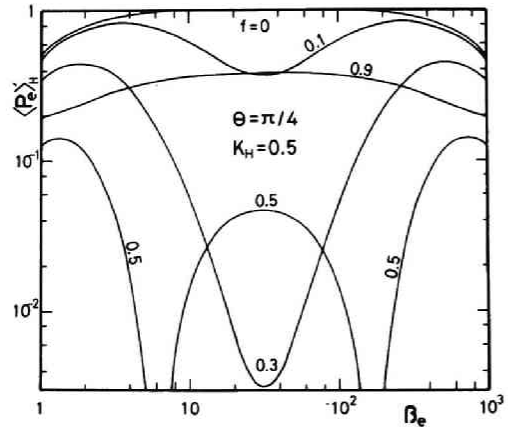

Fig.1.12. Normalized power density of a Hall-type MHD generator vs. β_e for $\theta=\pi/4$, $K_H=0.5$.

The averaged electrical efficiencies η_F and η_H for a Faraday- and a Hall-type MHD generation are defined, respectively, as

$$\eta_F = K_F \tag{1.77}$$

$$\eta_H = \langle -\vec{j}\cdot\vec{E}\rangle_H / (\langle \vec{j}\cdot\vec{E}^*\rangle_H + \langle -\vec{j}\cdot\vec{E}\rangle_H) = \langle j_x\rangle\langle E_x\rangle / (\langle j_y\rangle uB)$$

$$= \frac{K_H(1-K_H)\{\beta_e-(G-1)\cos\theta\cdot\sin\theta\}^2}{G+K_H\beta_e^2+(1-K_H)(G-1)^2\cos^2\theta\sin^2\theta} . \tag{1.78}$$

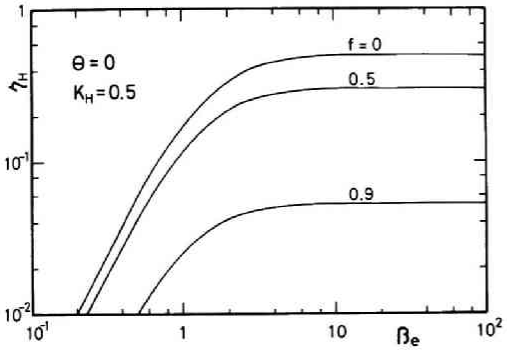

Fig.1.13. Electrical efficiency of a Hall-type generator vs. β_e for $\theta=0$, $K_H=0.5$.

It should be noted that when β_e becomes large, η_H approaches K_H unless θ is $\pm\pi/2$ or 0 and the following relation holds

$$\eta_H(-\theta) = \eta_H(\theta-\pi/2), \quad 0\leqq\theta\leqq\pi/2 \tag{1.79}$$

In Fig.1.13 η_H vs. β_e is shown for $\theta=0$. When f increases, it is difficult for the Hall current to flow in the x direction due to the large nonuniformity in the x direction, and hence η_H at smaller f is larger than that at larger f.

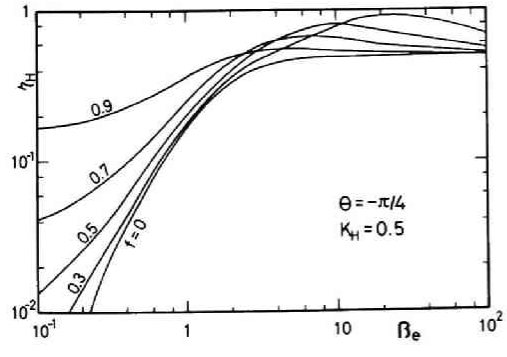

Fig.1.14. Electrical efficiency of a Hall-type generator vs. β_e for $\theta=-\pi/4$, $K_H=0.5$.

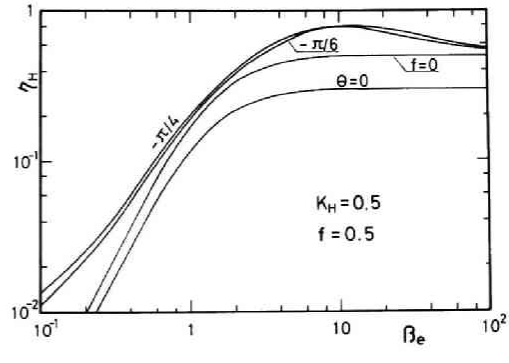

Fig.1.15. Electrical efficiency of a Hall-type generator vs. β_e for $f=0.5$, $K_H=0.5$.

For negative θ, on the other hand, every η_H for $f>0$ exceeds that for $f=0$ as seen in Fig.1.14. This is because such an inclination of the layer is highly favorable to the influence of the Hall effects on a Hall-type MHD generation. The dependence of η_H on the angle θ is shown in Fig.1.15. It is seen that when the effects of the nonuniformity is thought to be the strongest on the Hall current ($\theta=0$), the electrical efficiency is the lowest, and η_H becomes maximum for cases of $\theta\neq 0$. It is to be noted that η_H at $\theta=-\pi/6$ (or $-\pi/3$) or $-\pi/4$ is far larger than that at $f=0$ and $K_H=0.5$ in the region near $\beta_e=10$, and this is also true for large f. The reason is similar to that mentioned in reference to Fig.1.13.

I.5. Nonequilibrium ionization in a nonuniform gas plasma

In a closed cycle gas plasma MHD generation, such as a coolant rare gas of a HTGR or heatexchanged rare gas by the rejected combustion gas of an open cycle MHD generator is now being thought as a working gas. The temperature of these gases is, however, not so high as to be able to operate MHD generation in the thermal equilibrium state, which will lead to a very poor performance of the MHD generation. It is hence desirable or rather inevitable to operate MHD generation in the nonequilibrium state. The review of the nonequilibrium ionization is briefly stated below.

Since the mass of an electron is very small compared with that of an atom or an ion, the electron can be very easily accelerated resulting in the energy gain from the electric field, whereas it loses energy very little through collisions with atoms or ions due to large difference of masses. As a result, electrons can maintain the energy at the level higher than those maintained by atoms or ions, and the electron number density reaches its equilibrium state based not on the gas temperature but on the electron temperature. This phenomenon is usually stated as the nonequilibrium ionization. Once the effective nonequilibrium ionization is achieved, the electrical performances of MHD generation are highly improved, since the electrical conductivity of

the plasma is preferentially dependent on the electron temperature. The qualitative estimation of the nonequilibrium ionization will be made next.

The energy equation of electrons is written as

$$\frac{D}{Dt}\{n_e(\frac{3}{2}kT_e+eV_i)\}+n_e(\frac{3}{2}kT_e+eV_i)\bar{\nabla}\cdot\bar{u}+\bar{\nabla}\cdot\bar{q}_e+p_e\bar{\nabla}\cdot\bar{u}$$

$$=\bar{j}\cdot\bar{E}^*-\frac{3m_e}{2m_a}\delta kn_e\nu_e(T_e-T_g)-Q_r, \tag{1.80}$$

$$\bar{q}_e=-\lambda_e M\bar{\nabla}T_e-(\frac{5kT_e}{2e}+V_i)\bar{j}, \tag{1.81}$$

$$M=\frac{1}{1+\beta_e^2}\begin{pmatrix}1+\beta_x^2, & \beta_x\beta_y-\beta_z, & \beta_z\beta_x+\beta_y\\ \beta_x\beta_y+\beta_z, & 1+\beta_y^2, & \beta_y\beta_z-\beta_x\\ \beta_z\beta_x-\beta_y, & \beta_y\beta_z+\beta_x, & 1+\beta_z^2\end{pmatrix}, \tag{1.82}$$

$$\lambda_e=5n_ek^2T_e/(2m_e\nu_e), \tag{1.83}$$

$$p_e=n_ek\,T_e. \tag{1.84}$$

In the above, D/Dt is a mobil operator, and n_e, T_e, p_e and eV_i are electron number density, electron temperature, electron pressure and ionization energy of seed atoms, respectively. $\bar{q}_e$, δ, ν_e, k, T_g and Q_r are heat flux of electrons, collision loss parameter of electrons, collision frequency of electrons, Boltzmann's constant, gas temperature and radiation loss term, respectively. M and $\beta_j(=eB_j/m_e\nu_e)$ are the tensor Hall parameter and the Hall parameter based on the j-th component of $\bar{B}$ ($\beta_e^2=\beta_x^2+\beta_y^2+\beta_z^2$), m_e, m_a being mass of electron and atom, respectively.

In the steady state for a uniform gas in the absence of the radiation loss, Eq.(1.80) with use of Eq.(1.1) is reduced to the familiar form as[36]

$$j^2/\sigma=(3m_e/2m_a)\delta kn_e\nu_e(T_e-T_g). \tag{1.85}$$

In deducing Eq.(1.85), it was assumed that the effect of ion-slip can be neglected. The left-hand side of Eq.(1.85) denotes Joule dissipation in the plasma and Eq.(1.85) shows that the energy obtained from Joule heating(dissipation) is balanced by the energy dissipated through collisions with atoms, and the difference between the electron and the gas temperature is roughly proportional to Joule dissipation. If the Joule dissipation is spatially uniform, the electron temperature is also uniform in space as seen in Eq.(1.85) which corresponds to the case of $G=1$, realizing an ideal MHD generation. In the actual MHD generation, however, the spatially uniform electron temperature distribution which realizes an effective nonequilibrium ionization state can be hardly obtained due partly to some undesirable phenomena. One of them is the current concentration on the electrode edge by the Hall effect, for example, as will be discussed later. Although this phenomenon may be reduced to some degree by finely segmented electrodes, the degree of segmentation or the aspect ratio is practically restricted from technical point of view. Therefore, in the presence of the Hall effect, the current is still apt to concentrate on the electrode edge, and hence causes a seriously nonuniform Joule heating around the electrode edge leading often to a short-circuiting of the neighboring electrodes. These are both detrimental to the performance of MHD generation. The other phenomenon which causes also a serious nonuniformity in the MHD plasma is the ionization instability first indicated by Velikov et al.[15] and Kerrebrock[16]. When the Hall parameter exceeds the critical Hall parameter, the fluctuation wave of electron number density or temperature occurs and consequently results in a nonuniformity of the plasma parameters. These two phenomena, the current concentration on the electrode edge and the ionization instability, if occur, considerable nonuniformity often appears and the effective nonequilibrium ionization will hardly be realized as will be shown below.

In a Faraday-type MHD generator with finely segmented electrodes (see Fig.1.9) the local electron temperature is estimated from

Eq.(1.80) as

$$j^2/\sigma = \bar{j}\cdot\bar{E}^* = (3\delta/2\gamma)(uB/M)^2(\sigma/\beta_e^2)(T_e/T_g-1), \qquad (1.86)$$

where M is the Mach number in the plasma, and γ is the ratio of specific capacities. In using Eq.(1.80), it was assumed that $\bar{u}$ and $\bar{q}_e$ are constant, whereas other terms are uniform in the gas and Q_r can be neglected.

The averaged Faraday component of the electric field can be expressed by the averaged load factor K_F, and the averaged Hall component of the current density vanishes as

$$\langle j_x\rangle_y = 0, \qquad (1.87)$$

$$\langle E_y^*\rangle_y = \langle E_y\rangle_y - uB = (K_F-1)uB. \qquad (1.88)$$

The left-hand side of Eq.(1.86) may be written with use of Eqs.(1.27) and (1.63) as

$$\langle\bar{j}\cdot\bar{E}^*\rangle = \langle j_y\rangle_x(\langle E_y\rangle_y - uB) = \langle\sigma\rangle(1-K_F)^2(uB)^2/G_{21}. \qquad (1.89)$$

Average of Eq.(1.86) with use of Eq.(1.89) then yields

$$\langle T_e\rangle/T_g - 1 = (2\gamma/3\delta)M^2\beta_e^2(1-K_F)^2/G_{21}. \qquad (1.90)$$

In deducing Eq.(1.90), it was assumed that the Hall parameter is constant and the electron temperature is weakly dependent on the electron number density, whereas the electrical conductivity depends strongly on the electron temperature. In addition, the terms except for the electron were assumed to be constant and the effect of ion-slip was neglected. Eq.(1.90) shows that when the nonuniformity occurs, the degree of nonuniformity G plays an important role for the electron temperature elevation through G_{21} and only a small temperature elevation is expected in the case of a nonuniform plasma, which results in poor nonequilibrium MHD performances in a Faraday-type MHD generation.

In a Hall-type MHD generation, on the other hand, the averaged Joule dissipation term may be written as

$$\langle\bar{j}\cdot\bar{E}^*\rangle = \langle j_x\cdot E_x - j_y\cdot uB\rangle = \langle j_x\rangle\cdot\langle E_x\rangle\{1-\langle j_y\rangle uB/(\langle j_x\rangle\langle E_x\rangle)$$

$$= \langle P_e \rangle_H (1-\eta_H)/\eta_H$$

$$= \frac{\langle\sigma\rangle (uB)^2 \{G+[\beta_e K_H+(G-1)(1-K_H)\cos\theta\sin\theta]^2\}}{(G+\beta_e^2)(G\sin^2\theta+\cos^2\theta)}, \qquad (1.91)$$

Average of Eq.(1.86) together with Eq.(1.91) yields

$$\frac{\langle T_e \rangle - T_g}{T_{eo}-T_g} \simeq R_T$$

$$= \frac{(1+\beta_e^2)\{G+K_H\beta_e+(1-K_H)(G-1)\cos\theta\sin\theta\}}{(G+\beta_e^2)(G\sin^2\theta+\cos^2\theta)\{1+(K_H\beta_e)^2\}}, \qquad (1.92)$$

where T_{eo} is the ideal electron temperature in the uniform plasma, namely, for $G=1$. R_T vs. β_e is shown in Fig.1.16. In case of $\theta=0$ the averaged electrical conductivity $\langle\sigma\rangle$ becomes large since R_T exceeds unity, but as far as the averaged tensor conductivity is concerned, it is reduced by the factor of $1/G$ as a result. In general, R_T begins to decrease greatly when β_e exceeds about 2 in the case of $\theta\neq 0$, and consequently, the effective electron temperature elevation is hardly expected in these conditions. Much efforts to suppress the nonuniformity is hence required in order to realize the effective nonequilibrium ionization.

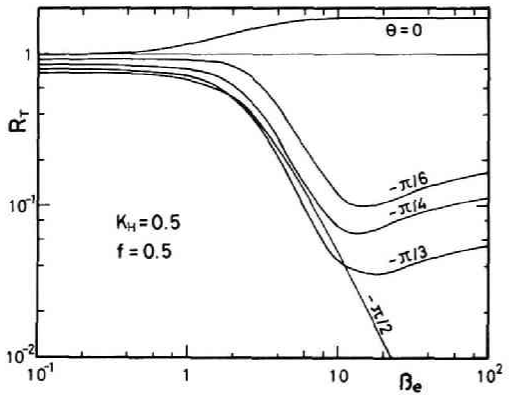

Fig.1.16. Relative electron temperature elevation vs. β_e for $f=0.5$, $K_H=0.5$.

I.6. Concluding remarks

When the angle θ is taken into account, the electrical characteristics of the MHD generation differs greatly from that at $\theta=0$ or $\pi/2$ which was previously calculated by Rosa[1], and the electrical conductivity and the Hall parameter in the averaged Ohm's law as in Eqs. (1.26) and (1.27) become tensor quantities expressed as

$$\langle \bar{j} \rangle_s = \langle \Sigma \rangle \begin{pmatrix} G_{11}^{-1}, & 0 \\ 0, & G_{21}^{-1} \end{pmatrix} \langle \bar{E}^* \rangle_s - \langle \Omega \rangle \begin{pmatrix} 0, & G_{12}^{-1} \\ -G_{22}^{-1}, & 0 \end{pmatrix} \langle \bar{j} \rangle_s . \qquad (1.93)$$

It is important that the inverses of G_{12} and G_{22} can be negative or greater than unity according to the relationship between Ω, G and θ, and the sign of G_{12} is identical with that of the Hall current $\langle j_x \rangle_y$ in case of Hall generation.

When the degree of fluctuation f increases, both the effective electrical conductivity and the effective Hall parameter are greatly reduced regardless of the isotropic or anisotropic nonuniformity. But the decreasing rate of σ_{eff} and the increasing rate of β_{eff} seem larger and smaller, respectively, in case of the isotropic nonuniformity than in case of the anisotropic one, in general, with increasing Hall parameters.

In a Faraday-type MHD generation, $\langle P_e \rangle_F$ is proportional to the inverse G_{21} and is considerably large in the region of small f and Ω, but when f or Ω increases, $\langle P_e \rangle_F$ decreases very rapidly to lead to a very poor performance of MHD generation. In case of a Hall-type MHD generation, on the other hand, $\langle P_e \rangle_H$ can take relatively large values for the negative angle θ, and even if the degree of fluctuation f is very close to unity, $\langle P_e \rangle_H$ still approaches 0.5 independent of β_e and exceeds those at smaller degree of fluctuation in the region of large Ω. Comparing $\langle P_e \rangle_F$ with $\langle P_e \rangle_H$, it turns out that the influence of the degree of fluctuation f on the former is far stronger than that on the latter. In the Hall generation, the region where the Hall current is negative can exist under the condition of the positive angle θ, whereas $\langle P_e \rangle_H$ is always positive independent of the sign of the Hall current. It is, however, very unlikely in the actual MHD generation that the negative Hall current will flow in a large scale.

With respect to the nonequilibrium ionization in a nonuniform gas plasma, the elevation of the electron temperature is much influenced

by the degree of nonuniformity and an effective one is scarcely expected, in general, when the degree of fluctuation is large. It is thus emphasized that much efforts must be made mainly towards lessening the degree of fluctuation to realize the effective MHD generation, particularly in a closed cycle gas plasma MHD generation.

II. ELECTRICAL CHARACTERISTICS OF MHD GENERATOR WITH RESISTIVE SEGMENTED ELECTRODES IN THERMAL EQUILIBRIUM[39]

II.1. Introduction

Many two-dimensional numerical analyses have been reported on the performance characteristics of equilibrium and nonequilibrium MHD generators[4,5,7,8], and attention has been drawn to the deterioration of generator performance due to the current concentration. This tendency of the current to concentrate around one edge of the electrode is accentuated with increasing Hall parameter. The phenomenon leads to short-circuiting of the current between neighboring electrodes, and increases the internal resistance of the MHD generator, thus resulting in generator performance deterioration.

In order to reduce this current concentration, the author here propose an arrangement of MHD generator in which segmented electrodes of resistive material are used, and the current is led out from the edge just opposite the edge where the current concentration usually occurs(refer to Fig.2.1). The analysis is limited to generators with a seperate electrical circuit for each pair of electrodes. Numerical analysis by difference method has been undertaken(see Appendix A). The electrode is treated as one dimensional, which is valid if the thickness of the electrodes is very small compared with their length. From the current distribution thus calculated, the internal resistance and the potential distribution along the wall of the MHD generator are discussed.

II.2. Theory

II.2.1. Assumptions

The following assumptions are adopted:

(1) The gas-dynamical parameters (pressure, temperature and gas velocity) are constant, $\overline{u}=(u,0,0)$. Also, the electrical conductivity σ is constant (thermal equilibrium between electrons and atoms is assumed).

(2) The channel cross section is constant along its axis (x direction).

(3) The applied magnetic field $\overline{B}$ is constant and uniform, $\overline{B}=(0,0,B)$.

(4) Channel end effects are excluded, thus providing a repetitive boundary condition in the x direction.

(5) Ion-slip is neglected.

(6) The thickness of the electrodes (y direction) is very small compared with their length (x direction), which assumption permits the electrodes to be treated as one dimensional.

(7) The upper (anode) and the lower (cathode) electrodes have the same constant resistivity ρ.

(8) Lead wires are connected to the edges just opposite the points where current usually concentrates.

(9) No leakage current flows between neighboring electrodes.

(10) Fig.2.1 shows the right-hand coordinate systems. The gas flows from left to right in the positive x direction and the magnetic field is applied in the positive z direction. Arrows indicate position of lead wires.

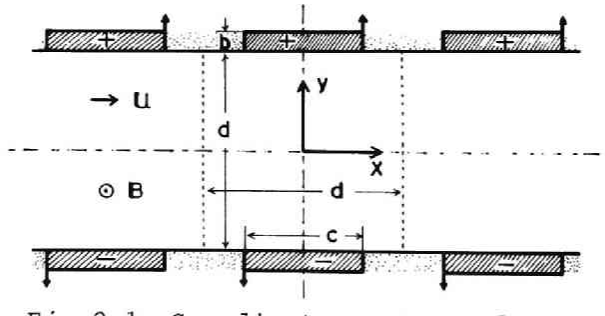

Fig.2.1. Coordinate system and configuration of MHD generator.

Arrows indicate positions of lead wires.

II.2.2. Basic equations

Ohm's law may be written in the form from Eqs.(1.1) and (1.2) as

$$\overline{j} = \overline{E}^* - \beta_e(\overline{j}\times\overline{B})/B, \tag{2.1}$$

$$\overline{E}^* = \overline{E} + \overline{u}\times\overline{B}. \tag{2.2}$$

On the basis of Maxwell's equations and the preceding assumptions, it can be shown that

$$rot\ \overline{E}^* = 0, \tag{2.3}$$

$$div\ \overline{j} = 0. \tag{2.4}$$

The current flux function ψ is defined by the relation

$$j_x = \partial\psi/\partial y, \tag{2.5}$$

$$j_y = -\partial\psi/\partial x. \tag{2.6}$$

Substitution of Eqs.(2.5) and (2.6) into Eq.(2.3) yields

$$\nabla^2\psi = 0, \qquad -d/2 \leqq x \leqq d/2, \quad -d/2 < y < d/2. \tag{2.7}$$

On the insulator surface,

$$j_y = 0, \qquad c/2 < |x| \leqq d/2, \quad y = \pm d/2, \tag{2.8}$$

which, with Eq.(2.6), results in

$$\psi = \psi_0, \qquad c/2 < x \leqq d/2, \quad y = \pm d/2, \tag{2.9}$$

$$\psi = 0, \qquad -d/2 \leqq x < -c/2, \quad y = \pm d/2, \tag{2.10}$$

where

$$\psi_0 = \int_{-d/2}^{d/2} -j_y dx. \tag{2.11}$$

On the resistive electrode surface(see Appendix A)

$$E_x^* = \rho/b \int_{-c/2}^{x} j_y dx, \qquad |x| \leqq c/2, \quad y = d/2, \tag{2.12}$$

$$E_x^* = \rho/b \int_{x}^{c/2} j_y dx, \qquad |x| \leqq c/2, \quad y = -d/2, \tag{2.13}$$

where ρ is the resistivity of the electrode, and b the electrode thickness. Introducing dimensionless quantities defined by

$$\psi' = \psi/\psi_0, \quad x' = x/d, \quad y' = y/d, \tag{2.14}$$

Eqs.(2.7),(2.9),(2.10),(2.12) and (2.13), with the previous assumption (4), become

$$\partial^2\psi'/\partial x'^2+\partial^2\psi'/\partial y'^2 = 0; \quad -1/2\leqq x'\leqq 1/2, \ -1/2<y'<1/2, \tag{2.15}$$

$$\psi' = 0; \quad -1/2\leqq x'<-c/2d, \ y'=\pm 1/2, \tag{2.16}$$

$$\psi' = 1; \quad c/2d<x'\leqq 1/2, \ y'=\pm 1/2, \tag{2.17}$$

$$\partial\psi'/\partial y'-\beta_e\partial\psi'/\partial x' = -\alpha\psi; \quad |x'|\leqq c/2d, \ y'=1/2, \tag{2.18}$$

$$\partial\psi'/\partial y'-\beta_e\partial\psi'/\partial x' = -\alpha(1-\psi'); \quad |x'|\leqq c/2d, \ y'=-1/2, \tag{2.19}$$

$$\psi'(x',y')+1 = \psi'(x'+1,y'); \tag{2.20}$$

where

$$\alpha = \sigma\rho d/b. \tag{2.21}$$

II.2.3. Internal resistance

The total current J is written in the form

$$J = w\int_{-c/2}^{c/2} -j_y(x,d/2)dx = w\psi_0, \tag{2.22}$$

where w is the electrode length in the z direction (channel width). The potential difference V between the right-hand edge of the positive electrode (anode) and the left-hand edge of the negative electrode (cathode) can be expressed by

$$V = 2\{\int_0^{d/2} -E_y^*(0,y)dy + \int_0^{c/2} -E_x^*(x,d/2)dx\} = (\psi_0/\sigma)\langle R_i\rangle, \tag{2.23}$$

where

$$\langle R_i \rangle = 2\{\int_0^{1/2} (\partial\psi'/\partial x')\big|_{x'=0} dy' + \alpha\int_0^{c/2d} \psi'(x',1/2)dx' + \beta_e[\psi'(0,1/2)-0.5]\}, \quad (2.24)$$

Then the internal resistance of the MHD generator is given by

$$R_i = V/J = \langle R_i \rangle/\sigma w = R_{ideal}\cdot\langle R_i \rangle, \quad (2.25)$$

where

$$R_{ideal} = 1/\sigma w. \quad (2.26)$$

R_{ideal} is considered to be the ideal resistance for the case $c/d=1$ (continuous electrode) and $\beta_e=0$ without end effects.

II.2.4. Potential distribution along the wall

The potential distribution along the upper electrode can be calculated from Eq.(A.3). The result is

$$\phi_{ue} = (\psi_o/\sigma)\phi'_{ue}, \quad (2.27)$$

where

$$\phi'_{ue} = \alpha\int_{-c/2d}^{x'} \psi'(x',1/2)dx' + \phi'_{ue}(-c/2d,1/2). \quad (2.28)$$

The potential distribution on the insulator downstream the electrode is expressed as

$$\phi_{ui} = (\psi_o/\sigma)\phi'_{ui}, \quad (2.29)$$

where

$$\phi'_{ui} = \int_{-1/2}^{x'} (\partial\psi'/\partial y')dx' - \beta_e\{\psi'(x',1/2)-\psi'(-1/2,1/2)\} + \phi'_{ui}(-1/2,1/2). \quad (2.30)$$

The potential distribution on the insulator upstream the electrode can be written in a similar form. The potential distribution ϕ_u' along the upper wall is represented in Fig.2.16, where $\phi_{ui}'(-1/2,1/2)$ is taken to be zero.

II.2.5. Hall potential

Making use of Eq.(2.1), the Hall potential difference between the points $(-d/2,0)$ and $(d/2,0)$ can be written as

$$V_H = \int_{-d/2}^{d/2} -E_x^* dx = (\psi_0/\sigma)V_H', \tag{2.31}$$

where

$$V_H' = -\int_{-1/2}^{1/2} (\partial\psi'/\partial y')dx' + \beta_e. \tag{2.32}$$

II.3. Results and discussions

Numerical analyses were made for various values of the three parameters, i.e., geometric parameter c/d, Hall parameter β_e, and dimensionless resistivity of the electrodes α.

The following ranges were used.

$$0.25 \leqq c/d \leqq 0.75, \quad 0 \leqq \beta_e \leqq 10, \quad 0 \leqq \alpha \leqq 50.$$

The current distributions are shown in Figs.2.2-2.9 for various values of β_e and α, and its dependence upon α is shown in Fig.2.10 for the case of $\beta_e=10$, $c/d=0.75$. It is clear from these figures that, for $c/d=0.25$, $\beta_e=1$, if α is chosen to be about 5, the current concentration on the edge of the electrode is greatly reduced and the distribution becomes nearly symmetric relative to the electrode center, which produces a condition analogous to that in case of $\beta_e=0$, $\alpha=0$. The similar tendency is also seen for the case of $\beta_e=5$, $\alpha=12.5$, $c/d=0.5$ and of $\beta_e=10$, $\alpha=20$, $c/d=0.75$.

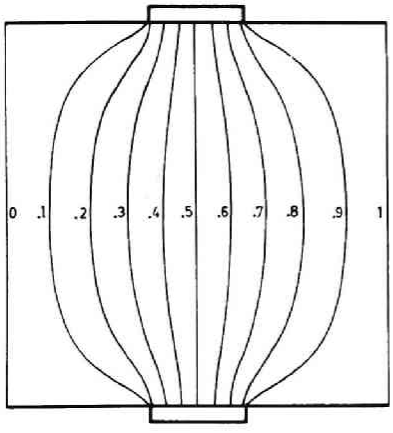

Fig.2.2. Current distribution for $\beta_e=0$, $\alpha=0$ and $c/d=0.25$.

The line $\psi'=0.5$ is identical with the electrode center.

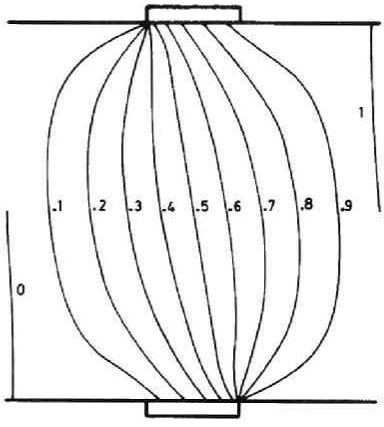

Fig.2.3. Current distribution for $\beta_e=1$, $\alpha=0$ and $c/d=0.25$.

Weak current concentration is seen.

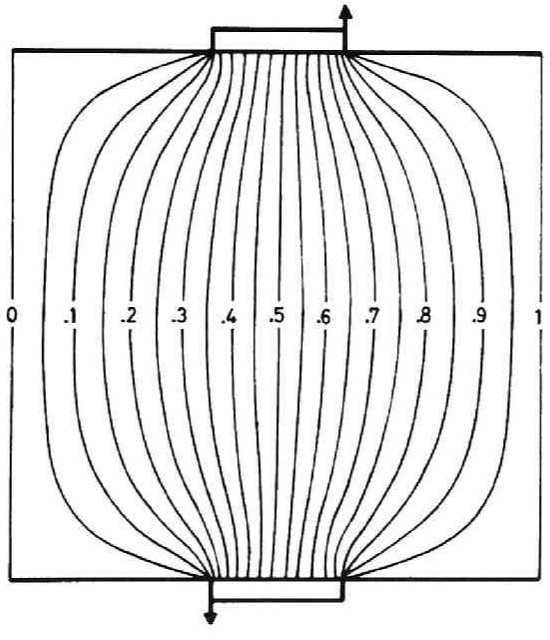

Fig.2.4. Current distribution for $\beta_e=1$, $\alpha=5$ and $c/d=0.25$.

Note that fairly symmetric current distribution relative to the electrode center is obtained compared with distribution of Fig.2.3.

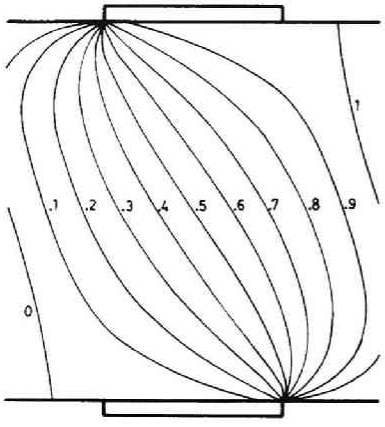

Fig.2.5. Current distribution for β_e=5, α=0 and c/d=0.5.

Considerable current concentration is seen.

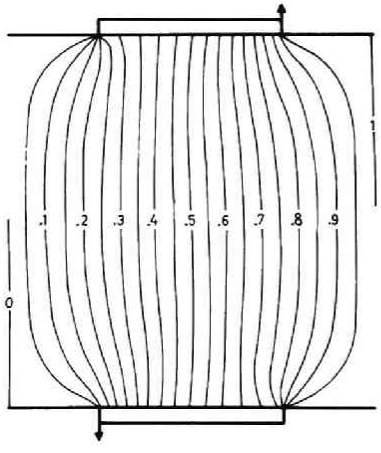

Fig.2.6. Current distribution for β_e=5, α=12.5 and c/d=0.5.

Note that fairly symmetric current distribution relative to the electrode center is obtained compared with distribution of Fig.2.5.

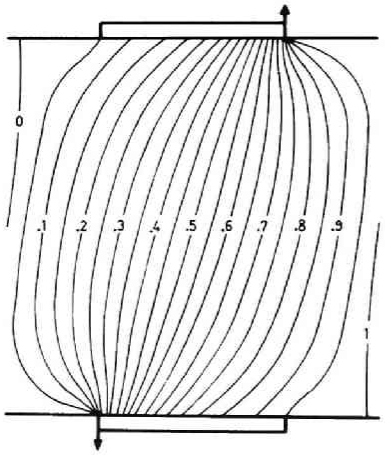

Fig.2.7. Current distribution for β_e=5, α=30 and c/d=0.5.

Current concentration at the edge where lead wire is connected begins to occur again.

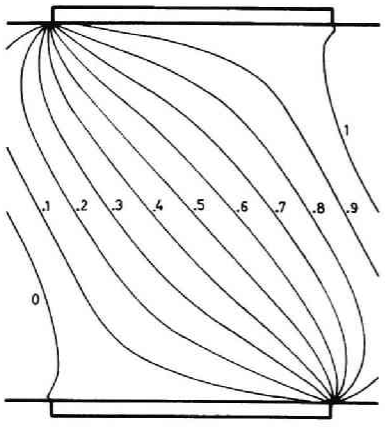

Fig.2.8. Current distribution for β_e=10, α=0 and c/d=0.75.

Strong current concentration is seen.

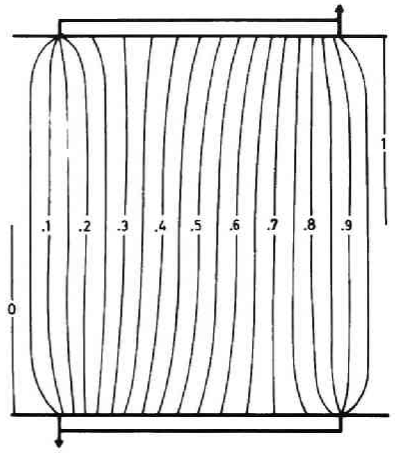

Fig.2.9. Current distribution for β_e=10, α=20 and c/d=0.75.

Note that fairly symmetric current distribution relative to the electrode center is obtained. Greatly reduced current concentration is seen compared with distribution of Fig.2.8.

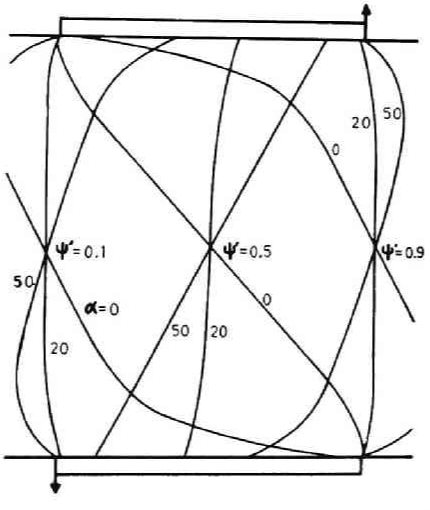

Fig.2.10. Dependence of current distribution upon α for β_e=10 and c/d=0.75.

With increasing α, the current begins to concentrate on the edge where lead wire is connected.

When α increases further, as in Figs.2.7 and 2.10, the current begins to concentrate at the other edge of the electrodes where the current is led out.

From the various current distributions calculated, the value of α that gives a current distribution closest to symmetry in reference to the electrode center is a function of β_e and c/d (since the pitch is chosen to be unity). This function can be approximated by

$$\alpha_s \simeq 4.5\beta_e; \qquad c/d=0.25, \tag{2.33}$$

$$\alpha_s \simeq 2.5\beta_e; \qquad c/d=0.5, \tag{2.34}$$

$$\alpha_s \simeq 2.0\beta_e; \qquad c/d=0.75. \tag{2.35}$$

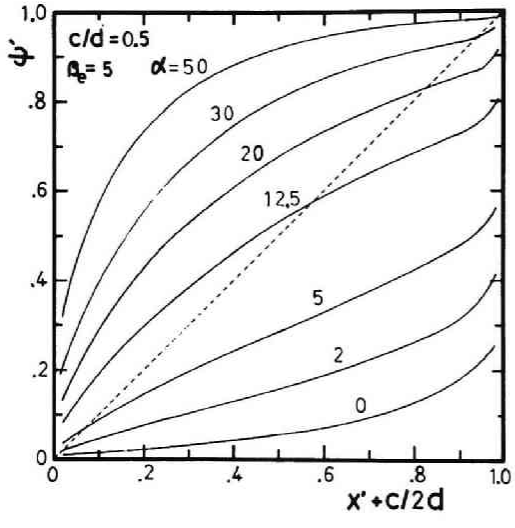

Fig.2.11. Distribution of current flux function ψ' on lower electrode for $\beta_e=5$ and $c/d=0.5$.

Fig.2.11 shows the distribution of the current flux function ψ' for the lower electrode in the case of $\beta_e=5$, $c/d=0.5$. Since the gradient of this curve gives the current density j_y, the current distribution nearest to the ideal current flux distribution (dotted straight line) is that which is sought for effectively reducing current concentration.

The dimensionless internal resistance $\langle R_i \rangle$ for each aspect ratio is shown in Figs.2.12-2.14. For $\beta_e=0$, while the current distribution is perfectly symmetric relative to the electrode center when $\alpha=0$, it progressively loses its symmetric form with increasing α and the current path becomes longer, resulting in increased internal resistance.

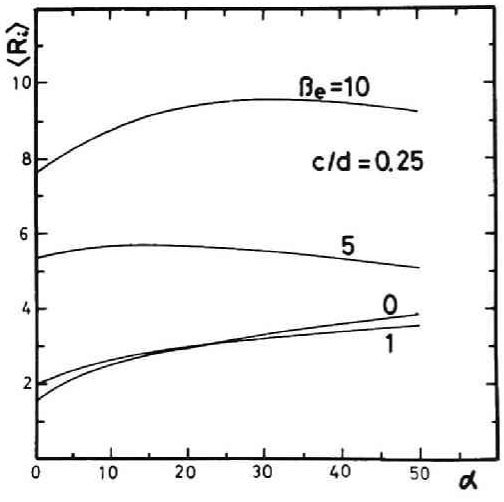

Fig.2.12. Dimensionless internal resistance for case of c/d=0.25.

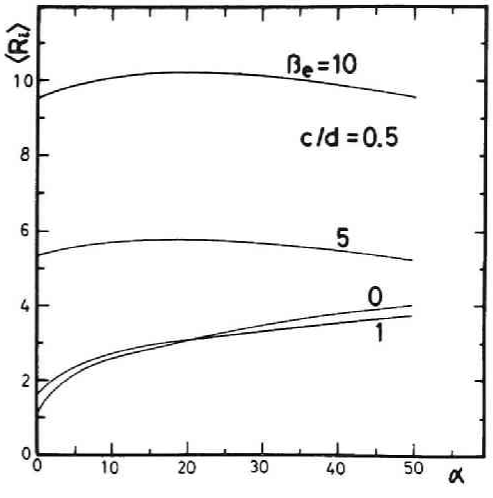

Fig.2.13. Dimensionless internal resistance for case of c/d=0.5.

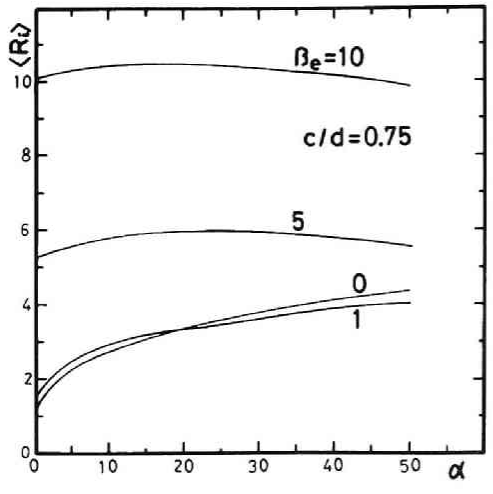

Fig.2.14. Dimensionless internal resistance for case of c/d=0.75.

For $\beta_e=1$, as is seen in Figs.2.12 -2.14, $\langle R_i \rangle$ increases with α. This is due to the reduction of the dependence of the internal resistance on the current homogeneity brought about by the resistive electrode since the degree of the current concentration is small compared with the case of larger Hall parameters, and the effect of the electrode resistance begins to make itself felt with increasing β_e. Therefore, in so far as the internal resistance is concerned, the resistive electrode system does not contribute

to the generator performance so effectively for small values of β_e. In the range of large values of β_e, however, the internal resistance becomes strongly dependent upon the current distribution, so that a moderately resistive electrode gives nearly the same value of $\langle R_i \rangle$ as in case of $\alpha=0$, and at the same time it can assure more symmetric current distribution. This fact is very favorable to improving MHD generator performance in nonequilibrium ionization, since a more uniform Joule heating and therefore a more uniform electron density can thereby be expected.

Fig.2.15 shows V_H' in case of $c/d=0.75$. The potential distribution ϕ_u' on the upper wall is also shown in Fig.2.16. It is clearly seen how, for $\alpha=0$, the potential gradient (i.e., electric field) at one edge of the electrode is so steep as to force the leakage current to flow along the wall, resulting in the short-circuiting effect. The potential difference between the two points $(-d/2,d/2)$ and $(d/2,d/2)$ is theoretically equal to the value V_H, and if $\alpha=0$ this value is maintained only by the insulators. But when α increases the value V_H is

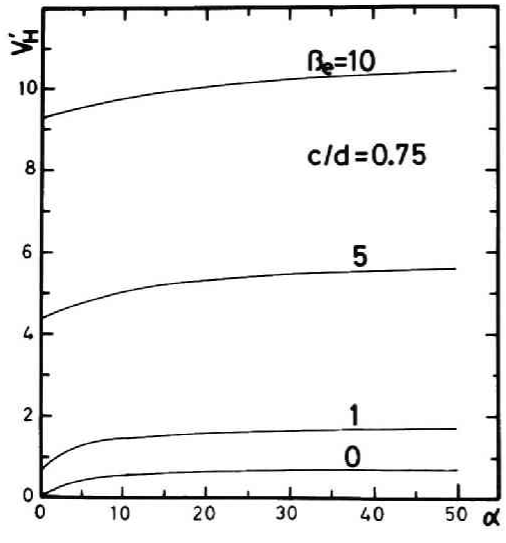

Fig.2.15. Dimensionless Hall potential between points (-d/2,0) and (d/2,0) for case of c/d=0.75.

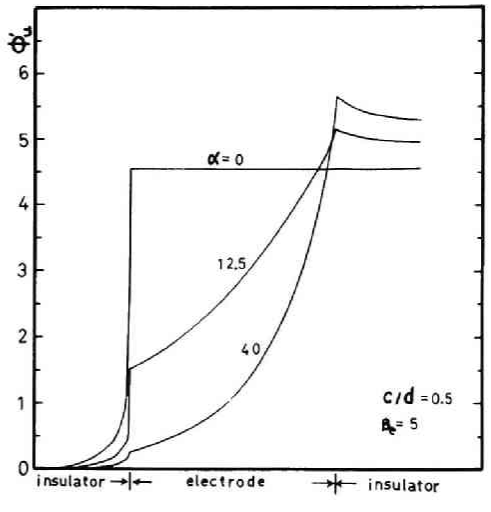

Fig.2.16. Potential distribution on upper wall for case of β_e=5 and c/d=0.5.

Steep potential gradient of α=0 is markedly reduced when α=40.

maintained by the combined action of both the electrode and insulators, which greatly reduces the steep potential gradient as illustrated in Fig.2.16 for cases of $\alpha=12.5$ and 40.

II.4. Concluding remarks

As foreseen, with moderately resistive electrode, the current distribution is brought appreciably closer to symmetry in reference to the electrode center, thus greatly reducing current concentration on one edge of the electrode. And furthermore, the gradient of electrical potential at the border between electrode and insulator is eased, thus preventing short-circuiting between neighboring electrodes. However, as a general rule, the internal resistance must inherently be larger with resistive electrodes than with non-resistive, and this disadvantage is accentuated when the Hall parameter is small.

The foregoing analysis has been based upon the thermal equilibrium condition, but the difference of current distribution between equilibrium and nonequilibrium conditions seems not so great[7,8] in the tendency, and therefore, even under the latter conditions a homogeneous current distribution can be expected by choosing a suitably resistive material, semi-conductor or some ceramics for example, for the electrodes. This will assure a homogeneous Joule heating and thereby a homogeneous electron density, and possibly in addition a smaller internal resistance than with non-resistive electrodes. In addition, the merit of resistive electrodes will lie in the fact that Joule heating of the electrode caused by the passage of the current will ensue the enhancement of the boundary layer temperature and also assist in thermionic emission from the electrode surface leading to the decrease in electrode drops.

While in the present work the lead wires have been connected to the extreme end of electrodes and the resistivity assumed to be the same between upper and lower electrodes, there may be many other practical arrangements for lead wire connections and selection of resis-

tivity. For example, if the lead wires were connected to the points $(c/4,d/2)$ and $(-c/4,-d/2)$, slightly removed from the electrode edge, the current concentration would then be much further reduced. (see Figs.2.17-2.19). Analyses covering cases of nonequilibrium conditions will provide more realistic and practical information on actual MHD generator performance.

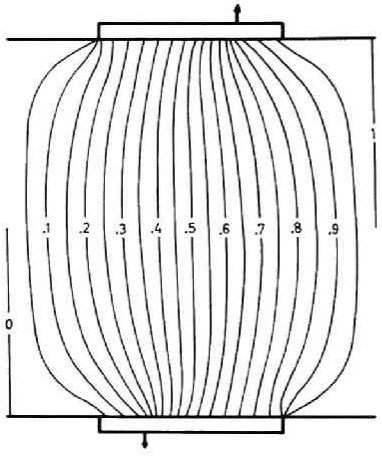

Fig.2.17. Current distribution for $\beta_e=1$, $\alpha=5$ and $c/d=0.5$.

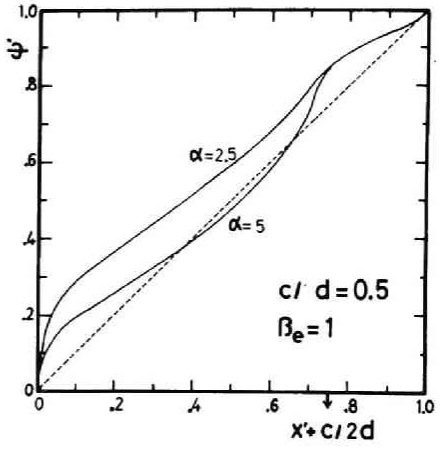

Fig.2.18. Distribution of current flux function ψ' on upper electrode for $\beta_e=1$ and $c/d=0.5$.

The dotted straight line indicates ψ' for a strictly uniform current. Arrows indicate positions of lead wires.

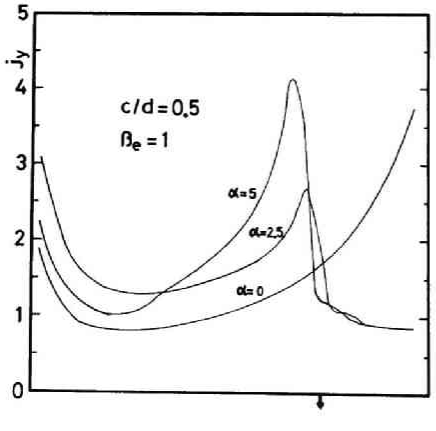

Fig.2.19. Current density j_y on upper electrode for $\beta_e=1$ and $c/d=0.5$.

The peaking of j_y in the vicinity of the lead wire indicated by an arrow is accentuated with increasing α.

III. CURRENT REFRACTION DUE TO DISCONTINUOUS HALL PARAMETER

III.1. Introduction

As was stated in chapter II, the current concentration at the electrode edge immediately causes complications such as short-circuiting between neighboring electrodes or nonuniform Joule heating, which consequently results in a seriously ineffective MHD generation in the nonequilibrium state. The proposal of using resistive electrodes was successfully analized in chapter II to realize a very uniform current distribution. The demerit of the electrode resistivity will be well canceled by the uniform current density and the shortening of the current path. In this chapter, another method to control the current distribution is proposed, that is, to control the current pattern by using spatially nonuniform Hall parameters.

We begin by assuming that only the electrical conductivity σ and the Hall parameter β_e are variables, whereas other quantities such as flow velocity $\overline{u}$ or the applied magnetic field $\overline{B}$ are constant in order to simplify the problem.

III.2. Theory

The configuration of an MHD generator is shown in Fig.3.1 and $\overline{u}$, $\overline{B}$ are expressed as

$$\overline{u} = (u,0,0), \quad u=const., \qquad (3.1)$$

$$\overline{B} = (0,0,B), \quad B=const. \qquad (3.2)$$

From Eq.(1.1) neglecting the ion-slip effect and electron pressure gradient, it is reduced to a

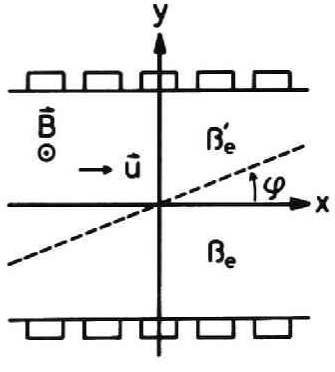

Fig.3.1. Configuration of MHD generator.

Dotted line denotes surface of discontinuity of Hall parameters.

familiar form as

$$\overline{j} = \sigma(\overline{E}+\overline{u}\times\overline{B}) - \beta_e/B\cdot\overline{j}\times\overline{B}. \tag{3.3}$$

where

$$rot\ \overline{E}^* = rot\ \overline{E} + rot\ (\overline{u}\times\overline{B}) = 0, \tag{3.4}$$

$$div\ \overline{j} = 0. \tag{3.5}$$

Parameters such as σ or β_e are assumed to change from σ or β_e to σ' or β_e', respectively across the boundary (surface) of discontinuity (dotted straight line in Fig.3.1) which makes an angle φ with the x axis as seen in Fig.3.1. Denoting components parallel to or tangential to the surface of discontinuity by a subscript $/\!/$ or $\perp$, respectively, and from Eqs.(3.4) and (3.5), the following relations are obtained

$$j_\perp = j_\perp', \tag{3.6}$$

$$E_{/\!/}^* = E_{/\!/}^{*\prime}. \tag{3.7}$$

The tangential component of $\overline{j}$ and the parallel component of $\overline{E}^*$ are written as

$$j_\perp = j_x sin\varphi - j_y cos\varphi, \tag{3.8}$$

$$E_{/\!/}^* = E_x^* cos\varphi + E_y^* sin\varphi. \tag{3.9}$$

We denote angles of θ and θ' as

$$tan\theta = j_y/j_x, \tag{3.10}$$

$$tan\theta' = j_y'/j_x'. \tag{3.11}$$

Use of Eqs.(3.3) and (3.6)-(3.11) then yields

$$A_M\cdot\overline{\mathcal{E}}^* = 0, \tag{3.12}$$

where

$$A_M = \begin{pmatrix} \beta_e - \tan\theta, & 1+\beta_e\tan\theta, & 0, & 0 \\ 0, & 0, & \beta_e' - \tan\theta', & 1+\beta_e'\tan\theta' \\ 1, & \tan\varphi, & -1 & -\tan\varphi \\ \dfrac{\sigma(\tan\varphi-\beta_e)}{1+\beta_e^2}, & -\dfrac{\sigma(1+\beta_e\tan\varphi)}{1+\beta_e^2}, & -\dfrac{\sigma'(\tan\varphi-\beta_e')}{1+\beta_e'^2}, & \dfrac{\sigma'(1+\beta_e'\tan\varphi)}{1+\beta_e'^2} \end{pmatrix}, \quad (3.13)$$

$$\bar{\mathcal{E}}^* = \begin{pmatrix} E_x^* \\ E_y^* \\ E_x^{*\prime} \\ E_y^{*\prime} \end{pmatrix} . \quad (3.14)$$

For the existence of the non-trivial solution of $\bar{\mathcal{E}}^*$, the following equation must hold

$$\det A_M = 0. \quad (3.15)$$

Eq.(3.15) is simply reduced to

$$\frac{\beta_e + \cot(\theta-\varphi)}{\sigma} = \frac{\beta_e' + \cot(\theta'-\varphi)}{\sigma'} . \quad (3.16)$$

In order to generalize discussions, we introduce a new angle Θ as

$$\Theta = \pi/2 - (\theta-\varphi), \quad (3.17)$$

which denotes the angle of incidence (or refraction) of the current density vector with respect to the line normal to the discontinuity boundary line and Θ is measured from the incident or refracted current density vector to the normal line(see Fig.3.2, where μ_e is an electron mobility).

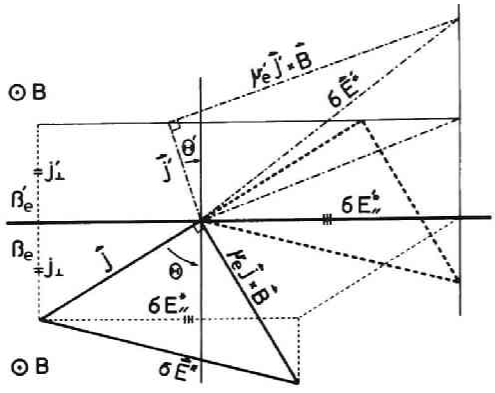

Use of Eq.(3.17) with Eq. (3.16) then yields

$$\frac{\beta_e+\tan\Theta}{\sigma} = \frac{\beta_e'+\tan\Theta'}{\sigma'} . \qquad (3.18)$$

Fig.3.2. Schematic Ohm's law and angle Θ.

μ_e is an electron mobility.

III.3. Results and discussions

In the calculations the electrical conductivity was assumed to be constant for convenience. From Eq.(3.18) the following relations hold

$$\tan\Theta' = \tan\Theta - \Delta\beta_e, \qquad (3.19)$$

$$\tan\Delta\Theta = -\Delta\beta_e/(\tan^2\Theta - \Delta\beta_e\tan\Theta + 1), \qquad (3.20)$$

$$\Delta\Theta_{max}| = \arctan\{4\Delta\beta_e/(\Delta\beta_e^2-4)\}, \qquad (3.21)$$
$$\tan\Theta^*=\Delta\beta_e/2$$

where

$$\Delta\beta_e = \beta_e' - \beta_e, \qquad (3.22)$$

$$\Delta\Theta = \Theta' - \Theta. \qquad (3.23)$$

Θ' vs. Θ for positive $\Delta\beta_e$ is shown in Fig.3.3. It is seen that when $\Delta\beta_e$ is positive, the incident current is always refracted to the left and the refracted angle changes greatly at large incident angles. It should be noted that the relationship between Θ and Θ' for negative

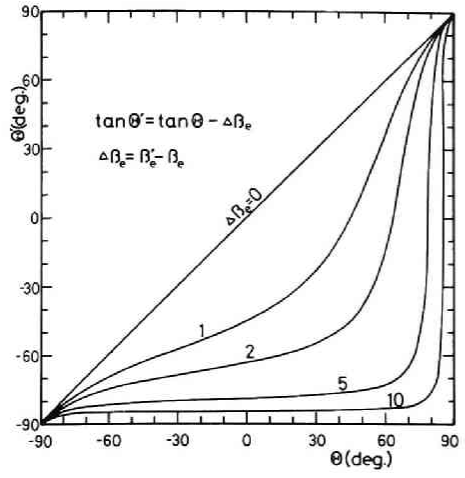

Fig.3.3. Refracted angle vs. incident angle of the current density for positive $\Delta\beta_e$.

$\Delta\beta_e$ will be easily obtained by exchangeing angles Θ and Θ' with each other. Fig.3.4 shows the relationship between $\Delta\Theta$ and Θ in Eq.(3.20). The figure shows that the large angle of deviation is obtained at large incident angles and its minimum lies on the straight line ($\Delta\Theta=-2\Theta^*$) and is realized at $\Theta=\Theta^*$, where Θ^* is $arctan(\Delta\beta_e/2)$.

In Fig.3.5 $\Delta\Theta_{min}$ is shown with respect to $\Delta\beta_e$. With increasing $\Delta\beta_e$, $\Delta\Theta_{min}$ begins to saturate and approaches *-180 deg*. In the region below $\Delta\beta_e \simeq 5$, $\Delta\Theta_{min}$ decreases greatly, but gradually in the region above $\Delta\beta_e \simeq 5$.

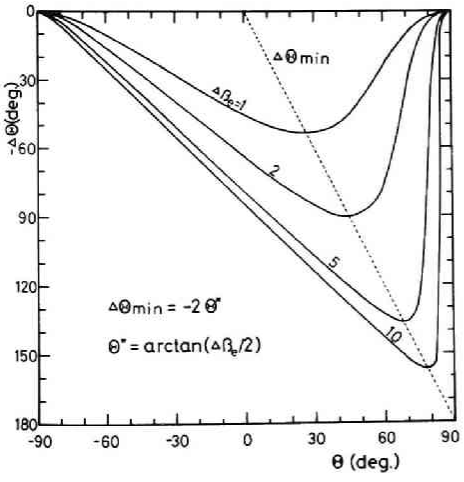

Fig.3.4. Angle of deviation vs. incident angle of the current density for positive $\Delta\beta_e$.

Dotted line shows $\Delta\Theta_{min}$.

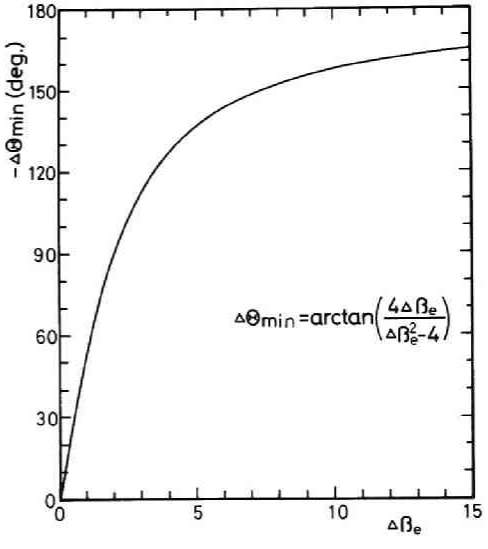

Fig.3.5. The minimum angle of deviation $\Delta\Theta_{min}$ *vs.* $\Delta\beta_e$.

The results of above calculations, consequently, proved the feasibility of current pattern control by arranging Hall parameters.

III.4. Concluding remarks

The feasibility to control the current distribution by using spatially nonuniform Hall parameters was successfully proved. With respect to the method realizing a desirable distribution of the Hall parameters, the application of the spatially modulated magnetic field will be most convenient, since the Hall parameter is proportional to the magnetic field strength. The analysis, however, must be made in the three dimension when the spatially modulated magnetic field is applied. This is because the external magnetic field $\overline{B}_a$ must always satisfy the equation for small magnetic Reynold's numbers

$$rot\ \overline{B}_a = 0. \qquad (3.24)$$

Hence the external magnetic field such as $\overline{B}_a = B_z(x,y)\overline{e}_z$ [12,13] can't be realized in practice and it should be noted that such $\overline{B}_a$ is always associated with other components B_x and B_y, resulting in the three-dimensional current distribution in general.

The detail analysis of the current control by using the spatially modulated magnetic field is beyond our scope and is left to future study.

IV. IONIZATION INSTABILITY AND STABLE REGION IN POTASSIUM SEEDED ARGON GAS PLASMA MHD GENERATION

IV.1. Introduction

It has been pointed out by many authors[16,35,42] that there are obstacles against the realization of an effective nonequilibrium ionization in a closed cycle plasma MHD generation and one of the main obstacles now being thought of will be the occurence of the ionization instability resulting in a large reduction of effective electrical conductivities and Hall parameters and thus in a serious deterioration of MHD generator performance. Recently, Nakamura et al.[32] proved experimentally that the plasma with fully ionized seed can be successfully used for the damping of the ionization instability and they showed that the effective electrical conductivity σ_{eff} at small seed fractions can be larger than that at high seed fractions under the condition of constant electric field strength and small magnetic field strength. However, since the current density in the stable region in case of such small seed fractions is severely restricted as will be shown later, the desired power density can hardly be obtained and remains generally at the low level. This restriction is of course very disadvantageous for practical MHD generation. And furthermore It is very important to know the influence of the operation pressure on the performance of the MHD generator, since, in the future, practical MHD generation will be made at considerably high pressures with HTGR.

In this chapter, stable regions free from the ionization instability are studied as functions of electron temperatures, magnetic field strengths, seed fractions and current densities under the condition of a gas temperature of *2000* ^{o}K and furthermore the influence

of magnetic field strength and operation pressure on the performance of a Faraday-type MHD generator with finely segmented electrodes are investigated.

IV.2. Equations

The plasma is assumed to be spatially uniform at an initial state and a perturbation of the plasma Y', such as electron temperature and number density, is assumed to occur in a plane wave whose propagation direction makes an angle θ with the averaged current density $\bar{j}$ (see Fig.B.5).

The perturbation form is assumed to be

$$Y' \propto exp(i\omega t), \tag{4.1}$$

where ω is a complex angular velocity defined as

$$\omega = \omega_r - i\omega_i. \tag{4.2}$$

Consequently, the maximum growth rate ω_i at the angle θ is given in a well known form from the linear perturbation theory[16,32] where instantaneous Saha equilibrium is assumed and terms except the elastic collision loss term are neglected in the electron energy equation. In the calculation of the collision frequency of electrons, Coulomb collision was also taken into account, and Ovcharenko's expression for the cross section of electrons with argon atoms was used[17].

Results by the linear perturbation theory are summarized below (see Appendix B).

$$\omega_i = \{\sqrt{(\beta_e n_T)^2+\sigma_T^2} - \sqrt{(\beta_{cr} n_T)^2+\sigma_T^2}\}/\tau^*, \tag{4.3}$$

$$\theta = arctan\{(1+\sqrt{1+\gamma_e^2})/\gamma_e\}, \tag{4.4}$$

$$\tau^* = n_e\{3kT_e/2+n_T(3kT_e/2+e<V_i>)\}/(j/\sigma)^2, \tag{4.5}$$

$$\beta_e = eB/(m_e\textstyle\sum_j \nu_{ej}), \tag{4.6}$$

$$\sigma = n_e e^2/(m_e\textstyle\sum_j \nu_{ej}), \tag{4.7}$$

$$n_T = d(\ln n_e)/d(\ln T_e), \tag{4.8}$$

$$\sigma_T = d(\ln \sigma)/d(\ln T_e), \tag{4.9}$$

$$A_T = d(\ln A)/d(\ln T_e), \tag{4.10}$$

$$\beta_{cr} = \sqrt{A_T^2-\sigma_T^2}\ /n_T, \tag{4.11}$$

$$\gamma_e = \beta_e n_T/\sigma_T, \tag{4.12}$$

$$A = (3/2)kn_e(T_e-T_g)\sum_j (m_e/m_j)\nu_{ej}\delta_j, \tag{4.13}$$

$$e\langle V_i\rangle = \sum_j n_j^+ V_{ij}/\sum_j n_j^+, \tag{4.14}$$

$$j = \sqrt{\sigma A}\ , \tag{4.15}$$

where β_{cr}, n_j, n_j^+ and A are critical Hall parameter, number density of the j-th component, ion number density of the j-th component and elastic collision loss of electrons, respectively, and m_j, δ_j, ν_{ej}, $\langle eV_i\rangle$ and eV_{ij} being mass of the j-th component, collision loss parameter of electrons with the j-th component, collision frquency of electrons with the j-th component, averaged ionization energy and ionization energy of the j-th component, respectively.

Considering ionization of all components, n_T is given by

$$n_T = \sum_j \alpha_j n_j(1-\alpha_j)(3/2+eV_{ij}/kT_e)/\sum_j \alpha_j n_j(2-\alpha_j), \tag{4.16}$$

where α_j is the ionization degree defined by the ratio of the j-th ion number density to its initial neutral number density.

Performance of a Faraday-type MHD generator with well finely segmented electrodes, each connected to a load resistance R_L, can be obtained from the following simultaneous equations(see Fig.4.1).

Current density;

$$j = \sigma_{eff} uB/(1+\sigma_{eff}/\sigma_L), \quad \text{(Ohm's law)}, \tag{4.17}$$

$$j = \sqrt{\sigma_{eff} A}\ , \quad \text{(energy equation)}, \tag{4.18}$$

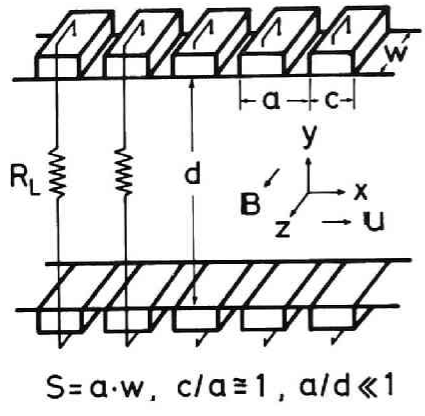

Fig.4.1. Configuration of a Faraday-type MHD generator with finely segmented electrode.

Power density;

$$P_e = (jS)^2 R_L/Sd = j^2/\sigma_L, \qquad (4.19)$$

where the effective electrical conductivity is assumed to be[32,40]

$$\sigma_{eff} = \sigma, \quad (\beta_e \leq \alpha_c \beta_{cr}), \qquad (4.20)$$

$$\frac{\alpha_c \beta_{cr}}{\beta_e}\sigma, \quad (\beta_e \geq \alpha_c \beta_{cr}), \qquad (4.21)$$

here α_c is a constant and the load resistance is expressed by σ_L as

$$\sigma_L = d/(SR_L). \qquad (4.22)$$

IV.3. Results of calculations

Calculations were performed for argon-potassium plasma under the condition of a gas temperature of *2000 °K*. The electron number density n_e and the electrical conductivity σ vs. the electron temperature T_e with allowance for the argon ionization is shown in Fig.4.2. It is obviously seen from the figure that the nearly perfect ionization of potassium atoms is realized and the electron number density saturates in the region near the intersecting point with the dotted line which corresponds to the maximum critical Hall parameter $(\beta_{cr})_{max}$, and then with increasing the electron temperature, argon plays an important role in the ionization and the electron number density sharply increases again. As for the electrical conductivity, it also increases at first with increasing the electron temperature until the region of full ionization of potassium atoms and begins to decrease in spite of the temperature rise due to invariable electron number density and the increase of collision frequency of electrons in case of relatively smaller seed fractions. When the electron temperature further increases, the electrical conductivity begins to increase again by the

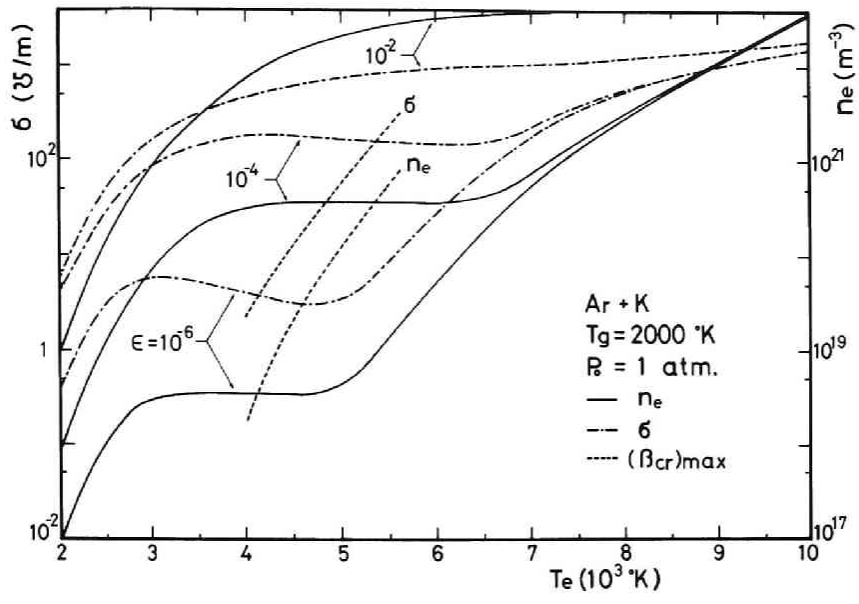

Fig.4.2. Electrical conductivity and electron number density vs. electron temperature.

onset of argon ionization.

In Fig.4.3 the current density j vs. the electron temperature T_e is shown for various seed fractions. Since the current density is proportional to n_e, the plateau seen in Fig.4.2 also exists in Fig.4.3 due to small n_T.

Critical Hall parameters β_{cr} and electrical conductivities σ vs. current densities are shown in Fig.4.4. The ionization of argon atoms being allowed, the maximum critical Hall parameter does not take an infinite value and remains finite[32]. According to the results obtained, the maximum Hall parameter is realized at the minimum value of n_T. It is generally true that the smaller is a seed fraction, the larger is a maximum critical Hall parameter and also the smaller is the corresponding current density. The peculiar tendency seen for a seed fraction of $\varepsilon=10^{-2}$ near $j=10^3 A/cm^2$ is attributed to the fact that the growth rate ω_i can not essentially be negative under these conditions. The reason why the electrical conductivity decreases after reaching the maximum value is same as that mentioned in Fig.4.2.

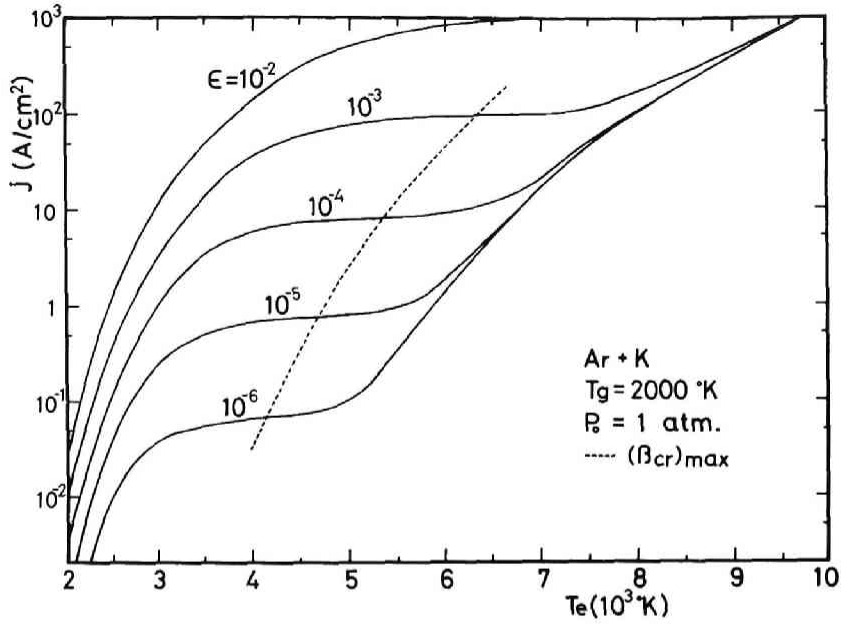

Fig.4.3. Current density vs. electron temperature.

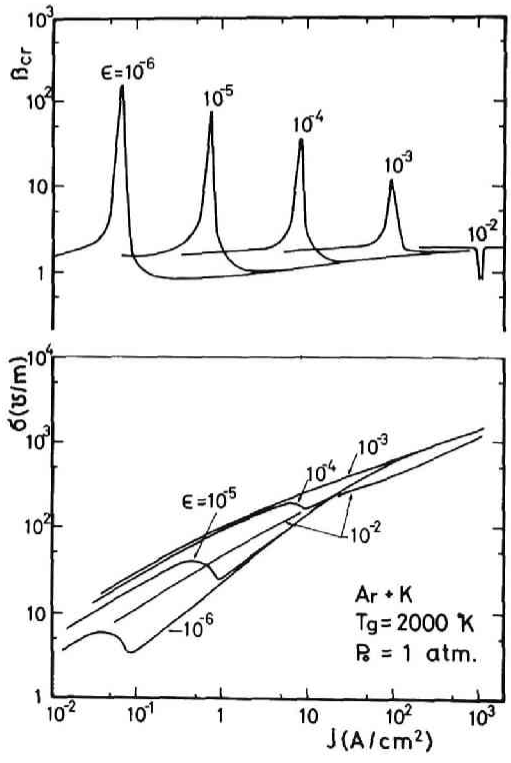

Fig.4.4. Critical Hall parameter and electrical conductivity vs. current density.

It should be noted that the critical Hall parameter $\beta_{cr} \simeq 2$ experimentally obtained[34,35] in the current region of $j=1\text{-}10\ A/cm^2$ for $\varepsilon=2\times10^{-3}$ agree well with that for $\varepsilon=10^{-3}$ in Fig.4.4.

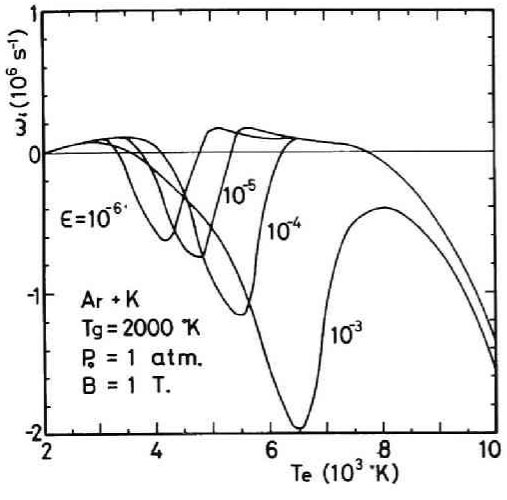

Fig.4.5. Growth rate vs. electron temperature.

The growth rate ω_i vs. the electron temperature T_e at $B=1$ *Tesla* is shown in Fig.4.5 for various seed fractions. The growth rate is requested only to be negative for the condition of stability, but the absolute value of ω_i will be desired to be as large as possible for the rapid decay of the perturbation. Under the present conditions, ω_i is of the order of $10^6\ s^{-1}$ and hence the system may be regarded to be completely stable only if ω_i is negative.

Hall parameters β_e and critical Hall parameters β_{cr} vs. the electron temperature T_e are shown in Figs.4.6 and 4.7 for $\varepsilon=10^{-3}$ and 10^{-5}, respectively. It is needless to say that the system is inherently stable at $T_e=T_g$ independent of the magnetic field strength. In Fig. 4.6 for $\varepsilon=10^{-3}$, the system is stable at $B=0.1$ *Tesla* for any electron temperatures below 10^4 °K. However, with increasing the magnetic field above $B_c=11.27$ *Tesla*, the system can not be stable any more in the electron temperature range below 10^4 °K. This can also be seen in Fig.4.7 for $\varepsilon=10^{-5}$ at the magnetic field strength above $B_c=15.28$ *Tesla*, where B_c is the critical magnetic field strength at which the system changes from stable condition to unstable one. Alternation of the system between stable and unstable states is seen, in general, with increasing electron temperature at the specific magnetic field strength.

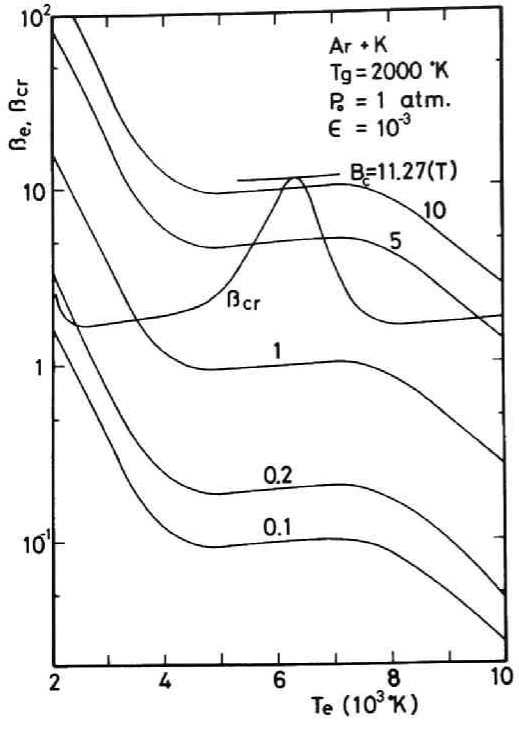

Fig.4.6. Hall parameter and critical Hall parameter vs. electron temperature for $\varepsilon=10^{-3}$.

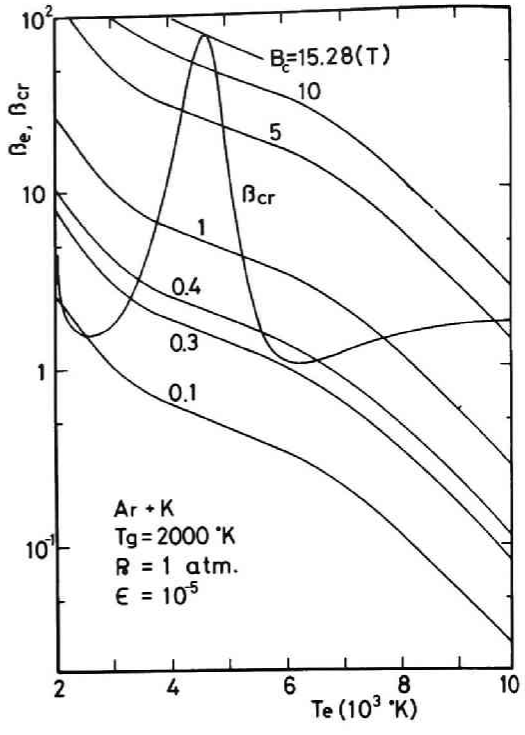

Fig.4.7. Hall parameter and critical Hall parameter vs. electron temperature for $\varepsilon=10^{-5}$.

In Fig.4.8 critical magnetic field strength B_c vs. current densities for various pressures in case of $\varepsilon=10^{-5}$ is shown. It is seen generally that B_c becomes large when the pressure is large except in the neighborhood of its maximum and also the current density corresponding to the maximum B_c shifts to the larger region. As far as the operation mode is concerned, the figures show that the MHD generation in the stable mode at a moderately high magnetic field, say about *5 Tesla*, and also at a desired current density may be realized by arranging the operation pressure.

Stable regions as functions of the magnetic field and the current density for various seed fractions at atmospheric pressure are shown in Fig.4.9. The region above and below the curve are unstable and stable, respectively. At a fixed magnetic field the range of the current density in which the system is stable is wider, for larger

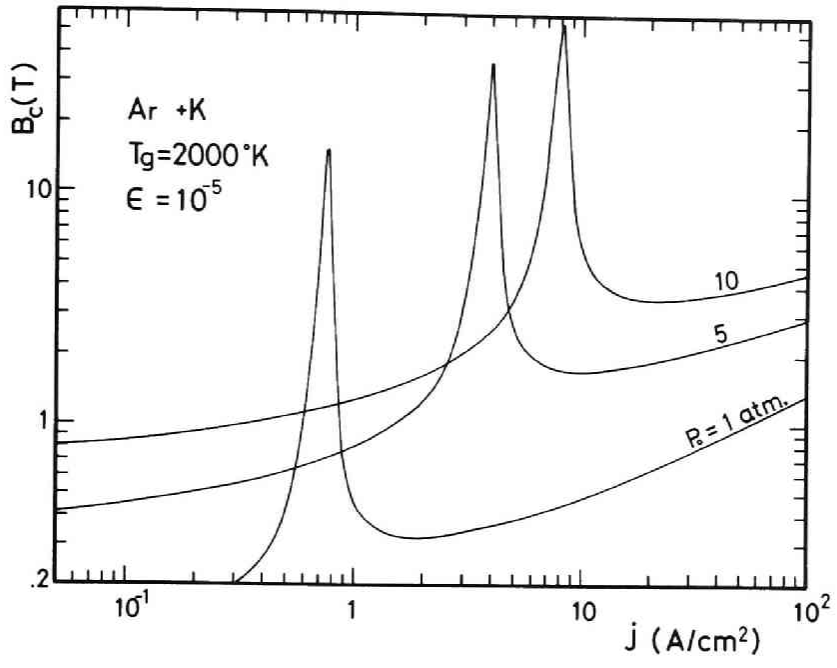

Fig.4.8. Critical magnetic field strength vs. current density for various pressures in case of $\varepsilon=10^{-5}$.

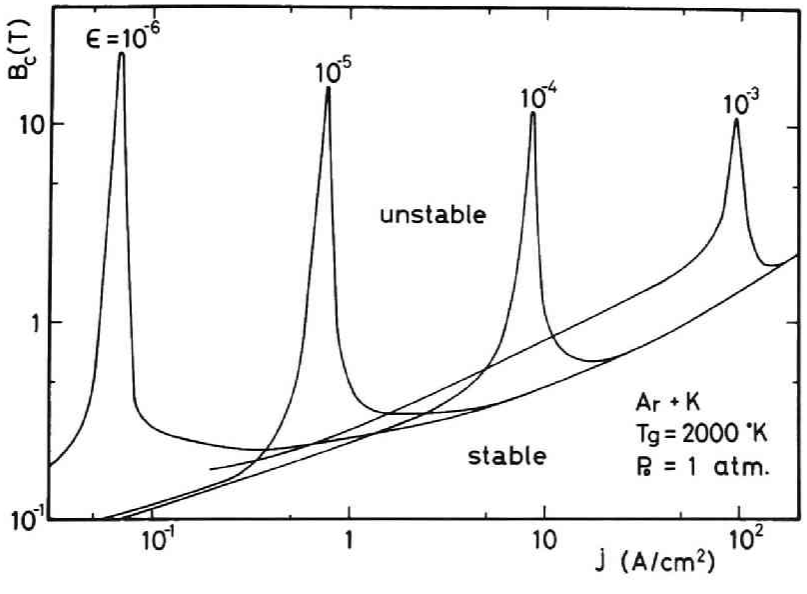

Fig.4.9. Stable regions as functions of magnetic field strength and current density at atmospheric pressure.

seed fraction. At a fixed current density, on the other hand, in the region above $B=5$ *Tesla*, the range of the seed fraction making the system stable is so narrowly restricted that the operation in the stable region does not seem to be very easy.

In Fig.4.10 the dependence of the stable region on the current density and the seed fraction is shown. The region between upper and lower curves is stable and current densities of $1\text{-}10^2 A/cm^2$ correspond approximately to seed fractions of $10^{-5}\text{-}10^{-3}$. It is to be noted that the linear part of the stable region still remains even if the magnetic field strength increases.

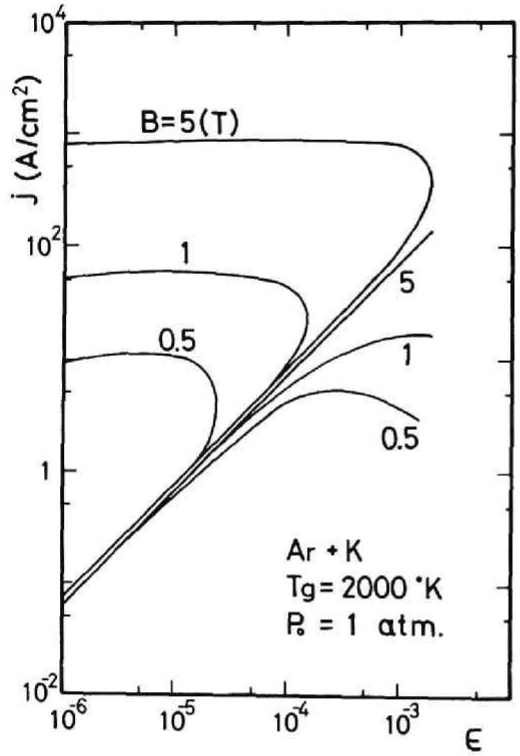

Fig.4.10. Stable regions as functions of current density and seed fraction at atmospheric pressure.

The electrical characteristics of a Faraday-type MHD generator with infinitely segmented electrodes each connected to an individual load resistance R_L as shown in Fig.4.1 were calculated for the argon-potassium plasma at a gas temperature of $2000\ ^\circ K$ assuming α_c in Eq.(4.21) to be unity. Under these conditions the electrical characteristics of the MHD generator were investigated in case of seed fractions of $\varepsilon=10^{-5}$ and 10^{-3} and flow velocities of $u=500$ and $1000\ m/s$.

According to the experimental results recently obtained by Brederlow et al.[40], the expression of the effective electrical conductivity given by Eq.(4.21) at $\alpha_c=1$ shows very good agreement with the experimental results for $A_r+0.05\%K$ at $T_g=1800\ ^\circ K$ in the range of

P_0=2.1-8.2 *bar* and B=1.1-3.55 *Tesla* ($\beta_e \leq 10.1$). However, they do not mention whether this equation will still rigorously hold good for various seed fractions and gas temperatures. If we assume that Eq.(4.21) exactly holds as long as the Hall parameter lies below *10*, then exact discussions for the case of $\varepsilon=10^{-5}$, σ_L=1 ℧/*m* and $\varepsilon=10^{-3}$, σ_L=10 ℧/*m* can not be made, as for these cases, β_e exceeds *10* at large magnetic fields (Fig.4.11-4.13). In Fig.4.16, however, the Hall parameter lies in the range far smaller than β_e=*10* although the seed fraction is twice and the gas temperature *200* °*K* higher than the condition executed by Brederlow et al.[40], and thus the equation may be allowed in this case for the estimation of the electrical performances of MHD generation. The expression for the effective electrical conductivity from Eq.(4.21) at α_e=*1* will be more exactly applicable to the actual case of high pressures, since the electron mobility decreases with increasing pressures. In the calculation of the electrical performances of MHD generators hereafter, Eq.(4.21) at α_e=*1* will be used as the most reliable expression now available for the effective electrical conductivity. It goes without saying that the final conclusion may be a little bit altered if the other relations which have been proposed[19,43] are used in place of Eq.(4.21), but the major conclusion obtained in this calculation seems to be still exact even for those relations.

The effective electrical conductivity σ_{eff} vs. the magnetic field strength B at atmospheric pressure is shown in Fig.4.11. In case of $\varepsilon=10^{-5}$ the current density corresponding to the maximum critical Hall parameter is easily realized, hence the largest effective electrical conductivity is realized in the stable region, and with increasing magnetic field σ_{eff} decreases slowly in the stable region and sharply in the unstable region. This tendency is seen also for any σ_L, and the maximum effective electrical conductivities for each σ_L are thus approximately same as about σ_{eff}=40 ℧/*m*. On the other hand for $\varepsilon=10^{-3}$, since the electron mobility is small compared with that for $\varepsilon=10^{-5}$, the stable region still exists for both large σ_L and velocity. In this region the increase of the magnetic field immediately

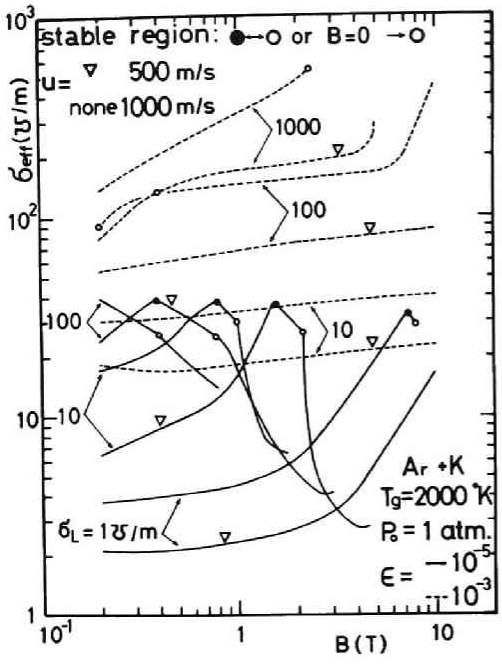

Fig.4.11. Effective electrical conductivity vs. magnetic field strength at atmospheric pressure in a Faraday-type MHD generator with finely segmented electrodes.

causes the increase of the current density resulting in the electron temperature rise, hence effective electrical conductivities increase. The obvious difference between $\varepsilon=10^{-5}$ and 10^{-3} is that σ_{eff} in the latter increases monotonously regardless of the system. When σ_L and the magnetic field strength are suitably fixed, there may be such a case[32] that the effective electrical conductivity in case of $\varepsilon=10^{-5}$ is larger than that in case of $\varepsilon=10^{-3}$, but in general, they are larger in case of $\varepsilon=10^{-3}$ than those in case of $\varepsilon=10^{-5}$ despite the partial ionization and being subject to the ionization instability in the former. It may be noted that the electron temperature rise for large σ_L is very rapid even in the region of small magnetic field strengths due to large Joule heating.

The current density vs. the magnetic field strength is shown in Fig.4.12. In case of $\varepsilon=10^{-5}$ the maximum current density corresponds to the smallest effective electrical conductivity in the stable region, and in the unstable region except the vicinity of the stable region, the current is roughly proportional to the magnetic field strength and this can be said also for the case of $\varepsilon=10^{-3}$. In general, current densities for $\varepsilon=10^{-3}$ seem larger than those for $\varepsilon=10^{-5}$ and this is true for the effective electrical conductivity also.

In Fig.4.13 the power density with respect to the magnetic field strength is shown. At small magnetic field strengths, power densities for $\varepsilon=10^{-5}$ are comparable to those for $\varepsilon=10^{-3}$, but in the region above

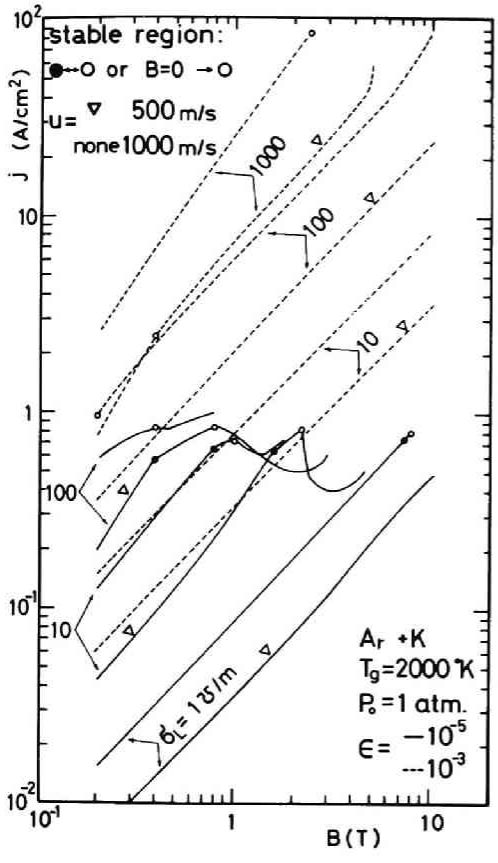

Fig.4.12. Current density vs. magnetic field strength at atmospheric pressure in a Faraday-type MHD generator with finely segmented electrodes.

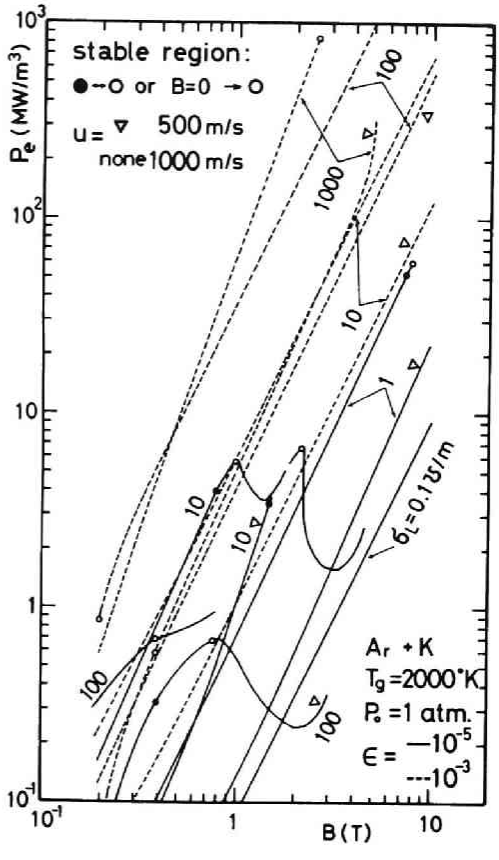

Fig.4.13. Power density vs. magnetic field strength at atmospheric pressure in a Faraday-type MHD generator with finely segmented electrodes.

B=1 Tesla those for $\varepsilon=10^{-3}$ are obviously far larger in general resulting in the superiority of the operation at a relatively high seed fraction, for example of 10^{-3}, provided the relation expressed by Eq.(4.21) exactly holds. It should be noted that the power density is still roughly proportional to the square of the magnetic field strength for $\varepsilon=10^{-3}$ in spite of being in the unstable region. It is desirable to compare maximum power densities for different seed fractions with each other, but the power density is a very complicated function of the load resistance, and its maximum is not attained generally at $\sigma_L=\sigma_{eff}$

in case of nonequilibrium MHD generation including the effects of the ionization instability.

As far as the actual MHD generation is concerned, it is of great interest to know the influence of the operation pressure and gas temperature on the MHD electrical performance.

In Fig.4.14 and 4.15 the effective electrical conductivity σ_{eff} vs. the magnetic field strength B is shown for various pressures at $T_g=2000\ ^oK$ for the case of $\varepsilon=10^{-3}$ and 10^{-5}, respectively. It is seen from Fig.4.14 that σ_{eff} does not remarkably depend on the operation pressure when the magnetic field strength increases and this tendency will be favorable to the practical MHD generation. In case of $\varepsilon=10^{-5}$ in Fig.4.15, σ_{eff} at higher pressures has the similar shape to that of $P_0=1\ atm.$ shifted to the larger magnetic field strength. Since the current density which gives $(\beta_{cr})_{max}$ may be easily realized below 10

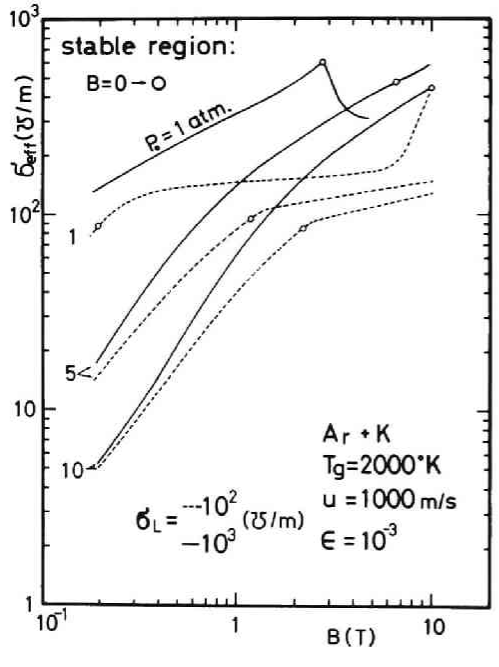

Fig.4.14. Effective electrical conductivity vs. magnetic field strength for $\varepsilon=10^{-3}$ in a Faraday-type MHD generator with finely segmented electrodes.

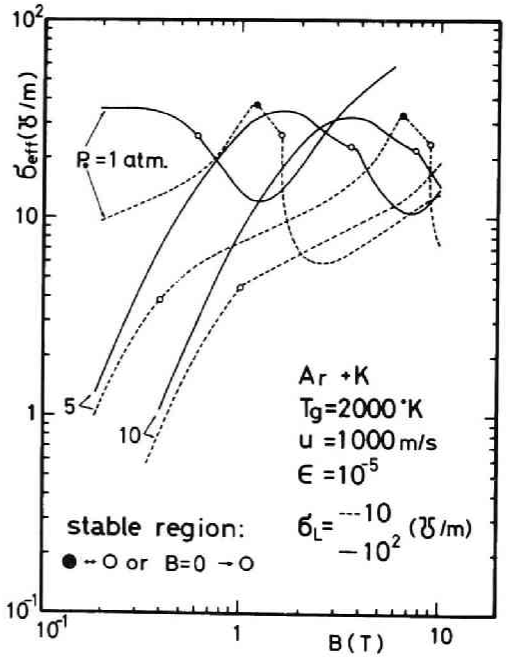

Fig.4.15. Effective electrical conductivity vs. magnetic field strength for $\varepsilon=10^{-5}$ in a Faraday-type MHD generator with finely segmented electrodes.

Tesla in the small seed fraction, σ_{eff} becomes a more complicated function of B and σ_L than that for $\varepsilon=10^{-3}$. The specific magnetic field strength giving $(\sigma_{eff})_{max}$ at high pressures exists also as shown in Fig.4.11, and this tendency differs apparently in that $(\sigma_{eff})_{max}$ for $\varepsilon=10^{-3}$ may be obtained at the largest B in general.

In Fig.4.16 power densities P_e vs. magnetic field strengths B for various pressures in case of $\varepsilon=10^{-3}$ are shown. It is obviously seen that the power densities scarecely depend on the operation pressure and they are still proportional to the magnetic field strength squared. And according to this figure, power densities more than $50\ MW/m^3$, which is the aiming power density at present for the practical MHD generation in the future, seem to be very easily obtained even at high pressures under the condition of $T_g=2000\ ^oK$ and $u=1000\ m/s$.

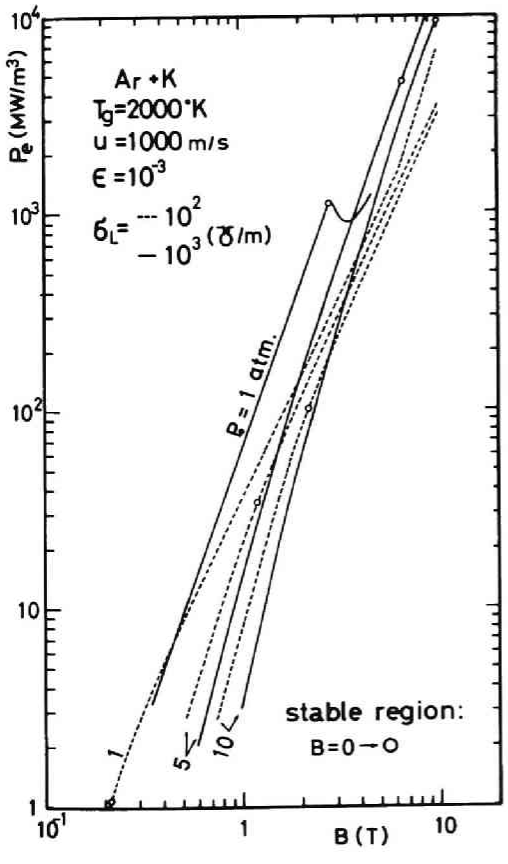

Fig.4.16. Power density vs. magnetic field strength for $\varepsilon=10^{-3}$ and $T_g=2000\ ^oK$ for various pressures.

In Figs.4.17 and 4.18 power densities P_e vs. magnetic field strengths B and $[P_e/(uB)^2]$ vs. B are shown at $T_g=1500\ ^oK$, respectively. Compared with that in Fig.4.16 at $T_g=2000\ ^oK$, P_e at $T_g=1500\ ^oK$ does not differ so much and shows similar tendency to that in Fig.4.16. It seems that even at a lower gas temperature of $1500\ ^oK$, power densities more than $50\ MW/m^3$ are still easily attainable at practical pressures. In Fig.4.18 $[P_e/(uB)^2]$ is shown for various seed fractions at a pressure of $20\ atm$. These figures show the superiority of operation at higher

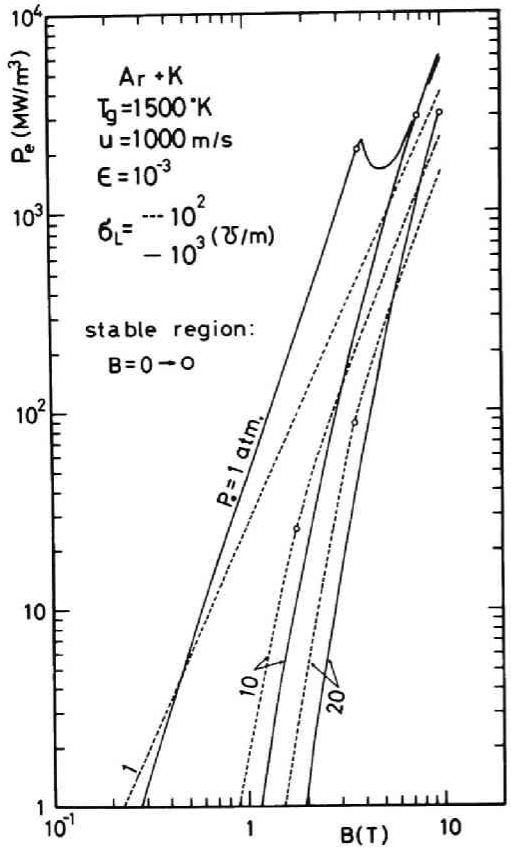

Fig.4.17. Power density vs. magnetic field strength for $\varepsilon=10^{-3}$ and T_g=1500 °K for various pressures.

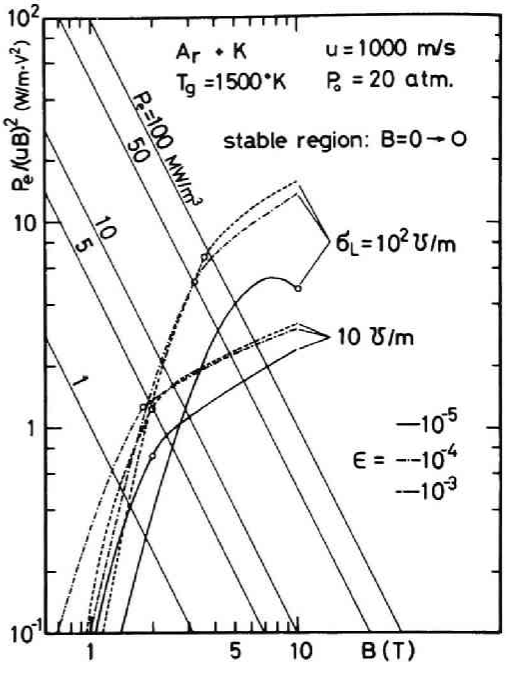

Fig.4.18. $[P_e/(uB)^2]$ vs. B at T_g=1500 °K and P_0=20 atm.

seed fractions and also afford the feasibility of the closed cycle MHD generation which will be connected at considerably high pressure levels with HTGR in the future.

IV.4. Concluding remarks

In a nonequilibrium MHD generation with potassium seeded argon plasma under the condition of T_g=2000 °K and atmospheric pressure, stable regions free from the ionization instability are so narrowly restricted by the seed fraction, the magnetic field strength and the current density, that a careful control of these quantities must be

made in order to operate MHD generation in the stable mode.

It is concluded that in a Faraday-type MHD generator with well finely segmented electrodes the results show the superiority of the operation at relatively high seed fractions, for example of 10^{-3}, over that at a seed fraction of 10^{-5}, in the region of high magnetic field strengths despite the partial ionization of the seed atoms and the occurrence of the ionization instability in the case of $\varepsilon=10^{-3}$.

Furthermore, it turned out that the influence of the operation pressure on the power density of a Faraday-type MHD generation is not pronounced and even at a low gas temperature of $1500\ ^{o}K$ and a pressure of $20\ atm.$, the power density for $\varepsilon=10^{-3}$ can still attain a value more than $50\ MW/m^{3}$ in the practical range of the magnetic field. These results consequently lead to the feasibility of the closed cycle gas plasma MHD generation operated at a relatively high seed fraction and a high pressure. Theoretical calculations including other energy loss effects of electrons are expected to be of the further study.

V. THE INFLUENCE OF SPATIAL TEMPERATURE DISTRIBUTION AND MEASURING CONFIGURATION ON LINE-REVERSAL TEMPERATURE[44]

V.1. Introduction

The potassium line-reversal method is widely used for plasma temperature measurements in MHD generators. It is a variant of the sodium line-reversal method[45,46,47]. Bundy and Strong[48] measured flame temperatures with this procedure. Recently, Riedmüller et al. [49] investigated the conditions which should be satisfied for a potassium line-reversal temperature to be almost identical with the electron temperature in the plasma and concluded that the typical MHD generator meets these conditions. According to their experiments, the potassium line-reversal temperature agreed well with the electron temperature derived from the measured electrical conductivity.

In this chapter, the effects of the temperature distribution in an MHD channel are studied, of the width of the inlet slit of the spectroscope and the spectral region covered by the photomultiplier on the potassium line-reversal temperature.

V.2. Line broadenings

In distinguishing the resonance line from others, we usually denote as; K, $4P_{1/2}$-$4S_{1/2}$, λ_0=7699 Å, where λ_0 is the wave length of the resonance line center. But in the strict meaning, the resonance line has not the definite energy corresponding to λ_0=7699 Å. This is partly due to the interaction with particles and partly due to the quantum effect. The physical coefficient describing these effects is called the absorption coefficient k_ν with frequency dependence corresponding to each effect.

V.2.1. Natural broadening

Natural broadening effect is caused essentially by the pure quantum effect, uncertainty principle, and the half-width for natural broadening $\Delta\nu_N$ is given by[50]

$$\Delta\nu_N = e^2\nu_0^2 f_{mn}/(\varepsilon_0 m_e c^3), \tag{5.1}$$

where ν_0, f_{mn} are the frequency of the resonance line center and the emission oscillator strength for $m \to n$ transition, respectively, and e, ε_0, c are elementary electric charge, dielectric constant of vacuum and speed of light, respectively. Thus a knowledge of f_{mn} allows immediate calculation of its natural broadened half-width $\Delta\lambda_N$ to be

$$\Delta\lambda_N = (\lambda_0^2/c)\Delta\nu_N \cong 1.15\times10^{-4}\text{Å}, \tag{5.2}$$

for K, λ_0=7699 Å. The overall shape of the absorption coefficient due to natural broadening is

$$k_{\nu N} = C_N/\left(1+\left(\frac{\nu-\nu_0}{\Delta\nu_N/2}\right)^2\right), \tag{5.3}$$

where C_N is a coefficient independent of the frequency ν.

V.2.2. Collision broadening

This broadening effect is ascribed to the field perturbation in the radiating atoms caused by the colliding atoms. The half-width for collision broadening $\Delta\nu_c$ is composed of the two half-widths $\Delta\nu_R$ (due to collision with radiating atoms themselves) and $\Delta\nu_P$ (due to collision with parent atoms). $\Delta\nu_R$ and $\Delta\nu_P$ are expressed with optical cross sections ρ_R^2, ρ_P^2, respectively, in the forms[52]

$$\Delta\nu_R = \rho_R^2 v_R n_R, \tag{5.4}$$

$$\Delta\nu_P = \rho_P^2 v_P n_P, \tag{5.5}$$

where n_P and n_R are the densities of parent atoms and seed atoms (radiating atoms), respectively, and v_P and v_R are the mean relative speeds of parent atoms-seed atoms and seed atoms-seed atoms, respectively.

They can be written as

$$n_P = (1-\varepsilon)P_0/kT, \tag{5.6}$$

$$n_R = \varepsilon P_0/kT \tag{5.7}$$

$$v_P = \sqrt{(8RT/\pi)(1/M_P+1/M_R)}, \tag{5.8}$$

$$v_R = 4\sqrt{RT/(\pi M_R)}, \tag{5.9}$$

where ε, T, P_0 are seed fraction, temperature and pressure of system, respectively and M_P, M_R are mole weights of parent atoms and radiating atoms, respectively. The optical cross sections of the potassium resonance lines (doublet, λ_0=7665 Å and λ_0=7699 Å) in the potassium seeded argon plasma are written in Table 5.1.

Table 5.1 (T in ^oK)

K*	λ_0(Å)	f_{mn}[51]	ρ_P^2 (Å^2)[52]	ρ_R^2 (Å^2)[52]
$4P_{3/2} - 4S_{1/2}$	7665	0.625	$3.72\times10^2\ T^{-0.2}$	$2.19\times10^5\ T^{-0.5}$
$4P_{1/2} - 4S_{1/2}$	7699	0.326	$3.72\times10^2\ T^{-0.2}$	$1.56\times10^5\ T^{-0.5}$

The total half-widths $\Delta\nu_c$ are in the forms

$$7665\ \text{Å};\ \Delta\nu_c = 8.94\times10^{11}(1-\varepsilon)T^{-0.7} + 5.29\times10^{14}\varepsilon T^{-1}\ (s^{-1}), \tag{5.10}$$

$$7699\ \text{Å};\ \Delta\nu_c = 8.94\times10^{11}(1-\varepsilon)T^{-0.7} + 3.77\times10^{14}\varepsilon T^{-1}\ (s^{-1}). \tag{5.11}$$

The overall shape of absorption coefficient for collision broadening is derived from the electron oscillator treatment of the classical theory as

$$k\nu_c = C_c/\left[1+\left(\frac{\nu-\nu_0}{\Delta\nu_c/2}\right)^2\right] \tag{5.12}$$

where C_c is a constant of proportionality, which is

$$C_c = e^2 n_R f_{mn}/\{4\pi\varepsilon_0 m_e c(\Delta\nu_c/2)\}, \tag{5.13}$$

Notice that the form of Eq.(5.12) has the same frequency dependence

as that of natural broadening.

V.2.3. Stark broadening

The Stark broadening is caused by the external electric field perturbation. In an MHD plasma this effect is due to the existence of many charged particles. Griem[51] has obtained the following estimation of the half-width $\Delta\lambda_{St}$ for neutral emitters.

$$\Delta\lambda_{St} = \Delta\lambda_{Se}\{1+1.75\eta_i(1-0.75\gamma_D)\}, \tag{5.14}$$

for K, λ_0=7665 Å and 7699 Å at T=2500 °K,

$$\Delta\lambda_{Se} = 2.87\times10^{-2}(n_e/10^{22}) \quad (\text{Å}), \tag{5.15}$$

$$\eta_i = 4.8\times10^{-2}(n_e/10^{22})^{1/4}, \tag{5.16}$$

$$\gamma_D = (3/4\pi n_e)^{1/3}\cdot(\varepsilon_0 kT/n_e e^2)^{-1/2}, \tag{5.17}$$

where $\Delta\lambda_{Se}$ is the half-width caused by the radiating atom-electron collisions and η_i, γ_D are the ion broadening parameter and the ratio of Debye radius of electron alone to the mean distance of ions, respectively. The electron number density n_e is in m^{-3}. Assuming Saha equilibrium, the electron number density at T=2500 °K, P_0=1 atm. is calculated as

$$n_e \cong 1.35\times10^{21}\sqrt{\varepsilon} \qquad (m^{-3}). \tag{5.18}$$

Thus, at $\varepsilon=10^{-3}$ for example,

$$\Delta\lambda_{St} \cong 1.25\times10^{-4} \qquad (\text{Å}). \tag{5.19}$$

The overall shape of the Stark broadened line in the wing region is expressed as

$$k_{\nu St} = C_{St}/\left(\frac{\nu-\nu_0}{\Delta\nu_{St}/2}\right)^{5/2}, \quad \text{(wing region)}, \tag{5.20}$$

where C_{St} is a constant independent of frequency.

V.2.4. Doppler broadening[50,53]

Since the radiating atoms have random thermal velocities according to Maxwell's distribution, they show Doppler effect in the resonance line resulting in the following shape

$$k_{\nu_D} = C_D \exp\{-\left(\frac{\nu-\nu_0}{\Delta\nu_D/2}\right)^2 \ln 2\} \tag{5.21}$$

$$\Delta\nu_D = 2\nu_0/c \cdot \sqrt{2RT \ln 2/M_R} \tag{5.22}$$

$$C_D = e^2 n_R f_{mn}/(4\varepsilon_0 m_e \nu_0) \cdot \sqrt{M_R/(2\pi RT)} \tag{5.23}$$

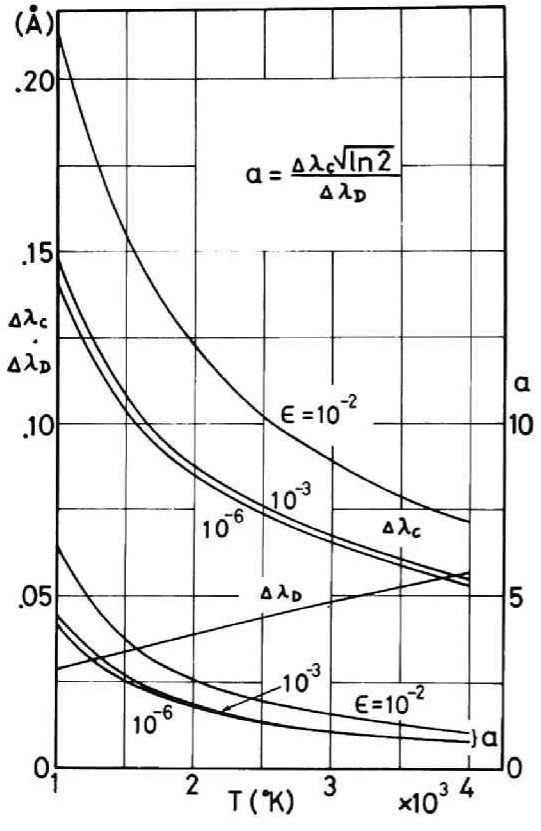

Fig.5.1. Half-widths for collision and Doppler broadenings and the ratio a with respect to the temperature for K, λ_0=7699 Å.

Notice that the strong influence of Doppler effect is limited to the reagion near the line center due to its frequency dependence, while natural or collision broadening plays an important role in the wing region. Half-widths for collision and Doppler broadenings are shown in Fig.5.1 as functions of temperature T and seed fraction ε in their ranges T=1000-4000 °K and $\varepsilon = 10^{-6}$-10^{-2} at atmospheric pressure. The ratio a of the collision broadened half-width to the Doppler broadened one is also shown in Fig.5.1 [see Eq.(5.28)].

V.2.5. Combined natural broadening and collision broadening profile and estimation of Stark broadening

The additional reciprocal life time due to collisions which is proportional to the uncertainty in the occupied energy level can be added to that for natural broadening, since they are involved in the same physical processes. Thus, the total half width $\Delta\nu_t$ can be written as

$$\Delta\nu_t = \Delta\nu_N + \Delta\nu_c, \tag{5.24}$$

and the coefficient C_N in Eq.(5.3) being equal to C_c in Eq.(5.12), the combined shape of absorption coefficient is then written in the form

$$k_\nu = \frac{e^2 n_R f_{mn} / \{4\pi\varepsilon_o m_e c(\Delta\nu_t/2)\}}{1+\{(\nu-\nu_0)/\Delta\nu_t/2\}^2}. \tag{5.25}$$

The above shape expressed by Eq.(5.25) will be referred to "pure dispersion broadening" hereafter. Comparing $\Delta\nu_N$ with $\Delta\nu_c$, the relationship $\Delta\nu_c >> \Delta\nu_N$ always holds in the region we are interested in, hence we may ignore $\Delta\nu_N$, and $\Delta\nu_c$ will stand for $\Delta\nu_t$ hereafter.

The absorption coefficient for collision broadening shows $(\nu-\nu_0)^{-2}$ frequency dependence, whereas the Stark broadening shows $(\nu-\nu_0)^{-5/2}$ frequency dependence in the wing region. Consequently, in the wing region far from the line center, the Stark broadening may be ignored if $\Delta\nu_{St} \simeq \Delta\nu_c$ and also it can be reasonably ignored if $\Delta\nu_{St} << \Delta\nu_c$ The latter condition is satisfied at $T=2500\ ^oK$ from Eq.(5.19) and Fig. 5.1. Hence we may consider only collision broadening and Doppler broadening in practice.

V.2.6. Combined collision broadening and Doppler broadening profile [52]

The combined profile of absorption coefficient can be written as

$$P_a = k_{|\xi|}/k_0 = (a/\pi) \int_{-\infty}^{\infty} \frac{exp(-y^2)}{a^2+(\xi-y)^2}\, dy, \qquad (5.26)$$

where

$$k_0 = e^2 n_R f_{mn} \lambda_0 / (4\varepsilon_0 m_e c) \cdot \sqrt{M_R/(2\pi RT)}\ , \qquad (5.27)$$

$$a = \Delta\nu_c \sqrt{ln\ 2}/\Delta\nu_D, \qquad (5.28)$$

$$\xi = (\nu-\nu_0)/\nu_0 \cdot \sqrt{M_R c^2/(2RT)} = (\nu-\nu_0)\sqrt{ln\ 2}/(\Delta\nu_D/2). \qquad (5.29)$$

The theoretical representation of P_a suitable for numerical calculations were obtained as follows:

$$P_a = exp(a^2-\xi^2)\{cos(2a\xi)erfc(a)+exp(-a^2)[1-cos(2a\xi)]/2\pi a$$
$$-4a/\pi \cdot exp(-a^2) \sum_{n=1}^{\infty} exp(-n^2/4)/(n^2+4a^2)[cos(2a\xi)-cosh(n\xi)]\}, \qquad (5.30)$$

for moderate or small values of ξ, and

$$P_a = \{a\sqrt{\pi}[1+(\xi/a)^2]\}^{-1} \cdot \{1-1/(2a^2) \cdot [1-\binom{3}{2}(\xi/a)^2]/[1+(\xi/a)^2]^2$$
$$+3/(2a^2)^2[1-\binom{5}{2}(\xi/a)^2+\binom{5}{4}(\xi/a)^4]/[1+(\xi/a)^2]^4+\cdots\cdots\} \qquad (5.31)$$

for $\xi/a >> 1$, where $\binom{n}{m}=n!/[m!(n-m)!]$ is the binominal coefficient.

For pure Doppler broadening and pure dispersion broadening, the absorption coefficient can be expressed as follows:

$$P_a = exp(-\xi^2); \qquad \text{pure Doppler broadening,} \qquad (5.32)$$

$$P_a = 1/a\sqrt{\pi} \cdot 1/\{1+(\xi/a)^2\}; \quad \text{pure dispersion broadening.} \qquad (5.33)$$

The calculations based on Eqs.(5.30)-(5.33) are shown in Fig.5.2 for $\varepsilon=10^{-3}$. It is seen from the figure that the difference between combined form and pure dispersion form is almost negligible for $\lambda-\lambda_0>0.1$Å, and it is very little, if any, for $\lambda-\lambda_0 \leqq 0.1$ Å when the ratio a is

large (i.e., low temperature). Therefore at low temperatures, the combined form may be well approximated by pure dispersion form. Even in the region of small a (i.e., high temperature), it is only for $\lambda-\lambda_0 \leq 0.1$ Å that the difference becomes clear.

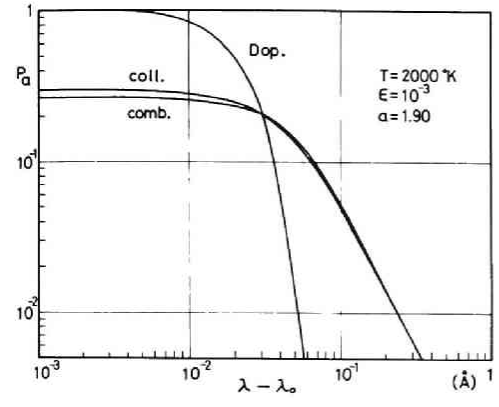

Fig.5.2. Absorption coefficients for collision and Doppler broadening and combined absorption coefficient at T=2000 °K.

As this remarkable difference exists only near the line center, the influence of this approximation on the specific intensity contour is small. This can be seen from the following explanation. Assuming T to be constant, the specific intensity I_λ at the wave length λ can be written as

$$I_\lambda = B_\lambda(T)\{1-exp(-k_\lambda \ell)\} \quad (5.34)$$

where ℓ, $B_\lambda(T)$ are the interaction length of the light with the plasma and Planck function, respectively. Thus the deviation of intensity with respect to k_λ becomes as

$$\delta I_\lambda = \ell B_\lambda(T) exp(-k_\lambda \ell)\delta k_\lambda. \quad (5.35)$$

Since the value of k_λ near the line center is very large, $exp(-k_\lambda \ell)$ may be estimated to be nearly zero and thus $\delta I_\lambda = 0$.

Accordingly, for the temperature below 3000 °K, one may use pure dispersion profile instead of complicated combined profile without considerable error. In the following calculations, we thus consider only pure dispersion profile due to collision broadening.

V.3. Basic equation of radiation field

The following assumptions are made:

(1) The radiation field is in local thermodynamic equilibrium.

(2) Continuum radiation is negligible near the resonance line.

(3) Atoms and electrons in the plasma are in thermal equilibrium at

the temperature T.

(4) The population distribution of excited levels of radiating atoms is Maxwellian at a temperature T and the transitions of the atomic state are caused mainly by electron collisions.

(5) The temperature of the plasma has the following spatial distribution in the observation direction

$$T = T_w + (T_c - T_w)f(x), \qquad (0 \leq f(x) \leq 1), \tag{5.36}$$

where T_c and T_w are temperatures at the plasma center and the wall (surface of the plasma), respectively. The temperature range is restricted between *1500 °K* and *2000 °K* and the spatial distribution function $f(x)$ is symmetric with respect to the plasma center.

Under these assumptions, the equation of the radiation field may be written as

$$1/c \cdot \partial I_\lambda/\partial t + \partial I_\lambda/\partial s = k_\lambda(B_\lambda(T) - I_\lambda), \tag{5.37}$$

where I_λ, B_λ are specific intensity and Planck function, and k_λ is the absorption coefficient expressed by Eq.(5.25), since induced radiation can be neglected under the conditions discussed here.

At the steady state, Eq.(5.37) can be integrated with the result

$$I_\lambda(\ell) = I_\lambda(0)exp\{-\tau_\lambda(\ell,0)\} + \int_0^\ell k_\lambda(T)B_\lambda(T)exp\{-\tau_\lambda(\ell,s)\}ds, \tag{5.38}$$

where $I_\lambda(0)=I_\lambda(s=0)$. Here the optical thickness of the layer $\tau_\lambda(s,s')$ is defined as

$$\tau_\lambda(s,s') = \int_s^{s'} k_\lambda(T)ds. \tag{5.39}$$

V.4. Measuring geometry and method

The measuring configuration for the line-reversal method is illustrated in Fig.5.3. The plasma is contained in the region between $s=0$ and $s=\ell$ where the direction s denotes the direction of observation. The W-lamp of known brightness temperature is set on the line s (opti-

cal axis) and the light from the W-lamp goes through the plasma into the inlet slit of the spectroscope. The light from the W-lamp is focused at the plasma center ($s=\ell/2$) and the inlet slit of the spectroscope, respectively. The light emitted from the W-lamp is received by photomultipliers P.M.1 and P.M.2 whose outputs are connected to the X- and Y-axes of an X-Y recorder, respectively. The spectral shape on the focal plane of the spectroscope is sharp in ideal case, but, in practice, because of the finite width of the inlet slit of the spectroscope, distortion occurs. The distorted spectral shape characterized by a superposed width δ can be calculated by integrating the spectral shape with no distortion. The superposed width δ and the wave length region ($\lambda_0-\Delta/2$, $\lambda_0+\Delta/2$) covered by P.M.2 are shown in Fig.5.4.

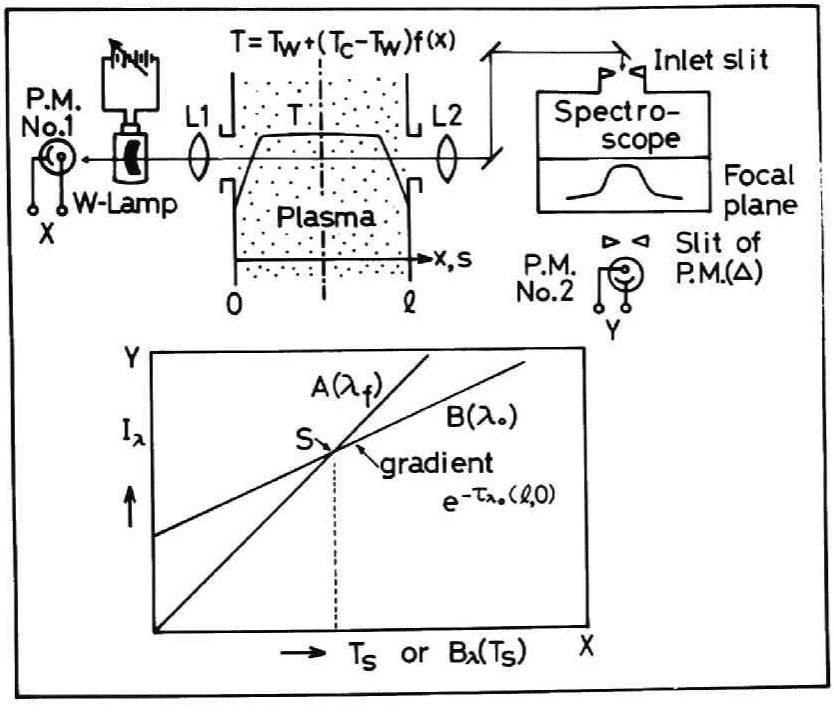

Fig.5.3. Measuring configuration of the line-reversal method.

Specific intensity $A(\lambda_f)$ corresponds to the equivalent specific intensity expressed by Eq.(5.41) and $B(\lambda_0)$ corresponds to Eq.(5.40) in the case of λ_0.

Under the conditions, the line-reversal temperature(LRT) is defined as follows.

V.4.1. $\delta=0$ Å

The specific intensity of the light at the wave length λ emitted from the W-lamp (the brightness temperature T_s) through the plasma is written as

$$I_\lambda(T_s) = B_\lambda(T_s)exp[-\tau_\lambda(\ell,0)]+\int_0^\ell k_\lambda(T)B_\lambda(T)exp[-\tau_\lambda(\ell,s)]ds. \quad (5.40)$$

In the absence of the plasma, the specific intensity is given by

$$I_\lambda(T_s) = B_\lambda(T_s). \quad (5.41)$$

When specific intensities in Eqs.(5.40) and (5.41) are equal, the following equation holds

$$B_\lambda(T_s) = B_\lambda(T_s)exp\{-\tau_\lambda(\ell,0)\} + \int_0^\ell k_\lambda(T)B_\lambda(T)exp\{-\tau_\lambda(\ell,s)\}ds. \quad (5.42)$$

The temperature satisfying Eq.(5.42) is defined as the line-reversal temperature at the wave length λ.

At a constant plasma temperature, Eq.(5.42) is reduced to

$$B_\lambda(T_s) = B_\lambda(T), \quad (5.43)$$

showing that the LRT is equal to the plasma temperature. In the next place, we define the averaged LRT T_Δ over the region $(\lambda_0-\Delta/2,\ \lambda_0+\Delta/2)$ as

$$\int_{\lambda_0-\Delta/2}^{\lambda_0+\Delta/2} B_\lambda(T_\Delta)\{1-exp[-\tau_\lambda(\ell,0)]\}d\lambda = \int_{\lambda_0-\Delta/2}^{\lambda_0+\Delta/2} J_\lambda d\lambda, \quad (5.44)$$

where

$$J_\lambda = \int_0^\ell k_\lambda(T)B_\lambda(T)exp\{-\tau_\lambda(\ell,s)\}ds. \quad (5.45)$$

Since $\Delta/\lambda_0 \ll 1$, The left-hand side of Eq.(5.44) can be written as

$$\int_{\lambda_0-\Delta/2}^{\lambda_0+\Delta/2} B_\lambda(T_\Delta)\{1-exp[-\tau_\lambda(\ell,0)]\}d\lambda = B_{\lambda_0}(T_\Delta)\int_{\lambda_0-\Delta/2}^{\lambda_0+\Delta/2}\{1-exp[-\tau_\lambda(\ell,0)]\}d\lambda. \quad (5.46)$$

For large $\tau_\lambda(\ell,0)$, Eq.(5.42) is reduced to

$$B_\lambda(T_s) = B_\lambda(T)\Big|_{s=\ell} = B_\lambda(T_w). \tag{5.47}$$

For small $\tau_\lambda(\ell,0)$, on the other hand, Eq.(5.42) is expressed by

$$B_\lambda(T_s) = \int_0^\ell k_\lambda(T)B_\lambda(T)ds/\tau_\lambda(\ell,0). \tag{5.48}$$

It is to be notable that the LRT T_s satisfying Eq.(5.48) corresponds to the asymptotic LRT $T_{s\infty}$ at $|\lambda-\lambda_0| \to \infty$ and is independent of the interaction length ℓ.

V.4.2. $\delta \neq 0$ Å

Because of the finite width of the slit, the distorted spectral shape appears as shown in Fig.5.4 (dotted curve).

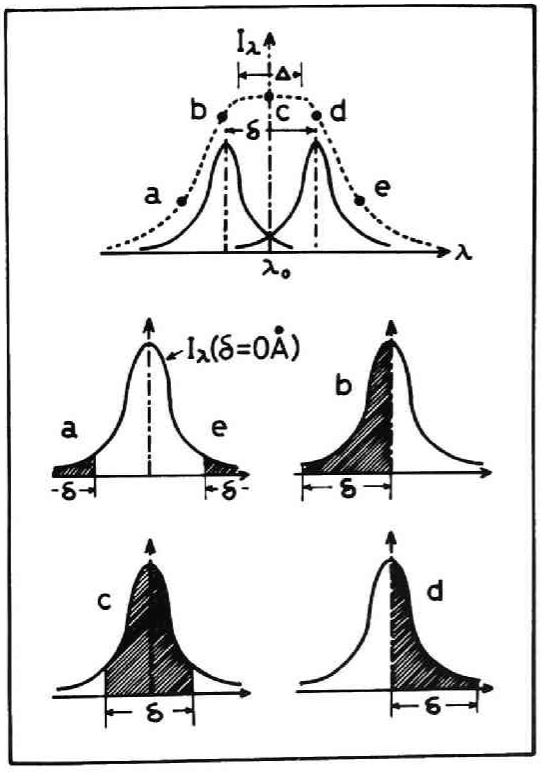

Fig.5.4. Distorted spectral shape(dotted curve) on the focal plane of the spectroscope.

δ and Δ are the superposed width and the spectral region covered by a photomultiplier. Intensities at points a,b,c,d *and* e *are calculated by integrating a non-distorted spectral shape(region of oblique lines).*

In this case the LRT T_s at the wave length λ is defined as

$$1/\delta \cdot \int_{\lambda-\Delta/2}^{\lambda+\Delta/2} B_\lambda(T_s)\{1-exp[-\tau_\lambda(\ell,0)]\}d\lambda = I_t(\lambda), \tag{5.49}$$

where

$$I_t(\lambda) = 1/\delta \cdot \int_{\lambda-\delta/2}^{\lambda+\delta/2} J_\lambda d\lambda. \tag{5.50}$$

The average LRT T_Δ over the region $(\lambda_0-\Delta/2,\ \lambda_0+\Delta/2)$ is similarly defined as

$$\int_{\lambda_0-\Delta/2}^{\lambda_0+\Delta/2} B_{t\lambda}(T_\Delta)d\lambda = \int_{\lambda_0-\Delta/2}^{\lambda_0+\Delta/2} I_t(\lambda)d\lambda, \tag{5.51}$$

where

$$B_{t\lambda}(T_\Delta) = 1/\delta \cdot \int_{\lambda-\delta/2}^{\lambda+\delta/2} B_\lambda(T_\Delta)\{1-exp[-\tau_\lambda(\ell,0)]\}d\lambda. \tag{5.52}$$

In order to know the influence of the optical thickness upon LRT, we introduce for convenience the following terms concerning optical thickness:

$$L_k = \{1/\tau_\lambda(\ell,0)\}\times 100\ \%, \tag{5.53}$$

$$L_{10} = \{(\ell-\ell_{90})/\ell\}\times 100\ \%, \tag{5.54}$$

$$L_{50} = \{(\ell-\ell_{50})/\ell\}\times 100\ \%, \tag{5.55}$$

$$L_{90} = \{(\ell-\ell_{10})/\ell\}\times 100\ \%, \tag{5.56}$$

where

$$I_\lambda(y) = \int_0^y k_\lambda(T)B_\lambda(T)exp[-\tau_\lambda(\ell,s)]ds, \tag{5.57}$$

$$I_\lambda(\ell_j) = (j/100)\times I_\lambda(\ell). \tag{5.58}$$

By these terms, we can estimate the degree of contribution from the plasma layers to the measured intensity.

V.5. Results of calculations

All calculations were made for the potassium resonance line (λ_0= *7699 Å*) at $\varepsilon=10^{-3}$ and atmospheric pressure. Under the condition the specific intensity I_λ and the LRT T_s may be regarded as being almost symmetric with respect to the resonance line center.

V.5.1. Constant temperature

At a constant temperature (T=*2000 °K*), spectral intensities emitted from the plasma alone are shown for ℓ=*1* and *10 cm* in Fig.5.5 (solid curves). Since the intensity emitted from the plasma is proportional to $[1-\exp(-k_\lambda \ell)]$, the spectral shape thus shows sharp peak around the line center for small ℓ. With increasing δ, the shape becomes flattened and the intensity also decreases. The dotted curves show intensities of the light emitted from the W-lamp at $T_s = T_w$ and δ=*0 Å* after passing through the plasma.

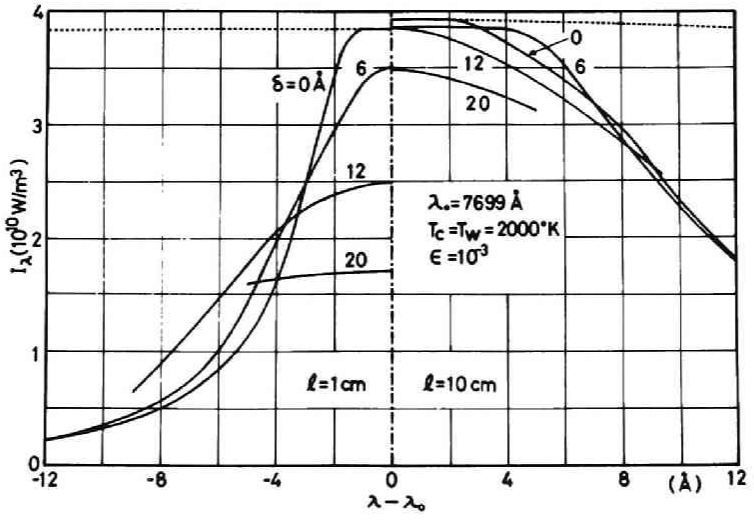

Fig.5.5. Intensity profiles of a constant temperature for ℓ=1 cm and 10 cm.

V.5.2. Variable temperatures

Three spatial distribution functions of the temperature are chosen as follows(see Fig.5.6):

$$f_1(x) = |1-2x/\ell|, \tag{5.59}$$

$$f_2(x) = (1-|1-2x/\ell|)^{1/7}, \tag{5.60}$$

$$f_3(x) = \sin(\pi x/\ell). \tag{5.61}$$

The spatial distribution function $f_2(x)$, often encountered in an MHD experiment, changes remarkably large at the boundary of the plasma, and $f_3(x)$ is chosen to compare with $f_2(x)$. $f_1(x)$ is also chosen as the special case where the temperature at the boundary is highest. Spectral intensity profiles in case of $f_1(x)$ and $f_2(x)$ for ℓ=1 and 10 *cm* are shown in Figs.5.7 and 5.8, respectively. The conditions of solid and dotted curves are same as in the section V.5.1. It is obvious that the intensity near the line center is independent of the intensity emitted from the W-lamp because of a large optical thickness of the plasma. It is also seen from Fig.5.8 that self-reversal occurs for distributions having a maximum temperature at the plasma center, and with increasing δ the concave shape particular to the self-reversal phenomenon deminishes. The LRTs for each distribution function are shown in Figs.5.9 and 5.10. For the function $f_1(x)$, the LRT has a maximum at the line center for small δ and it is equal to the plasma temperature T_w in case of δ=0 Å as predicted in Eq.(5.47). By similar reasoning, the LRT in cases of $f_2(x)$ and $f_3(x)$ has

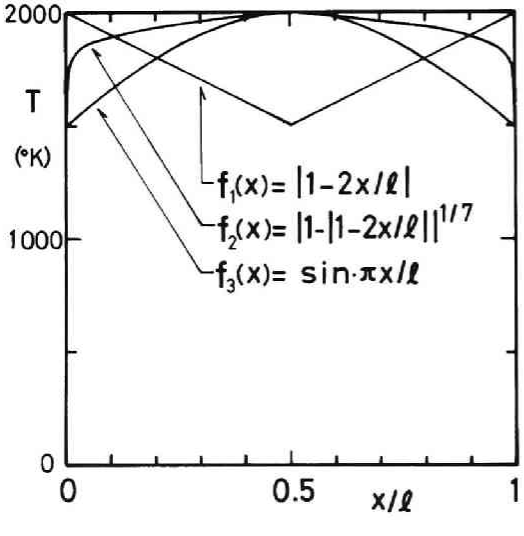

Fig.5.6. Three spatial distribution functions of plasma temperature.

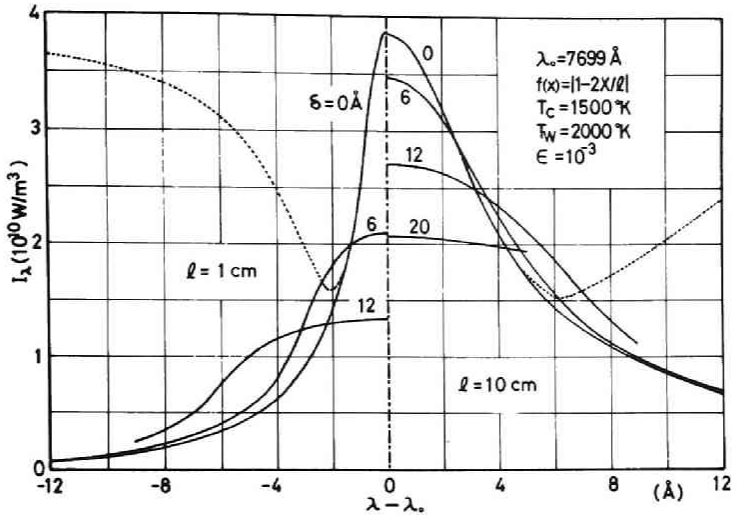

Fig.5.7. Intensity profiles in case of $f_1(x)$ for ℓ=1 cm and 10 cm.

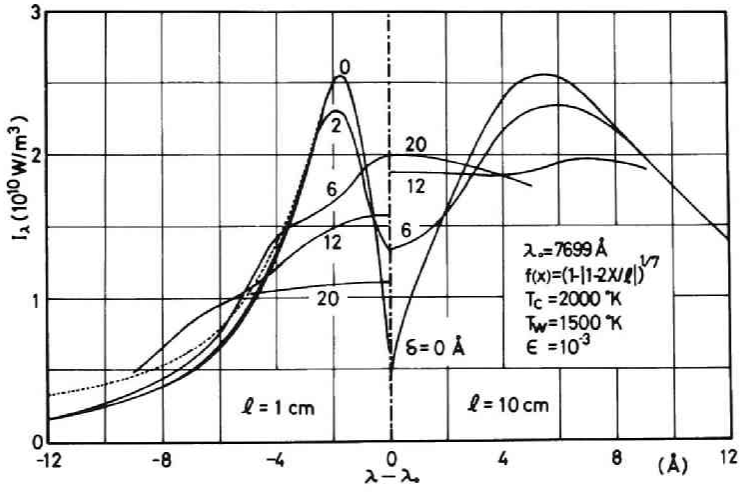

Fig.5.8. Intensity profiles in case of $f_2(x)$ for ℓ=1 cm and 10 cm.

a minimum at the line center. These figures show that the LRT depends greatly both on the spatial distribution function and on the superposed width. The LRT experimentally obtained[49] shows a similar tendency to that in Fig.5.10 at moderate δ.

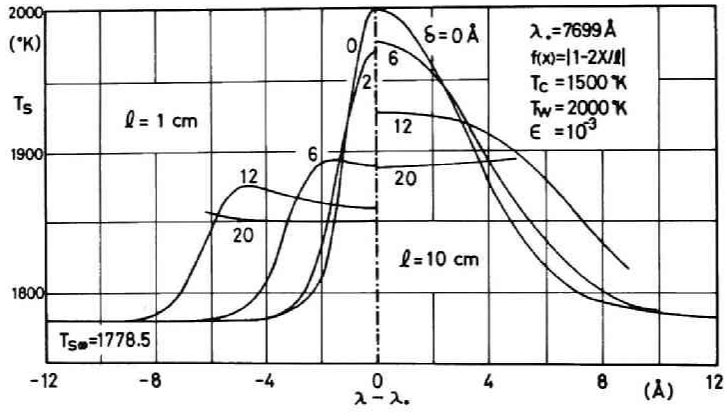

Fig.5.9. Line-reversal temperatures in case of $f_1(x)$ (Δ=0 Å) for ℓ=1 cm and 10 cm.

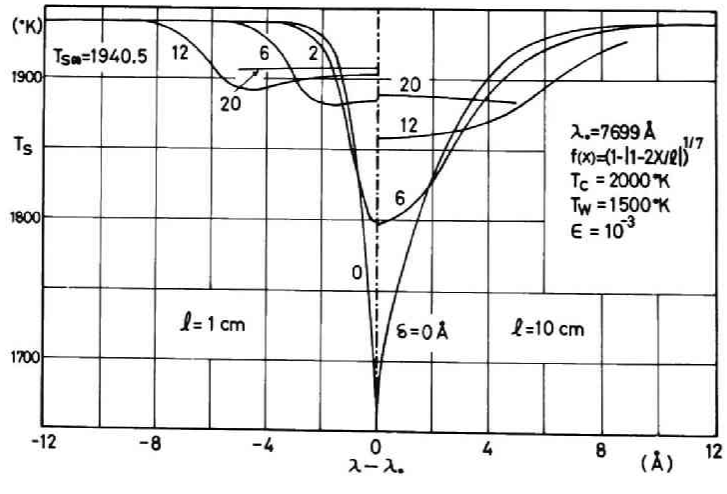

Fig.5.10. Line-reversal temperatures in case of $f_2(x)$ (Δ=0 Å) for ℓ=1 cm and 10 cm.

The temperature T_Δ including effects of both δ and Δ are shown in Figs. 5.11-5.13. With increasing Δ, every curve approaches to the curve with $\delta=0$ Å, and T_Δ will be almost independent of δ, if Δ is taken at least 20 Å for every case in these figures. Comparing these average LRTs at large Δ with each other, T_Δ in case of $f_2(x)$ is closest to the temperature at the plasma center, because it holds higher temperatures to the vicinity of the plasma boundary. The asymptotic LRT $T_{\Delta\infty}$ at large Δ is shown in Fig.5.14 with respect to the product of seed fraction and interaction length, $\varepsilon \cdot \ell$, which is proportional to the optical thickness.

From the point of view of an MHD experiment, it will not be desirable that the observed LRT depends greatly on δ or Δ. This is partly because it is impossible to explain the observed LRT in connection with the coupled function of δ or Δ with the unknown spatial distri-

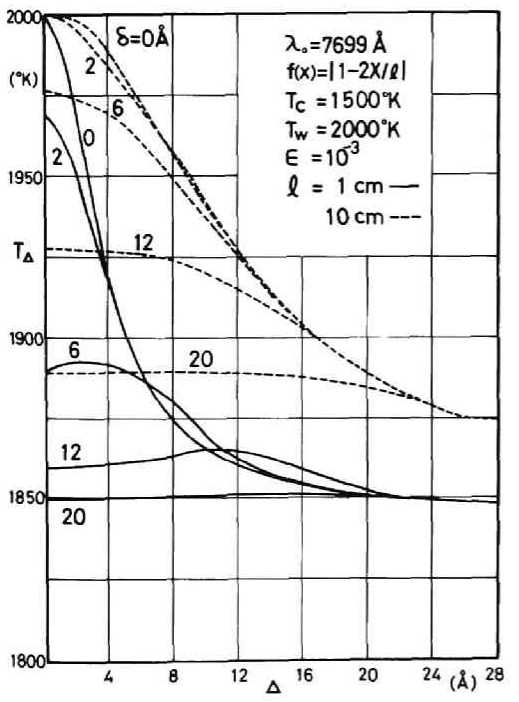

Fig.5.11. Average line-reversal temperatures in case of $f_1(x)$ for ℓ=1 cm and 10 cm.

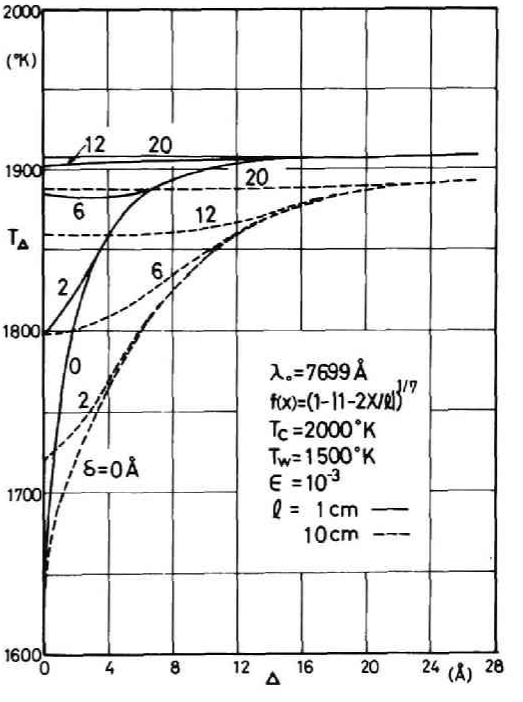

Fig.5.12. Average line-reversal temperatures in case of $f_2(x)$ for ℓ=1 cm and 10 cm.

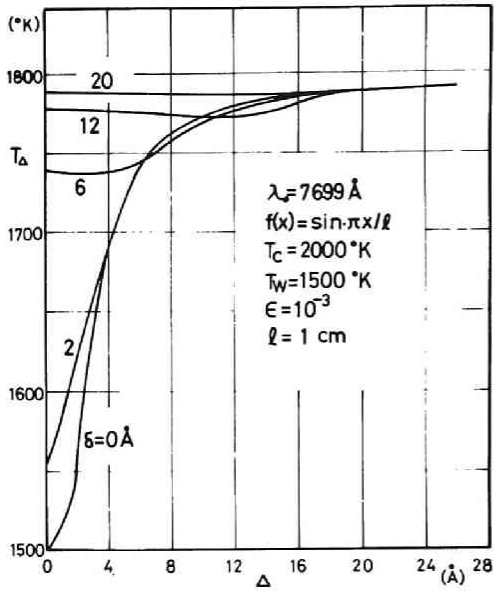

Fig.5.13. Average line-reversal temperatures in case of $f_3(x)$ for ℓ=1 cm.

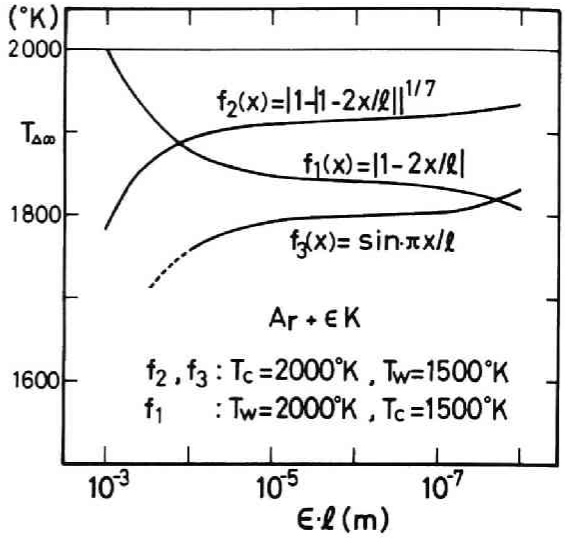

Fig.5.14. Asymptotic average line-reversal temperatures with respect to the product of seed fraction and physical length of the plasma.

bution of the plasma temperature, and partly because it is hoped to measure the LRT closest to that at the plasma center (or that of core region) by which a theoretical electrical conductivity or other properties can be determined. It should be noted that the superposed width δ and the spectral region covered by the photomultiplier Δ are interchangeable when either of them is small.

L_k, L_{10}, L_{50} and L_{90} for $f_2(x)$ is shown in Fig.5.15. From the curve of L_{90} in case of ℓ=1 cm, it is seen that the contribution to the observed intensity is made mainly by the plasma surface with respect to the resonance line center and the plasma is optically very thick. For the wave length smaller than λ_0+2 Å the variation is very large resulting in 70% at λ_0+2 Å. This variation corresponds to that of absorption coefficient near the resonance line center. And L_{50} reaches only 30% at λ_0+2 Å. These L_{50} and L_{90} show that the major

contribution to the observed intensity is made from the vicinity of the plasma surface. In the case of larger optical thickness as ℓ=10 cm in Fig.5.15, this tendency becomes more prominent. It is also seen that L_k inversely proportional to the optical thickness stays between L_{50} and L_{90} for small $|\lambda-\lambda_0|$.

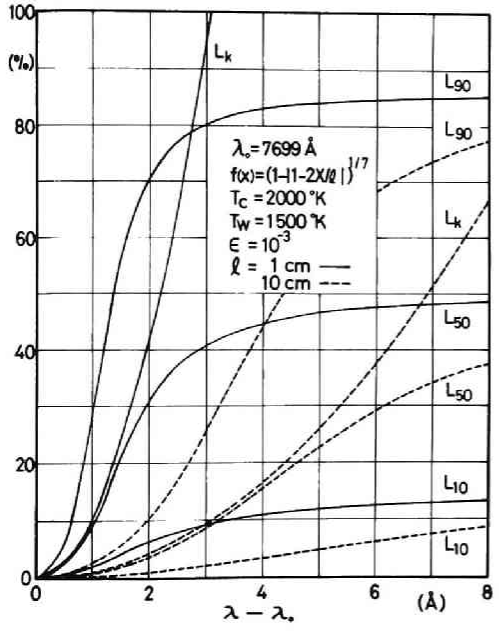

Fig.5.15. L_{10}, L_{50}, L_{90} and L_k in case of $f_2(x)$ for ℓ=1 cm and 10 cm.

V.6. Concluding remarks

Considering absorption coefficient, we can get good approximation by using collision broadening alone under the condition discussed here. In the case of δ=0 Å, the intensity profile is very sharp, and with increasing δ its variation with respect to the wave length becomes small. Particularly, self-reversal phenomenon can not be distinguished for large δ. The line-reversal temperature T_s takes T_w at the resonance line center for δ=0 Å for an optically thick plasma, and with increasing δ, T_s vs. $\lambda-\lambda_0$ curve becomes flattened resulting in a constant temperature at δ=20 Å near the resonance line center and it

approaches $T_{s\infty}$. As for T_{Δ} including effects of δ and Δ, the average LRT should be observed by widening δ or Δ to some degree in order to get as much information as possible from the inner region of th plasma. It is, however, very difficult to guess the temperature in the inner region of the plasma from these observed LRTs, since they are very sensitive to the spatial distribution of the plasma temperature and to the measuring configuration as foreseen. The observed LRT hence must be interpretted taking much care of these respects.

SUMMARY AND CONCLUSION

The nonuniformity of the MHD plasma has much influence on the electrical performance of MHD generators. It is needless to say that this phenomenon is not desirable from the point of view of effective MHD generation, but it must be taken for granted at the same time as an inherent property attached to the slightly ionized gas plasma.

Several proposals both theoretical and experimental have been successfully made in order to get rid of the causes of the nonuniformity, but in the final estimation of its effectiveness, it should be checked whether the output power density can be increased by them or not.

Among many phenomena causing nonuniformities in the MHD plasma, Ionization instability seems not so detrimental to the performance of MHD generators under practical MHD operation conditions. This conclusion is, however, based on Eq.(4.21), and thus it needs to be established using more exact expressions applicable to various conditions.

With respect to the nonuniformity due to current concentration at the electrode edge, it can be remarkably reduced by using resistive electrodes and this method seems very promising particularly to the nonequilibrium MHD generation. It is, however, necessary that the proposal mentioned in this paper should be not only analyzed more in detail including nonequilibrium ionization effects, but also checked experimentally.

Bald but well deliberate proposals for the reduction of the nonuniformity are expected in the future and only those accompanied with the originality will be useful to the early realization of the effective MHD generation operated in the nonequilibrium state.

APPENDICES

Appendix A. Boundary condition and formulation of equations by the difference method

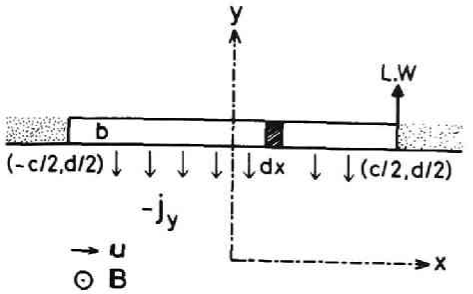

Fig.A.1. Configuration of upper wall.

1. Equation (2.12) can be shown to be valid for the upper electrode as follows.

The resistance of an element of length dx of an electrode is

$$\rho dx/(wb), \tag{A.1}$$

where ρ, w and b are electrode resistivity, electrode length in the z direction and electrode thickness in the y direction, respectively(see Fig.A.1).

The current that flows through this element dx is

$$w \int_{-c/2}^{x} -j_y dx. \tag{A.2}$$

Therefore the potential difference $d\phi$ in dx is

$$d\phi = \rho dx/wb \cdot w \int_{-c/2}^{x} -j_y dx. \tag{A.3}$$

Since $E_x^* = E_x = -d\phi/dx$, Eq.(2.12) holds.

2. Calculations have been performed in the region of $-d/2 \leqq x \leqq d/2$, $0 \leqq y \leqq d/2$, for the reason that the current flux function ψ' satisfies the relation

$$\psi'(x',y') = 1-\psi'(-x',-y'). \tag{A.4}$$

This can easily be proved as described below.

Changing the variables into

$$\Psi' = 1-\psi', \tag{A.5}$$

$$X = -x', \quad Y = -y', \tag{A.6}$$

and substituting Eqs.(A.5) and (A.6) into Eqs.(2.15)-(2.20),

$$\partial^2\Psi/\partial X^2+\partial^2\Psi/\partial Y^2 = 0; \qquad -1/2\leqq X\leqq 1/2, \ -1/2<Y<1/2, \tag{A.7}$$

$$\Psi = 1; \qquad c/2d<X\leqq 1/2, \ Y=\pm 1/2, \tag{A.8}$$

$$\Psi = 0; \qquad -1/2\leqq X<-c/2d, \ Y=\pm 1/2, \tag{A.9}$$

$$1-\Psi(-X,-Y) = -\Psi(1-X,-Y), \tag{A.10}$$

$$\partial\Psi/\partial Y-\beta_e\partial\Psi/\partial X = -\alpha(1-\Psi); \qquad |X|\leqq c/2d, \ Y=-1/2, \tag{A.11}$$

$$\partial\Psi/\partial Y-\beta_e\partial\Psi/\partial X = -\alpha\Psi; \qquad |X|\leqq c/2d, \ Y=1/2. \tag{A.12}$$

Eqs.(A.7)-(A.12) have the same form as Eqs.(2.15)-(2.20). Therefore, Eq.(A.4) holds, and the analysis can be made only in the region of positive y. Since the ends of the electrode are the singular points in the calculation, the number of square meshes is chosen to be 48 in the region of $4/13\leqq y'\leqq 1/2$ and to be 24 in the region of $0\leqq y'\leqq 4/13$ in order to obtain more detailed information around these edges.

Appendix B. Linear perturbation theory for ionization instability

In the linear perturbation analysis, following equations are used[16].

Continuity equation of electrons;

$$Dn_e/Dt = a_i n_e(n_{s0}-n_e)-k_r n_e^3 = k_r\{S(T_e)n_e(n_{s0}-n_e)-n_e^3\}. \quad (B.1)$$

Energy equation of electrons;

$$D\{n_e(3kT_e/2+eV_i)\}/Dt = \bar{j}^2/\sigma-A-Q_r. \quad (B.2)$$

Ohm's law;

$$\bar{j} = \sigma\bar{E}^*-(\beta_e/B)\bar{j}\times\bar{B}, \quad (B.3)$$

$$\bar{E}^* = \bar{E} + \bar{u}\times\bar{B}. \quad (B.4)$$

Saha's equation;

$$S(T_e) = \frac{n_e}{n_{s0}-n_e} = \left(\frac{2\pi m_e kT_e}{h^2}\right)^{3/2} exp\left(\frac{-eV_i}{kT_e}\right) \quad (B.5)$$

Maxwell's equation;

$$div\ \bar{j} = 0, \quad (B.6)$$

$$rot\ \bar{E} = 0. \quad (B.7)$$

Collision loss of electrons;

$$A = \frac{3}{2} kn_e(T_e-T_g) \sum_j \frac{m_e}{m_a} \nu_{ej}\ \delta_j, \quad (B.8)$$

where a_i, k_r are ionization coefficient and recombination coefficient, respectively, n_{s0}, eV_i being initial number density of a seed material and its ionization energy, k, h and δ_j being Boltzmann's constant, Planck's constant and collision loss parameter of electron with the

j-th component, respectively. In the analysis, $\overline{u}$ is assumed to be zero, hence $\overline{E}^*$ and mobil operator D/Dt are reduced to $\overline{E}$ and d/dt, respectively. In Figs.B.1-B.4, A, σ and $\nu_e (=\sum_j \nu_{ej})$ are shown for several set of pressure, temperature and seed fraction. It should be noted that all these quantities vary rapidly at the electron number density corresponding to $(\beta_{cr})_{max}$.

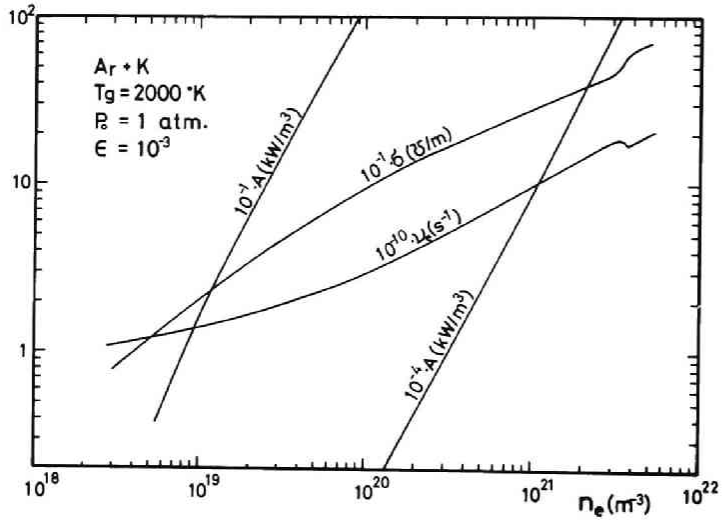

Fig.B.1. Properties of the plasma for T_g=2000 °K, P_0=1 atm. and $\varepsilon=10^{-3}$.

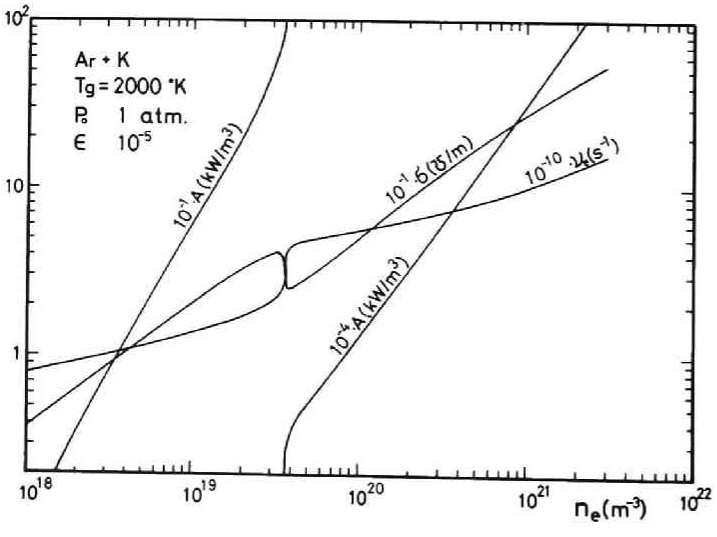

Fig.B.2. Properties of the plasma for T_g=2000 °K, P_0=1 atm. and $\varepsilon=10^{-5}$.

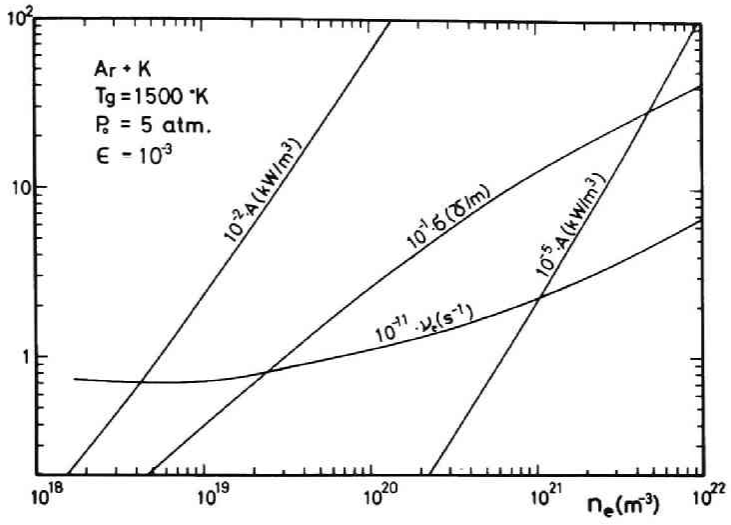

Fig.B.3. Properties of the plasma for T_g=1500 °K, P_0=5 atm. and $\varepsilon=10^{-3}$.

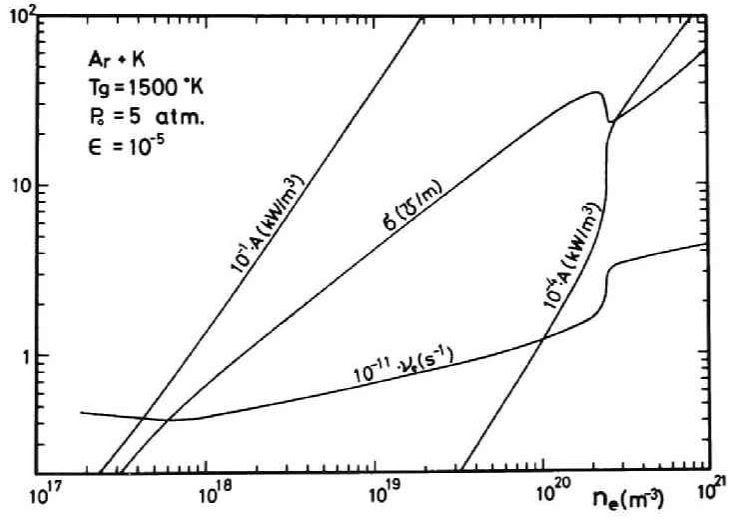

Fig.B.4. Properties of the plasma for T_g=1500 °K, P_0=5 atm. and $\varepsilon=10^{-5}$.

Let's assume that n_e and T_e are initially uniform in space and then change to n_e+n_e' and T_e+T_e', respectively where n_e' and T_e' are perturbed terms independent of space. Under these assumptions the following relationship is obtained from Eq.(B.5)

$$S'/S = (3/2+eV_i/kT_e)T_e'/T_e, \tag{B.9}$$

and Eq.(B.1) is reduced to

$$dn_e'/dt = k_r S' n_e (n_{so}-n_e)+Sn_e'(n_{so}-2n_e)-3n_e^2 n_e'. \tag{B.10}$$

Assuming instantaneous Saha equilibrium ($dn_e'/dt=0$), we obtain

$$S'n_e'(n_{so}-2n_e)+S'n_e(n_{so}-n_e)-3n_e^2 n_e' = 0. \tag{B.11}$$

From Eqs.(B.5),(B.9) and (B.11) n_T is defined as

$$\begin{aligned} n_T &= d(\ln n_e)/d(\ln T_e) = (n_e'/n_e)/(T_e'/T_e) \\ &= (3/2+eV_i/kT_e)(n_{so}-n_e)/(2n_{so}-n_e) \\ &= (3/2+eV_i/kT_e)\{(1-\alpha_i)/(2-\alpha_i)\}, \end{aligned} \tag{B.12}$$

where α_i is the ionization degree defined as

$$\alpha_i = n_e/n_{so}. \tag{B.13}$$

Similarly, Eq.(B.2) is reduced to

$$(3kn_e/2)dT_e'/dt+(3kT_e/2+eV_i)dn_e'/dt = 2\bar{j}\cdot\bar{j}'/\sigma-j^2\sigma'/\sigma^2-A'. \tag{B.14}$$

In deducing Eq.(B.14) Q_r was assumed to be negligible.

Here we assume the perturbed term Y' in the form

$$Y' \propto exp(i\omega t) = exp(\omega_i t)exp(i\omega_r t), \tag{B.15}$$

$$\omega = \omega_r - i\omega_i, \tag{B.16}$$

where ω is a complex angular velocity and its imaginary part ω_i is a growth rate.

Substitution of Eq.(B.15) into Eq.(B.14) then yields

$$\omega_i\{3kn_eT_e'/2+(3kT_e/2+eV_i)n_e'\}T_e/T_e' = (2\bar{j}\cdot\bar{j}'/\sigma)T_e/T_e'$$

$$-j^2\sigma' T_e/(\sigma^2 T_e') - A' T_e/T_e'$$

$$= (2\bar{j}\cdot\bar{j}'/\sigma) T_e/T_e' - (j^2/\sigma)\sigma_T - A_T A, \qquad (B.17)$$

where

$$\sigma_T = d(ln\ \sigma)/d(ln\ T_e), \qquad (B.18)$$

$$A_T = d(ln\ A)/d(ln\ T_e). \qquad (B.19)$$

Next, we consider the term $(2\bar{j}\cdot\bar{j}'/\sigma)T_e/T_e'$ appeared in the right-hand side of Eq.(B.17).

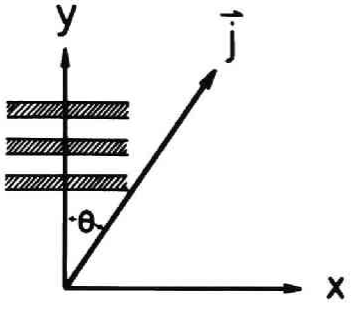

Fig.B.5. Pattern of ionization instability wave. Wave propergates in y direction.

The perturbation is assumed to propagate in the y direction as a plane wave as seen in Fig.B.5. From Eq. (B.3) the respective current components are reduced to

$$j_x = \sigma E_x - \beta_e j_y, \qquad (B.20)$$

$$j_y = \sigma E_y + \beta_e j_x, \qquad (B.21)$$

and for such wave of perturbation, Maxwell's formulas readily give

$$j_y' = 0, \qquad (B.22)$$

$$E_x' = 0, \qquad (B.23)$$

where charge neutrality was assumed and this is not true in the strict sence, since space charge electric fields occur as a result of the fluctuations. But due to relatively small difference in electron and ion number densities compared with the fluctuation in the amplitude of the two number densities this assumption may be reasonable[17].

Use of Eqs.(B.20) and (B.21) together with Eqs.(B.22) and (B.23) yields

$$j_x' = \sigma' E_x - \beta_e j_y = j(\sigma'/\sigma)(sin\theta + \beta_e cos\theta) - \beta_e' j cos\theta, \qquad (B.24)$$

$$E_x = (j_x + \beta_e j_y)/\sigma = (j/\sigma)(sin\theta + \beta_e cos\theta), \qquad (B.25)$$

where θ is the angle made by the y axis and the unperturbed (averaged) current density.

Hence

$$2\bar{j}\cdot\bar{j}'/\sigma = 2j\sin\theta\ j_x'/\sigma$$

$$= (2j^2\sigma'/\sigma^2)\sin\theta(\sin\theta+\beta_e\cos\theta-\beta_e'\sigma\cos\theta/\sigma'). \qquad (B.26)$$

Considering the relationship between σ, n_e and β_e

$$\sigma = n_e\beta_e(e/B), \qquad (B.27)$$

we obtain

$$1-(\sigma/\sigma')(\beta_e'/\beta_e) = (\sigma/\sigma')(n_e'/n_e) = n_T/\sigma_T. \qquad (B.28)$$

Consequently, the final expression is written as

$$2\bar{j}\cdot\bar{j}'T_e/(\sigma T_e') = (2j^2/\sigma)\sigma_T\sin\theta(\sin\theta+\beta_e n_T\cos\theta/\sigma_T). \qquad (B.29)$$

Substitution of Eq.(B.29) into Eq.(B.17) then yields

$$\omega_i n_e\{3kT_e/2+(3kT_e/2+eV_i)n_T\} = (j^2/\sigma)\sigma_T\{2\sin\theta(\sin\theta+\gamma_e\cos\theta)-1\}$$

$$-A_T A, \qquad (B.30)$$

where γ_e is defined as

$$\gamma_e = \beta_e n_T/\sigma_T. \qquad (B.31)$$

In the unperturbed state the enrgy equation denoted by Eq.(B.2) neglecting Q_r gives the relationship as follows

$$A = j^2/\sigma. \qquad (B.32)$$

Eq.(B.30) is thus reduced to

$$\omega_i(\text{growth rate}) = \{\sigma_T[2\sin\theta(\sin\theta+\gamma_e\cos\theta)-1]-A_T\}/\tau^*$$

$$= -(\sigma_T/\tau^*)\{\sqrt{1+\gamma_e^2}\cos(2\theta+\theta^*)+A_T/\sigma_T\}, \qquad (B.33)$$

$$\tau^* = n_e\{3kT_e/2+(3kT_e+eV_i)n_T\}/(j^2/\sigma), \qquad (B.34)$$

$$\theta^* = \arctan\gamma_e. \qquad (B.35)$$

The condition of the angle θ giving the maximum growth rate ω_i is obtained as

$$\cos(2\theta+\theta^*) = -1, \tag{B.36}$$

and the maximum ω_i is expressed as

$$(\omega_i)_{max} = (\sigma_T/\tau^*)(\sqrt{1+\gamma_e^2} - A_T/\sigma_T). \tag{B.37}$$

Defining the critical Hall parameter β_{cr} identical with the Hall parameter β_e which satisfies $(\omega_i)_{max}=0$, β_{cr} is written as

$$\beta_{cr} = \sqrt{A_T^2-\sigma_T^2}\ /n_T, \qquad (A_T \geq \sigma_T). \tag{B.38}$$

Expression of $(\omega_i)_{max}$ in term of β_{cr} is then obtained as

$$(\omega_i)_{max} = \{\sqrt{(\beta_e n_T)^2+\sigma_T^2} - \sqrt{(\beta_{cr} n_T)^2+\sigma_T^2}\}\ /\tau^*. \tag{B.39}$$

The most probable direction in which the ionization instability will propagate may be written as

$$\cos(2\theta+\theta^*) = -1, \tag{B.40}$$

and hence

$$\theta = \arctan\{(1+\sqrt{1+\gamma_e^2})/\gamma_e\}. \tag{B.41}$$

It is easily understood that the following relationship will hold

$$\beta_e < \beta_{cr}; \qquad \omega_i < 0, \quad \text{stable}, \tag{B.42}$$

$$\beta_e > \beta_{cr}; \qquad \omega_i > 0, \quad \text{unstable}. \tag{B.43}$$

Hence the Hall parameter must satisfy the relation in Eq.(B.42) in order that the plasma is stable to ionization instability.

The most feasible way to stabilize the MHD plasma is to increase the critical Hall parameter β_{cr}, the reason for which will be obviously seen from Eq.(B.42). From Eqs.(B.12) and (B.38), β_{cr} is readily written as

$$\beta_{cr} = \sqrt{A_T^2-\sigma_T^2}\cdot\frac{2-\alpha_i}{1-\alpha_i}\ /(3/2+eV_i/kT_e). \tag{B.44}$$

The above equation shows that β_{cr} may increase to a considerable

degree, as the ionization degree approaches unity. One of the ways to make α_i as large as unity (complete ionization) is to increase T_e as much as possible which will be immediately thought of, but this is practically impossible for a MHD generation due to severe limitation of the electron temperature. Therefore, other methods must be investigated.

Using Eqs.(B.5) and (B.13), the ionization degree α_i is expressed as

$$\alpha_i = 2/\{1+\sqrt{1+4n_{s0}/S(T_e)}\} , \tag{B.45}$$

which shows that with decreasing the value of $n_{s0}/S(T_e)$, α_i approaches unity. This situation will be easily realized by a very small seed fraction as was indicated by Belousov et al.[54], and experimentally proved by Nakamura et al.[32].

In the calculation of collision frequencies, the following expressions are adopted.

$$\nu_{ej} = \nu_{ej}(elastic\ collision) + \nu_{ej}(Coulomb\ collision) \tag{B.46}$$

1) electron-potassium atom;

$$\nu_{e1}(elastic\ collision) = n_K\sqrt{8kT_e/(\pi m_e)}\cdot Q_{e1}, \tag{B.47}$$

$$Q_{e1} = 4.0\times10^{-18}\ m^2, \tag{B.48}$$

2) electron-argon atom;

$$\nu_{e2}(elastic\ collision) = n_A\sqrt{8kT_e/(\pi m_e)}\cdot Q_{e2}, \tag{B.49}$$

$$Q_{e2} = \{6.0+0.0055|T_e-2000|\}\times10^{-21}\ m^2\ [17], \tag{B.50}$$

3) electron-potassium ion;

$$\nu_{e1}(Coulomb\ collision) = n_K^+\ T_e^{-3/2}\ c_o ln\ \Lambda, \tag{B.51}$$

$$c_o = e^4/(6\sqrt{2m_e}\pi^3k^3\varepsilon_o^2), \tag{B.52}$$

$$\Lambda = (12\pi/e^3)(\varepsilon_o kT_e)^{3/2}/n_e^{1/2}, \tag{B.53}$$

4) electron-argon ion;

$$\nu_{e2}(Coulomb\ collision) = n_A^+\ T_e^{-3/2}\ c_o ln\ \Lambda. \tag{B.54}$$

With respect to the collision loss parameters of electrons, they are taken to be 2 both for argon and potassium atoms.

REFERENCES

[1] R.J. Rosa, Phys. Fluids, 5(1962)1081

[2] H. Hurwitz Jr., R.W. Kirb and G.W. Sutton, J. Appl. Phys., 32(1961)205

[3] R.J. Rosa, Magnetohydrodynamic Energy Conversion, p.66(1968, McGRAW-HILL, New York)

[4] Z.D. Celinski and F.W. Fisher, AIAA J., 4(1966)421

[5] I. Michiyoshi and M. Numano, J. Nucl. Sci. Technol., 6(1969) 443

[6] R. Decher, M.A. Hoffman and J.L. Kerrebrock, AIAA J., 9(1971) 357

[7] D.A. Oliver and M. Mitchner, AIAA J., 5(1967)1424

[8] L.L. Lengyel, Energy Conversion, 9(1969)13

[9] J. Burger and G. Brederlow, Proc. of 11th Symp. on Eng. Aspects of MHD, p.205(1970, Calif. Inst. of Tech., Pasadena)

[10] G.F. Hohnstreiter, C.H. Kruger, R.M. Evans and M. Mitchner, Electricity from MHD, Vol.2, p.3(1968, IAEA, Vienna)

[11] R.J. Rosa and S. Petty, Proc. of 13th Symp. on Eng. Aspects MHD, II.7(1973, Stanford Univ., Stanford)

[12] A.V. Gubarev, L.M. Degtyarev, A.A. Samarskii and A.P. Favorskii, 5th Int. Conf. on MHD Elect. Power Gen., Vol.2, p.159(1971, IAEA, Vienna)

[13] P. Fritzer, L.L. Lengyel and K.J. Witte, Proc. of 12th Symp. on Eng. Aspects of MHD, III.7(1972, ANL, Illinois)

[14] J.W.M.A. Houben, J.H. Blom and L.H.T. Rietjens, AIAA J., 10 (1972)1513

[15] E.P. Velikov and A.M. Dykhne, Proc. of 6th Int. Conf. on Ionization Phenomena in Gases, Vol.4, p.511(1964, BECENS, Paris)

[16] J.L. Kerrebrock, AIAA J., 2(1964)1072

[17] A.H. Nelson and M.G. Haines, Plasma Phys., 11(1969)811

[18] S. Yoshikawa and D.J. Rose, Phys. Fluids, 5(1962)334

[19] A. Solbes, Electricity from MHD, Vol.1, p.499(1968, IAEA, Vienna)

[20] E.P. Velikov, L.M. Degtyarev and A.P. Favorskii, 5th Int. Conf. on MHD Elect. Power Gen., Vol.2, p.307(1971, ZAED, Karlsruhe)

[21] G. Brederlow and R.T. Hodgson, AIAA J., 6(1968)1277

[22] R.M. Evans, SU-IPR report No.429(1971, Stanford Univ., Stanford)

[23] J.L. Kerrebrock and R. Dethlefsen, AIAA J., 6(1968)2115

[24] L.L. Lengyel, Proc. of 11th Symp. on Eng. Aspects of MHD, p.193(1970, Calif. Inst. of Tech., Pasadena)

[25] W. Riedmüller, ibid., p.199

[26] T. Hiramoto, Phys. Fluids, 13(1970)1492

[27] A.H. Nelson, AIAA J., 8(1970)1753

[28] A.V. Nedospasov, Electricity from MHD, Vol.2, p.345(1966, IAEA, Vienna)

[29] E.E. Zukoski and R.R. Gilpin, Phys. Fluids, 10(1967)1974

[30] J. Bernard, P. Ricateau and P. Zettwoog, Electricity from MHD, Vol.2, p.277(1966, IAEA, Vienna)

[31] A. Solbes, T. Nakamura and J.L. Kerrebrock, Proc. of 11th Symp. on Eng. Aspects of MHD, p.193(1970, Calif. Inst. of Tech., Pasadena)

[32] T. Nakamura and W. Riedmüller, 5th Int. Conf. on MHD Elect. Power Gen., Vol.2, p.291(1971, ZAED, Karlsruhe)

[33] A.R. Bishop and L.D. Nichols, AIAA J., 8(1970)829

[34] R. Dethlefsen and J.L. Kerrebrock, Proc. of 7th Symp. on Eng. Aspects of MHD, p.117(1966, Princeton Univ., Princeton)

[35] G. Brederlow, W. Feneberg and R. Hodgson, Electricity from MHD, Vol.2, p.29(1966, IAEA, Vienna)

[36] J.L. Kerrebrock, AIAA J., 4(1965)591

[37] Z. Croitoru, Electricity from MHD, Vol.2, p.245(1966, IAEA,

Vienna)

[38] K. Yoshikawa and Y. Hattori, Tech. Rep. Inst. Atom. Energy, Kyoto Univ., No.161(1973)

[39] K. Yoshikawa and I. Michiyoshi, J. Nucl. Sci. Technol., 7 (1970)394

[40] G. Brederlow and K.J. Witte, Proc. of 13th Symp. on Eng. Aspects of MHD, I.7(1973, Stanford Univ., Stanford)

[41] G. Brederlow, K.J. Witte and H. Zinko, AIAA J., 11(1973)1065

[42] J. Louis, Phys. Fluids, 10(1967)2062

[43] W. Riedmüller, IPP Rep. IV/52(1973, Max-Planck-Institut für Plasmaphysik, Garching, Germany)

[44] K. Yoshikawa and I. Michiyoshi, J. Quant. Spectrosc. Radiat. Transfer, 12(1972)1673

[45] Ch. Féry, Compt. rend., 137(1903)909

[46] H. Kohn, Ann. Physik, 44(1914)749

[47] E. Griffith and J.H. Awbery, Proc. Roy. Soc., 123(1929)401

[48] H.M. Strong and F.P. Bundy, J. Appl. Phys., 25(1954)1521

[49] W. Riedmüller, G. Brederlow and M. Salvat, Z. Naturforsch, 23a(1968)731

[50] A.C.G. Mitchell and M.W. Zemansky, Resonance Radiation and Excited Atoms, p.100(1961, Cambridge University Press, New York)

[51] H.R. Griem, Plasma Spectroscopy, p.91, p.418(1964, McGraw-Hill, New York)

[52] T. Hiramoto, J. Phys. Soc. Japan, 26(1969)785

[53] S.S. Penner, Quantitative Molecular Spectroscopy and Gas Emissivities, p.33(1959, Pergamon Press, London)

[54] V.N. Velousov, V.V. Eliseev and I.Ya. Shipuk, Electricity from MHD, Vol.2, p.323(1966, IAEA, Vienna)